Preparation and structure control of dielectric thin films by chemical solution deposition

Tadasu Hosokura
2012

Contents

Chapter 1 General Introduction

1.1 Introduction……..……1

1.2 Back ground of the study…….…….……2

1.2.1 Crystal structure and dielectric properties of $BaTiO_3$…….……2

1.2.2 Crystal structure and dielectric properties of $Ba_xSr_{1-x}TiO_3$ (BST) …….……3

1.2.3 CSD processes……...……..3

1.2.4 Deposition process……..……6

1.2.5 Microstructured materials……..…….……...10

1.2.6 Dielectric thin films……...10

1.2.7 Artificial superlattices of oxide materials…….……11

1.3 Objectives……..……..13

1.4 References…….……..14

Chapter 2 Preparation of microstructured barium titanate

2.1 Introduction…….20

2.2 Preparation of barium titanate with patterned microstructure by a novel electrophoretic deposition method…….……..…….……21

2.3 Conclusion…….…….…….39

2.4 References…….…….…….40

Chapter 3 Fabrication and characterization of $(Ba,Sr)TiO_3$ thin films by CSD method

3.1 Introduction…….42

3.2 Fabrication and electrical characterization of one-axes oriented epitaxially grown $(Ba,Sr)TiO_3$ thin films prepared by sol-gel method….…….…….43

3.3 Crystallization and decomposition kinetics of $Ba_{0.7}Sr_{0.3}TiO_3$ CSD films….……54

3.4 Effect of the heating rate to the properties of BST thin film by CSD……65

3.5 Conclusion…….…….…….76

3.6 References…….……..78

Chapter 4 (100) three-axis-oriented thin film prepared by CSD

4.1 Introduction……..……...….79

4.2 (100) three-axis-oriented $(Ba_{0.7}Sr_{0.3})TiO_3$ thin film prepared by CSD.....….…80

4.3 (100) three-axis-oriented $BaTiO_3$ thin film with $BaZrO_3$ buffer layer…….92

4.4 Conclusion……..……103

4.5 References…….…..104

Chapter 5 Artificial superlattices fabricated by chemical solution deposition

5.1 Introduction…….……..…..105

5.2 The (100)-oriented $SrTiO_3/BaTiO_3$ artificial superlattices fabricated by chemical solution deposition……..……...……108

5.3 Conclusion…….……..…….……..121

5.4 References……..……122

Summary……..……..……..…….……124

List of Publications……..……..….……..……127

Acknowledgment……...……..……..……132

Chapter 1

General Introduction

1.1 Introduction

Chemical solution deposition (CSD) method utilized for the synthesis of various perovskite-type thin films can be applied to large wafers (typically from 4 to 8 inches) and possesses definite advantages for the formation of such films with typical thicknesses from 100nm to 400nm. These advantages include good compositional homogeneity, stoichiometry control, high purity, and intermediate processing temperatures. CSD processing requires inexpensive and standard laboratory equipment for the formation of such thin films.[1]

Usually the chemical solution deposition methods used are spin-coating, dip-coating, or electrophoretic depositioning of the precursor solution.

Barium titanate (BT) and/or barium strontium titanate (BST) crystals, ceramics, and thin films are in increasing demand because of their applications in ferroelectric materials, ferroelectric memories[2], multilayer capacitors[3], optical devices[4], and so on. Recently, high-quality ferroelectric thin films have been used in advanced microwave signal-processing devices. Small, compact, and low-power microwave devices that can be fabricated from structures based on ferroelectric films include phase shifters, tunable filters, tunable resonators, phased array antennas, and frequency agile microwave radio transceivers. BT thin films satisfy most device requirements due to their unique properties. Epitaxial ferroelectric films are required for electro-optical applications such as optical waveguides because of their low propagation loss. BT thin films have been prepared by various techniques such as RF sputtering[5], pulsed laser deposition[6], metal-organic chemical vapor deposition (MOCVD)[7, 8], and CSD processing.

1.2 Back ground of the study

1.2.1 Crystal structure and dielectric properties of $BaTiO_3$

$BaTiO_3$ was discovered in 1942 by Wainer et al.[9] At almost the same time Wul et al.[10] and Ogawa[11] et al. discovered a barium titanate independently. $BaTiO_3$ was a very important discovery since it was the first ferroelectric structure without hydrogen bonds and had more than one ferroelectric phase. $BaTiO_3$ has tetragonally distorted perovskite structure, which belongs to ABO_3 family of perovskite mineral $CaTiO_3$. In this perovskite crystal structure, A and B are metal ions, the total charge of which is +6. To exhibit ferroelectric behavior the smaller ion must be of larger charge in order. In $BaTiO_3$, the radius of Ba^{2+} is 1.35 Å, and the radius of Ti^{4+} is 0.68 Å. The crystal structure of ABO_3 type perovskite structure is shown in figure 1.1. As seen from figure 1.1., the structure can be described also as a set of BO_6 octahedra arranged in a simple cubic pattern, with A atoms located in spaces between the octahedra. Above the Curie temperature, BT has the cubic perovskite structure and is paraelectric. Below the Curie temperature, a structural distortion takes place, leading to the lower symmetry and off-center shift of the Ti^{4+} cation. As a result, spontaneous polarization appears in BT.[12]

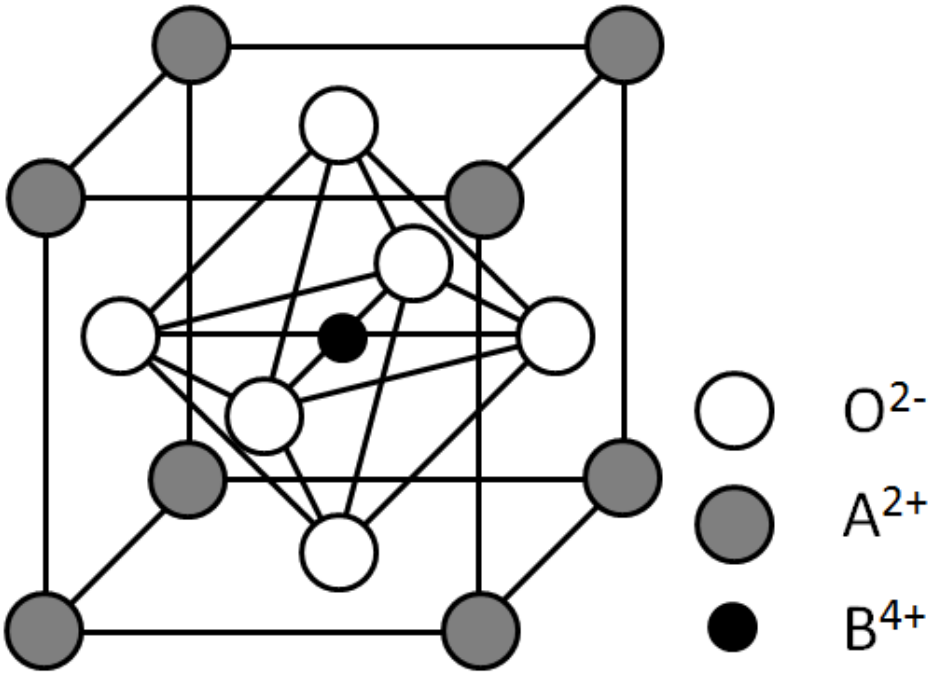

Figure 1.1 ABO_3 cubic perovskite structure.[12]

1.2.2 Crystal structure and dielectric properties of $Ba_xSr_{1-x}TiO_3$ (BST)

BST ($Ba_xSr_{1-x}TiO_3$) is a solid solution of $BaTiO_3$ and $SrTiO_3$. Ba-rich $Ba_xSr_{1-x}TiO_3$ compounds have tetragonal lattice and are ferroelectric, while Sr-rich $Ba_xSr_{1-x}TiO_3$ compounds are cubic and paraelectric at room temperature.[13] Substituting Ba with Sr results in the decrease of the Curie temperature and the increase of the dielectric constant of the material.[14] The phase diagram of the $BaTiO_3$-$SrTiO_3$ system has been studied by several groups.[15-20] The phase diagram in the entire concentration range obtained by Menoret et al.[15]

Exceptionally high values of the dielectric constants have been reported for bulk BST ceramics (2500)[21] and epitaxial films (2000–6000).[22] The high dielectric constant of ferroelectric BST arises from an ionic displacement upon applied electric field. BST has the ability to change the dielectric constant and dielectric-loss tangent near the ferroelectric Curie temperature by an externally applied field, which makes this material ideally suited for electrically tunable microwave devices, such as resonators, filters, and phase shifters.[23-28]

1.2.3 CSD processes

The CSD technique has been extensively used to synthesize a wide range of ferroelectric oxides[29-38] because of its numerous advantages, including simplicity, low cost, excellent thickness and compositional control, short fabrication cycle, and uniformity over large areas. A conventional sol-gel process includes the preparation of stable solution of metal oxide precursors in a suitable solvent with other chemical additives to control the solution properties. This is an important step for sol-gel processing, and many complicated chemical reactions such as hydrolysis, condensation, and chelation proceed during the solution preparation. The solution is partially hydrolyzed to form a stable sol, and then the sol is polymerized to form a gel. Afterwards, it is dried and fired to remove the organic components and form an oxide powder, which can be sintered to make ceramics. To fabricate thin films, the sol-gel solution is spin-coated on a flat substrate, and then the resulting film undergoes a low-temperature heat treatment (pyrolysis) to remove organic components. Most organic materials from precursor solutions are decomposed and removed from the films during the pyrolysis step. The thickness of the deposited layer is usually very low, of the order 50 nm, and preparation of films with thicknesses of 0.5-1μm

requires repeated deposition steps. Finally, the as-pyrolized amorphous film is subjected to high-temperature annealing to form a dense crystalline layer of the desired phase composition and thickness. More information about precursor characteristics as well as various chemical, physical, and technological aspects of the sol-gel process can be found in Refs. 39-44. Structural and, therefore, physical properties of sol-gel films depend strongly on such processing conditions as temperature of pyrolysis and final heat-treatment, heat treatment atmosphere and duration, solution composition, and seeding layer.[45-53]

It should be mentioned that although the sol-gel technique is studied and successfully used for many years, it still has some significant drawbacks. One of them is the formation of cracks during the drying process of a sol-gel film. As the solvent evaporates from the film, its volume decreases and the film shrinks, which results in biaxial tensile stress relieved by developing cracks.[54, 55] Delamination of the film due to the difference in thermal expansion coefficient between a film and a bottom electrode is one more unresolved problem.[55] Among other limitations of this technique are poor step coverage and residual organic impurities in the films.[56]

In the case of perovskite-type ferroelectrics, such as PZT, one of the major drawbacks of the sol-gel technique is that it does not yield the desired perovskite phase directly. The formation of perovskite phase upon final annealing is preceded by the undesirable nonferroelectric pyrochlore phase. It was found that distribution of the nearest neighbor and next nearest neighbor ions in the pyrochlore phase is similar to those in the amorphous phase.[45] Therefore, although perovskite is the thermodynamically stable phase in the temperature range used in sol-gel fabrication, the transformation from amorphous to pyrochlore phase is kinetically more favorable than a straight transformation to the perovskite phase.

The perovskite thin films preparation by CSD may be grouped into two categories:

(1) Sol-gel processes

(2) Metal organic decomposition (MOD)

Figure 1.2 shows the flow chart of a typical CSD process of preparing metal oxide thin films.

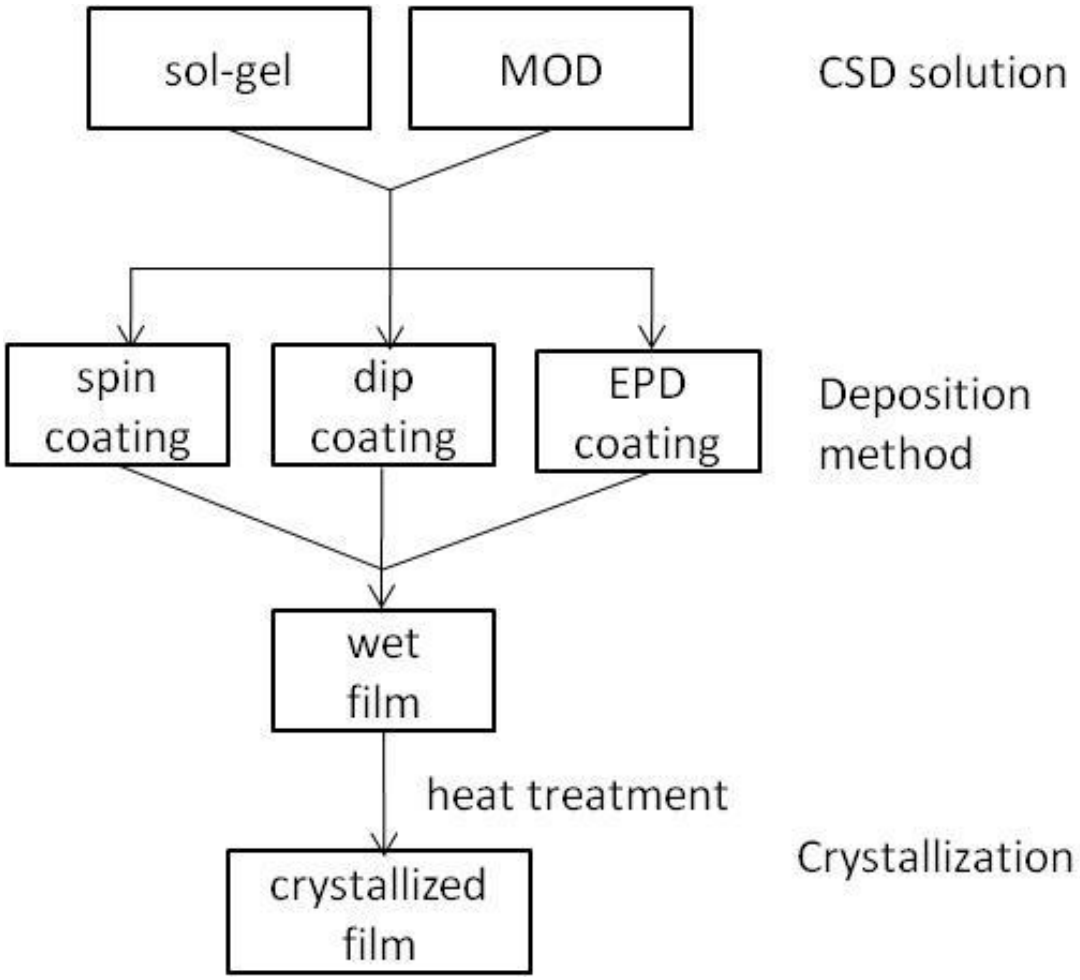

Figure 1.2 Flow chart of a typical CSD process.

(1) For sol-gel processes, 2-methoxyethanol (CH_3-OCH_2CH_2OH) is most extensively used in the chemical synthesis of perovskite materials. Alkoxides are usually considered to be the most appropriate starting materials for sol-gel processes since the metal-oxygen-metal (M-O-M) bonds are key reactions of hydrolysis.

• Hydrolysis

$$M(OR)_x + H_2O \rightarrow M(OR)_{x-1}(OH) + ROH \quad (1)$$

• Condensation (alcohol elimination)

$$2\ M(OR)_{x-1}\ (OH) \rightarrow M_2O(OR)_{2x-3}(OH) + ROH \quad (2)$$

• Condensation (water elimination)

$$2\ M(OR)_{x-1}\ (OH) \rightarrow M_2O(OR)_{2x-2}(OH) + H_2O \quad (3)$$

Pre-hydrolysis of less reactive alkoxides may be used to improve solution compositional uniformity. Often an alcohol exchange reaction results in decrease of hydrolysis sensitivity. During an alcohol exchange process a less reactive alkoxy group (2-methoxyethoxy group in this case represented by (OR') replaces a more reactive alkoxy group (OR).

$$M(OR)_x + xR'OH \rightarrow M(OR')_x + xROH \quad (4)$$

2-methoxyethanol has often been used for the dissolution of carboxylate precursors like barium acetate ($Ba(OCOCH_3)_2$).

Ba-Ti alkoxied is reactive and easily decompose to Ba-Ti based hydro-oxide gels. Dissolving concentration of Ba-Ti alkoxied to 2-methoxyethanol is around 0.1 mol/l.

(2) MOD routes utilize carboxylate precursors. Basically, dissolving the metalloorganic compounds in a common solvent (e.g. carboxylate or β-diketonates) and combining the solutions to yield the desired stoichiometry and concentration. The use of chelating agents like acetylacetone (β–diketonate) can lead to the formation of monomeric compounds and lower the organic content of the film. This reduces film shrinkage during drying and decreases cracking. Although the solutions are water insensitive, the presence of carboxylate ligands with alcohols leads to esterification. Solutions, therefore, still exhibit aging and display changes and films produced from such aged solutions differ in property. To decompose the precursors and obtain perovskite materials, annealing is proceeded under oxygen atmosphere.

1.2.4 Deposition process

Deposition process of CSD may be grouped into three categories:

1) Spin coating

2) Dip coating

3) Electrophoretic deposition (EPD)

1) After precursor solution has been prepared, films are formed by coating process. Spin coating is achieved on the planar substrates by a spinner. The substrate is kept in place on the spinner by applying a vacuum from the backside. The precursor solution is poured with using a syringe with a filter on the substrate. The substrate is then accelerated rapidly to 1000 to 8000 rpm. The angular velocity, the spinning time, and the solution viscosity, can be used to control the thickness of the wet film. The schematic illustration of spin coating process is shown in figure 1.3. This characteristic determines the thickness of the final ceramic film. To convert the as-deposited film into the crystalline dense perovskite phase, the film is usually heated rapidly to the crystallization temperature, which results in both organic removal and crystallization. This is because the nucleation is predominantly homogeneous and lead to small polycrystalline grains. By heating rapid (>100 °C/s) rates, condensation reactions between the precursor species are delayed and the film is freer to densify without cracking. For films that are not pyrolyzed but are heated directly to the crystallization temperature, both precursor chemistry and heating rate can affect the densification of the film.

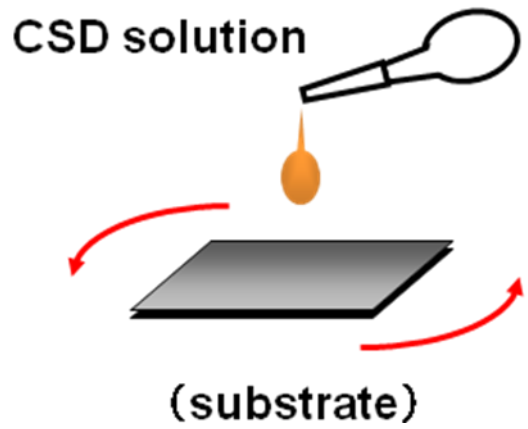

Figure 1.3 Schematic illustration of spin coating process

2) Dip coating (figure 1.4) is another deposition method widely used these days. The general steps are immersion of the substrate into the dip-coating solution, start-up withdrawal of the substrate from the solution, film deposition, solvent evaporation, and continued drainage as the substrate is completely removed from the liquid bath.[57] The thickness of the film that is formed in dip-coating is governed by viscosity, gravitational forces, and the surface tension in the concavely curved meniscus among others. For dip-coating from sol-gel solutions, the characteristics of the precursor (sticking probability), aggregation and gelation behaviors also play a key role in defining both the thickness and nature of the film.

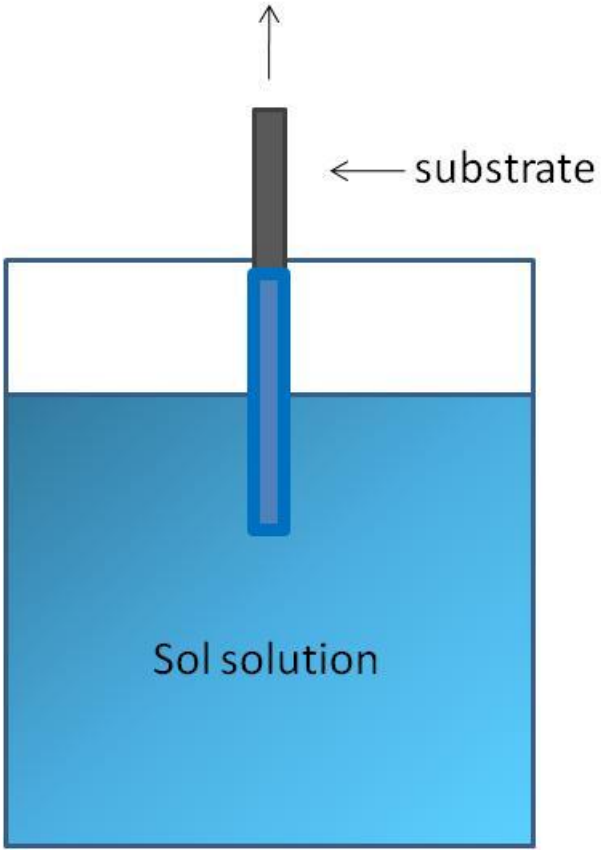

Figure 1.4 Schematic illustration of dip coating process

3) An EPD is known to be one of the most effective and efficient techniques to fabricate functional materials and devices.[58-61] In fact, this method has been utilized to prepare thin film of various ceramics, for biomaterials, sensing materials, energy conversion materials, optical materials, and so on.[62-67] A general schematic illustration of EPD process is shown in figure 1.5.

In the EPD process, a voltage difference is applied across two electrodes immersed in a suspension, and then a layer of particles is formed on one of the electrodes. Thus, an electric field is used as an external force for a fabrication of layer consisting of various particles (such as ceramic, metal, polymer, and their composite). This technique has received much attention due to its simplicity in experimental setup, low equipment cost, high deposition rate, easiness of thickness control, and capability to complex shapes and patterns. In addition, porous ceramics and high ionic conductive polymer as well as electron conductive material such as metal can be employed as the substrate in the EPD system.

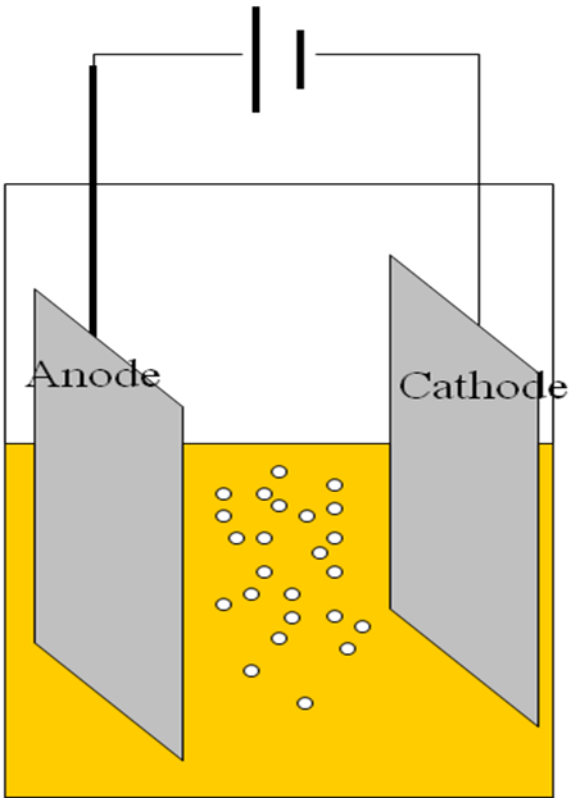

Figure 1.5 Schematic illustration of EPD process.

1.2.5 Microstructured materials

Periodic patterning of mesostructured materials is attracting much attention for microelectromechanical systems (MEMS)[68], sensors[69], magnetic applications and optical applications.[70–72] Many studies have contributed to the control of the pore size, mesostructure (i.e., lamellar, hexagonal, or cubic), and morphology (i.e., powder or film) of the mesoporous materials obtained.[73–75] Ferromagnetic cobalt based metals were electroless-deposited into microstructured porous silicon (PS) pores. Perpendicular magnetic anisotropy changed in the electroless cobalt-boron layer prepared to be microstructured material.[76]

Porous patterns can be fabricated by placing a solution droplet into a polymer stamp, a reversed replica of a patterned master that has already been prepared using lithography. Stucky and co-workers have proposed patterning procedures, which combines solution chemistry with soft lithography.[77, 78] Another approach for direct patterning thin-film media has been reported.[79, 80] In the reports, a photosensitive thin film was prepared on substrates and then exposed to UV light with a photomask on top of each thin film. Subsequent chemical etching or heat treatments would result in porous patterns with a desired shape. This approach restricts the reacting materials to photosensitive media, which cannot be applied in most non-photosensitive surfactant-templated porous materials. An electron-beam (EB) lithography patterning method can be prepared without a photomask and directly draw a pattern on a photosensitive thin film. EB lithographic technique is very useful for patterning mesoporous thin films with a controllable morphology and various chemical compositions.

1.2.6 Dielectric thin films

The dielectric BST thin films have been under development for nearly two decades. Initially, they were used for the manufacturing of high density miniaturized or integrated thin film decoupling capacitors. During the last decade BST film properties increased because of their potential use in tunable microwave applications attested to the large variation of their strong voltage tunability. Much research has focused on strain effects and the influence of substrate on BST thin films properties, e.g.: how lattice structure distortions affect the direction and the magnitude of polarization formation and what is the response to an applied electric field.

Historically, the research activities in BST films deposition started in Japan more than two decades ago lead by the NEC.[81] BST thin films were directly deposited from a BST target by RF-sputtering and/or ion beam assisted deposition on r-cut sapphire substrates with Pt, Ru or RuO_2 electrodes, and the initially obtained dielectric constants were in the range of 820-880 for 475 nm thick $Ba_{0.5}Sr_{0.5}TiO_3$ film deposited.[82, 83] Many additional reports followed during the next decade by the method of MOD or CSD, which became the most common used method for BST films fabrication. Few comprehensive reviews on CSD technique have been published, providing further details on the mechanism of film crystallization, and tailoring of microstructure through manipulation of deposition parameters.[84-86]

1.2.7 Artificial superlattices of oxide materials

Artificial superlattices of oxide materials have attracted the attention of material scientists because the superlattices have the potential to drastically improve material properties.[87, 88] Oxides with the perovskite-type structure exhibit various properties, such as ferroelectricity, piezoelectricity, and superconductivity; therefore, the artificial superlattices of the perovskite structure, where materials with different properties are stratified at an atomic level, seem to be one of the most interesting systems in the research of the oxide superlattices. Some research groups have succeeded in fabricating artificial superlattices of the perovskite compounds.[89–96] Anomalies in the dielectric properties of $BaTiO_3/SrTiO_3$ (BT/ST) superlattice were pointed out by Tabata *et al.*[93] and Nam *et al.*[97] However, the dielectric properties of BT/ST superlattices are still not very reliable because of their high leakage currents. It is very important to understand the origin of the high leakage currents and to establish the method to measure dielectric properties of oxide superlattices.

Optical properties of BT/ST superlattices have not been measured except for the second harmonic generation by Zhao *et al.*[95] Ellipsometry is a powerful technique to determine the thickness and the refractive index of thin films. This technique has been applied to superlattices of semiconductors by many researchers.[98,99] The schematic illustration of artificial superlattices is shown in figure 1.6.

The tetragonal form of $BaTiO_3$ exhibits ferroelectric distortions involving displacements of the cations Ti^{4+}, Ba^{2+} relative to the anions O_2^-, leading to a net dipole moment per unit volume. These soft-mode distortions correspond to a 1% c axis/a axis lattice strain in

tetragonal BT. When one BT layers are combined with ST layers as BT/ST superlattices, there is a relatively large mismatch of 3.0% between the in-plane lattice parameters (BT; 3.990 Å, ST; 3.905 Å). Thus strain is induced by changing the periodicity of the strained superlattices. In order to study the importance of the soft-mode coupling with the lattice strain, ferroelectric strained superlattice is also effective, because even in cases with small strain in BT, the strain energy strongly affects the phase transition as was indicated in the bulk sample.

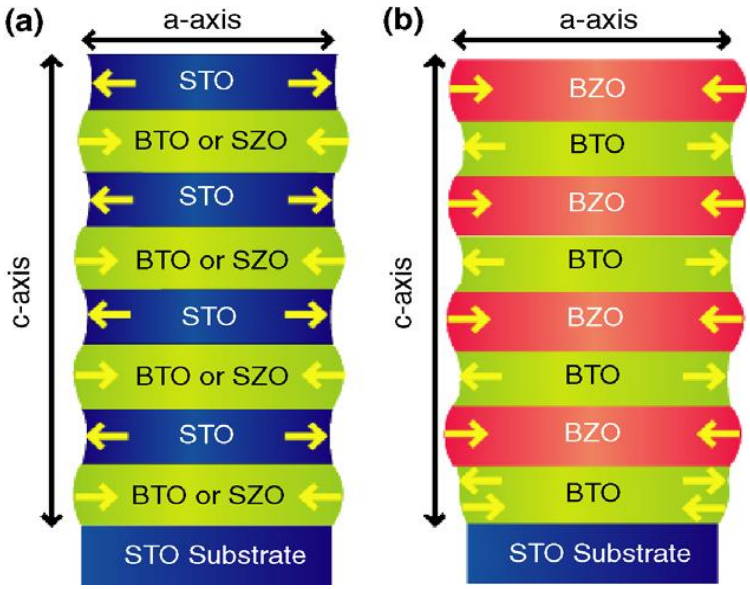

Figure 1.6 Schematic illustration of artificial superlattices. [99]

1.3 Objectives

Processing conditions have a significant effect on controlling thin film structures. The performances of the films are drastically determined by the structures of the film.

(a) To produce BT patterned microstructures by combining high-concentration metal alkoxides sol-gel processing, an electrophoretic deposition technique, and EB lithography. This deposition technique for formation of BT patterned microstructures is very promising for fabricating photonic crystals.

(b) To control the orientation and the morphology of the BT and BST thin film prepared by CSD method. The fabrication of the orientation and the morphology controlled thin films will be useful to produce thin film devices using BT and BST.

(c)To produce $SrTiO_3$(100)/$BaTiO_3$(100) artificial superlattices with the thickness of the layer less than 10 nm synthesized by the CSD method. This finding is expected to lead to artificial superlattices of oxide materials synthesized by CSD, which will drastically improve the material properties and open the door for the wide use of artificial superlattices of oxide materials.

1.4 References

[1] Schwartz R. W., Schneller. and T., Waser R., C. R. Chimie., **7** (2004) 433.

[2] Chen K.-H., Chen Y.-C., Chen Z.-S., Yang C.-F., Chang T.-C., Appl. Phys. A, **89** (2007) 533.

[3] Takeshima Y., Shiratsuyu K., Takagi H., and Sakabe Y., Jpn. J. Appl. Phys., **36** (1997) 5870.

[4] Tang P., Towner D. J., Meier A. L., and Wessels B. W., Appl. Phys. Lett., **85** (2004) 4615.

[5] Gevorgian S., Ferroelectrics in Microwave Devices, Circuits and Systems Physics, Modeling, Fabrication and Measurements; Springer-Verlag : London, (2009).

[6] Tabata H.; Tanaka H., and Kawai T, Appl. Phys. Lett., **65** (1994) 1970.

[7] Iijima K., Terashima T., Bando Y., Kamigai K., and Terauchi H., J. Appl. Phys., **72** (1992) 2840.

[8] Tsurumi T., Suzuki T., Yamane M., and Daimon M., Jpn. J. Appl. Phys. Part 1, **33** (1994) 5192.

[9] E. Wainer, N. Salomon, Titanium Alloy Mfg. Co. Elec. Rep, **120**, (1942) 184.

[10] Wul, I., and M. Goldman, Comptes Rendus URSS, **46** (1945) 139.

[11] Ogawa Takeo, Busseiron kenkyu, **6** (1947) 1 (in Japanese).

[12] N. Izyumskaya A. Alivov, and H. Morkoc, Critical Reviews in Solid State and Materials Sciences, **4** (2009) 89.

[13] B. A. Baumert, L.-H. Chang, A. T. Matsuda, T.-L. Tsai, C. J. Tracy, R. B. Gregory, P. L. Fejes, N. G. Cave, W. Chen, D. J. Taylor, T. Otsuki, E. Fujii, S. Hayashi, and K. Suu, J. Appl. Phys., **82** (1997) 2558.

[14] Sharmistha Lahiry, and A. Mansingh, Thin Solid Films, **516** (2008) 1656.

[15] C. Menoret, J. M. Kiat, B. Dkhil, M. Dunlop, H. Dammak, and O. Hernandez, Phys. Rev. B, **65** (2002) 224104.

[16] D. Barb, E. Barbulescu, and A. Barbulescu, Phys. Status Solidi A, **74** (1982) 79.

[17] V. V. Lemanov, E. P. Smirnova, P. P. Syrnikov, and E. A. Tarakanov, Phys. Rev. B, **54** (1996) 3151.

[18] M. E. Guzhva, V. V. Lemanov, P. A. Markovin, Fiz. Tverd. Tela and S. Peterberg Phys. Solid State, **39** (1997) 618,.

[19] V. S. Tiwari, N. Singh, and D. Pandey, J. Phys., Condens. Matter., **7** (1995) 1441.

[20] N. Singh and D. Pandey, J. Phys., Condens.Matter., **8** (1996) 4269.

[21] U. Syamaprasad, R. K. Galgali, and B. C. Mohanty, Mater. Lett., **7** (1988) 197.

[22] C. M. Carlson, T. V. Rivkin, P. A. Parilla, J. D. Perkins, D. S. Ginley,A. B. Kozyrev, V. N. Oshadchy, and A. S. Pavlov, Appl. Phys. Lett., **76** (2000) 1920.

[23] P. Bao, T. J. Jackson, X. Wang and M. J. Lancaster, J. Phys. D: Appl. Phys. **41** (2008) 063001.

[24] D. Galt, J. Price, J.A. Beall, and R.H. Ono, Appl. Phys. Lett., **63** (1992) 3078.

[25] V.N. Kesis, A.B. Kozyrew, M.L. Khazov, J. Sok, and J.S. Lee, Electron. Lett., **34** (1998) 107.

[26] Y. Liou, W.K. Chu, and C.W. Chu, Appl. Phys. Lett., **75** (1999) 412.

[27] J. Im, O. Auciello, S. Streiffer, P. Baumann, D. Kaufman, and A.R. Krauss, Appl. Phys. Lett., **76** (2000) 625.

[28] W.J. Kim, W. Chang, S.B. Qadri, J.M. Pond, S.W. Kirchoefer, D.B. Chrisey, and J.S. Howitz, Appl. Phys. Lett., **76** (2000) 1185.

[29] Lazarevic Z, Stojanovic BD, Varela JA, SCIENCE OF SINTERING., **37** (2005) 199.

[30] Manoj Kumar, Ashish Garg, Ravi Kumar, and M.C. Bhatnagar, Physica B, **403** (2008) 1819.

[31] Zhiqiang Wei,Huping Xu, Minoru Noda and Masanori Okuyama, Journal of Crystal Growth, **237** (2002) 443.

[32] Reaney, I.M., Taylor, D.V., and Brooks, K.G. , J. Sol-Gel Sci. Technol., **13** (1998) 813,.

[33] Tsai SD, Suresh MB, and Chou CC, Improvement in ferroelectric properties of PZT thick films prepared by a modified sol-gel, PHYSICA SCRIPTA, **T129** (2007) 175.

[34] Pu, Zhaohui, Wu, Jiagang, Yu, Xudong, Xu, Peng, Cheng, Lifang, Xiao, Dingquan, and Zhu, Hanguo, SURFACE & COATINGS TECHNOLOGY **202** (2008) 2068.

[35] L.N. Gao, S.N. Song, J.W. Zhai, X. Yaoa, and Z.K. X , Journal of Crystal Growth **310** (2008) 1245.

[36] Graca MPF, da Silva MGF, and Valente MA, Journal of the Europian Ceramic Society, **28** (2008) 1197.

[37] Qi, Yajun, Lu, Chaojing, Zhang, Qiaofeng, Wang, Lihua, Chen, Fang, Cheng, Chunsheng, and Liu, Baoting, J. of Physics D Applied Physics, **41** (2008) 065407.

[38] Ye, Wanneng, Lu, Chaojing, Qi, Yajun, Liu, Xiaolin, Senz, Stephan, Lee, Sung Kyun, and Hesse, Dietrich, Applied Physics A-Materials Science & Processing, **91** (2008) 323.

[39] Schneller T, and Waser R, Ferroerctrics. **267** (2002) 293.

[40] Waser, R., Schneller, and T., Horrmann-Eifert, S., and Ehrhart, P., Integrated Ferroelectrics, **36** (2001) 3.

[41] Schwartz, R.W., Boyle, T.J., Lockwood, S.J., Sinclair, M.B., Dimos, D., and Buchheit, C.D., Int. Ferroelectrics, **7** (1995) 259,.

[42] Schwartz, R.W., Schneller, T., and Waser, R., Comptes Rendus Chimie, **7**(2004) 433.

[43] Majumder SB, Bhaskar S, and Katiyar RS, A review, Integrated Ferooelectrics, **42**, 245 (2002) 36.

[44] Vorotilov KA, Yanovskaya MI, Turevskaya EP, and Sigov AS, Journal of Sol-Gel Science and Technology, **16**, 109 (1999) 36

[45] Reaney, I.M., Taylor, D.V., and Brooks, K.G., J. Sol-Gel Sci. Technol., **13** (1998) 813,.

[46] Brooks K. G., Reaney, I. M., Klissurska, R., Huang, Y., Buzsill, L., and Setter, N., J. Mater. Res., **9** (1994) 2540.

[47] Tiwari, V. S., Kumar, A., and Wadhawan, V. K., J. Mater. Res., **13** (1998) 2170.

[48] Bursil, L.A. and Brooks, Keith G., J. Appl. Phys., **75** (1994) 4501.

[49] Klee, M., Eusemann, R., Waser, R., Brand, W., and Van Hal, H., J. Appl. Phys., **72** (1992) 1566.

[50] Vorotilov, K.A., Yanovskaya, M.I., Turevskaya, E.P., and Sigov, A.S., J. Sol-Gel Sci. Technol., **16** (1999) 109.

[51] Lefevre, M. J., Speck, J. S., Schwartz, R. W., Dimos, D., and Lockwood, S. J., J. Mater. Res., **11** (1996) 2076.

[52] Law, C. W., Tong, K.Y., Li, J. H., and Li, K., Thin Solid Films, **335** (1998) 220.

[53] Gong, W., Li, J.-F., Chu, X., and Li, L., , J. European Ceramic Soc., **24** (2004) 2977.

[54] Meng, X. J., Cheng, J. G., Li, B., Guo, S. L., Ye, H. J., and Chu, J. H., J. Cryst. Growth, **208** (2000) 541.

[55] Shen, I.Y. Steve., Cao, G. Z., Wu, Chia-Che, and Lee, Cheng-Ghun, Ferroelectrics, **342** (2006) 15.

[56] Hwang, Jae-Seob., Kim, Woo Sik., Park, Hyung-Ho., Kim, Tae-Song, Sensors and Actuators A, **117** (2005) 137.

[57] C.J. Brinker, and G.W. Scherer, Sol–Gel Science, Academic Press, Boston, (1990).

[58] P. Sarkar, P.S. Nicholson, J. Am. Ceram. Soc., **79** (1996) 1987.

[59] R. Moreno, and B. Ferrari, Am. Ceram. Soc. Bull., **79** (2000) 44.

[60] K. Kanamura, J. Hamagami, and T. Umegaki, Trans. Mater. Res. Soc. Jpn., **27** (2002) 67.

[61] I. Zhitomirsky, Adv. Colloid Interface Sci., **97** (2002) 279.

[62] J. Hamagami, Y. Inda, K. Yamashita, and T. Umegaki, Solid State Ionics, **235** (1998) 113.

[63] K. Yamashita, M. Nagai, and T. Umegaki, J. Mater. Sci., **32** (1997) 6661.

[64] Yamashita, E. Yonehara, X. Ding, M. Nagai, T. Umegaki, M. Matsuda, and J. Biomed. Mater. Res., **43** (1998) 46.

[65] T. Ishihara, K. Shimose, T. Kudo, H. Nishiguchi, T. Akbay, and Y. Takita, J. Am. Ceram. Soc., **83** (2000) 1921.

[66] T. Ishihara, K. Sato, and Y. Takita, J. Am. Ceram. Soc., **79** (1996) 913.

[67] K. Kanamura, and J. Hamagami ,Solid State Ionics, **172** (2004) 303.

[68] Paik J A, Fan S K, Kim C J, Wu M C, and Dunn B, J. Mater. Res., **17** (2002) 2121.

[69] Doshi D A, Huesing N K, Lu M, Fan H, Lu Y, Simmons-Potter K, Potter B G, Hurd A J and Brinker C J, Science, **290** (2000) 107.

[70] Yang P., Science, **287** (2000) 465.

[71] Doshi D A, Huesing N K, Lu M, Fan H, Lu Y, Simmons-Potter K, Potter B G Jr, Hurd A J and Brinker C J, Science, **290** (2000) 107.

[72] Scott B J, Wirnsberger G, McGehee M C, Chmelka B F and Stucky G D, Adv. Mater., **13** (2001) 1231.

[73] Ogawa M and Masukawa N., Micropor. Mesopor. Mater., **38** (2000) 35.

[74] Yang P, Deng T, Zhao D, Feng P, Pine D, Chmelka B F, Whitesides G M, Stucky G D Science, **282** (1998) 2244.

[75] Yang P, Rizvi A H, Messer B, Chmelka B F, Whitesides G M and Stucky G D, Adv. Mater., **13** (2001) 427.

[76] Tadasu Hosokura, Koh-ichi Maruyama, Izumi Ohno and Osamu Nittono, Journal of the Surface Finishing Society of Japan, **49** (1998) 401.

[77] Ha K, Lee Y J, Chun Y S, Park Y S, Lee G S and Yoon K B, Adv. Mater., **13** (2001) 594.

[78] Sugimura H, Hozumi A, Kameyama T, Takai O, Adv. Mater. **13** (2001) 667.

[79] DattelbaumAM, AmwegM L, Ecke L E, Yee C K, Shreve A P, Parikh A N, Nano Lett., **3** (2003) 719.

[80] Kim H C, Wallraff G, Kreller C R, Angelos S, Lee V Y, VolksenW ,Miller R D, Nano Lett., **4** (2004) 1169.

[81] Y. Miyasaka, S. Matsubara, IEEE 7th Int. Symp. Appl. Ferroelectr., ISAF 1990, (1990) 121.

[82] K. Takemura, T. Sakuma, Y. Miyasaka, Appl. Phys. Lett., **64** (1994) 2967.

[83] R. W. Schwartz, Chem. Mater., **9** (1997) 2325.

[84] R.W. Schwartz, T. Schneller, R. Waser, C. R. Chimie, **7** (2004) 433.

[85] U. Hasenkox, S. Hoffmann, R. Waser, J. Sol-Gel Sci. Technol., **12** (1998) 67.

[86] J. S. Cross and I. P. Koutsaroff, Journal of the Technical Association of Refractories, Japan, **62** (2010) 162

[87] H. Koinuma and N. Kanda, Shinku, **36** (1993) 67 (in Japanese).

[88] H. Tabata and T. Kawai, Shinku, **36** (1993) 81 (in Japanese).

[89] K. Iijima, T. Terashima, Y. Bando, K. Kamigai, and H. Terauchi, J. Appl. Phys., **72** (1992) 2840.

[90] T. Tsurumi, T. Suzuki, M. Yamane, and M. Daimon, Jpn. J. Appl. Phys., Part 1, **33** (1994) 5192.

[91] T. Tsurumi, T. Miyasou, Y. Ishibashi, and N. Ohashi, Jpn. J. Appl. Phys., Part 1, **37** (1998) 5104.

[92] F. Le Marrec, R. Farhi, M. El Marssi, J. L. Dellis, and M. G. Karkut, Phys. Rev. B, **61** (2000) 6447.

[93] H. Tabata, H. Tanaka, and T. Kawai, Appl. Phys. Lett., **65**, 1970 (1994).

[94] M. Yoshimoto, H. Ohkubo, N. Kanda, and H. Koinuma, Jpn. J. Appl. Phys., Part 1 **31** (1992) 3664.

[95] T. Zhao, Z.-H. Chen, F. Chen, W.-S. Shi, H.-B. Lu, and G.-Z. Yang, Phys. Rev. B, **60** (1999) 1697.

[96] D. H. Kim, D.-W. Kim, B. S. Kang, T. W. Noh, D. R. Lee, K.-B. Lee, and S. J. Lee, Solid State Commun., **114** (2000) 473.

[97] S. M. Nam, S. Mitarai, Y. Ishibashi, T. Tsurumi, and O. Fukunaga, J. Korean Phys. Soc., **29** (1996) S632.

[98] R. H. Hartley, M. A. Folkard, D. Carr, P. J. Orders, D. Rees, and I. K. Varga, J. Cryst. Growth, **117** (1992) 166.

[99] T. Harigai; Nam, S.-M.; Kakemoto, H.; Wada, S.; Saito, K.; Tsurumi, T., Thin Solid Films, **13** (2006) 509.

Chapter 2

Preparation of microstructured barium titanate

2.1 Introduction

There have been many studies on the preparation of metal oxide thin or thick films by electrophoretic deposition (EPD), in which suspensions of ceramic particles, usually with a diameter >100 nm, were used.[1-6] Such conventional EPD methods have been successfully employed to fabricate various ceramic film devices, ranging from capacitors[7,8] to fuel cells.[9-11] However, the green (as-deposited) films needed firing at high temperatures (usually >550 °C) for sintering, mainly because of the large size of the particles. A combined method of sol-gel processing and EPD has also been investigated. It was expected that it would provide a promising route to the fabrication of ceramic film devices at much lower temperatures[12] than those required for conventional EPD methods. One may call this fabrication process a precise soft chemical processing, since this method yields gel films consisting of sol-gel-derived nanometer-sized particles, and consequently, allows low-temperature synthesis of ceramic devices. To date, there have been several examples in which this method is applied to the formation of silica thick films.[13-15]

Many studies have been done on synthesis of ceramic thin or thick films of complex oxide, such as $Pb(Zr,Ti)O_3$[16] and $BaTiO_3$[17], by using electrophoretic depositions of ceramic particle-dispersed solutions. However, none of these previous studies were successful in obtaining dense ceramic films with a uniform microstructure by sintering at lower temperatures, probably because the sols they used contained particles with a rather broad size distribution and large particles were contained. To synthesize dense ceramic films with uniform microstructure at low temperatures, it is first necessary to produce sols with nanometer-sized particles having a very sharp size distribution. These suspensions would then be used for electrophoretic deposition.

To this end, sols were prepared by partially hydrolyzing a highly concentrated solution containing 1.1 mol/l Ba and Ti alkoxides. It has been confirmed that transparent, dense $BaTiO_3$ crystalline gel monoliths can be obtained from such a highly concentrated alkoxide suspension (>1.0 mol/L).[18,19] This study demonstrates that the solution of

partially hydrolyzed alkoxide is suitable for electrophoretic deposition as seen from the fact that a pseudo-cubic perovskite powder is obtained and the size of primary particles is about 20 nm in diameter. [20]

The use of electron-beam lithography is a very effective way for obtaining ceramic thin films with a patterned microstructure. For example, an array of Ni pillars having 35 nm diameter, 120 nm height and 100 nm periodic distance is fabricated on silicon by appling the electron-beam lithography to the film prepared by electroplating technique. [21]

In this work electron-beam lithography were used to produce resist molds, which were subsequently used to fabricate $BaTiO_3$ gel materials with a patterned microstructure by an electrophoretic deposition method developed in this study. This new technique is also promising as a means of fabricating photonic crystals (PCs).

2.2 Preparation of barium titanate with patterned microstructure by a novel electrophoretic deposition method

An electron beam resist (ZEP-520-22 Zeon Co.) was spun onto a substrate of $Pt/Ti/SiO_2/Si$ at 600 rpm for 90 sec and then at 2000 rpm. for 2 sec. The sample was heat-treated at 180 °C for 3 min. The thickness of the resist was typically 250 nm. This process was repeated three times to obtain a 750-nm-thick resist film. Dot arrays with a diameter of 250 nm and spacing of 500 nm distributed in a triangular lattice were formed in the resist by using an electron beam lithography system (ELS-5700 ELIONICS). The resist was heat-treated at 110 °C for 3 min after development.

A precursor suspension was prepared by dissolving $Ba(OC_2H_5)_2$ and $Ti(O\text{-}i\text{-}C_3H_7)_4$ with a molar ratio of 1:1 in a mixed solvent of methanol and ethyleneglycol monoethylether (EGMME) with a volume ratio of 3:2. The concentration of precursor suspensions was fixed at 1.1 mol/L for barium and titanium. The alkoxide precursor solutions were hydrolyzed at 250 K with water having an H_2O/Ba ratio (r_w) of 7. For electrophoretic deposition, 3 vol% of 2-dimethylaminoethanol (DMAE) was added to the hydrolyzed precursor suspension. Flow chart for the preparation of the microstructure by EPD is shown in figure 2.1.

Electrophoretic deposition from the sol was carried out at -20 °C. A stainless steel wire was used as the anode, and the resist mold was formed on the cathode. Distance between the anode and the cathode was held for 1 cm in the sol. The wet-gel film

deposited on the substrate was aged at 30 °C for one day and further aged at 50 °C for another day in a nitrogen atmosphere. It was then further aged at 150 °C for one day in an atmosphere of air. After aging, the resist mold was chemically removed by ZDMAC (Zeon Co.). Schematic illustration of preparation for the microstructure by EPD process is shown in figure 2.2.

Surface and cross section images of the gel films were taken with a field emission-scanning electron microscope (FE-SEM, Hitachi S-5000). A focused ion beam system (FIB, SII SMI-9200) was used to cut the pillars of the array, and a scanning ion microscope (SIM, SII SMI-9200) was used to obtain the image of the cut pillars.

The titanium and barium contents of the gel were determined by inductively coupled plasma-atomic emission spectroscopy (ICP-AES, Thermo Jarrell Ash Corp. Iris Advantage). Characterization of crystalline phase was carried out by X-ray diffraction (XRD, MAC Science M18XHF).

Optical reflectance measurements was carried out by using the method reported by Poborchi et al.[22] to confirm that there were (Photonic band-gap) PBGs in the BT PCs. Schematic illustrations of optical reflectance measurements are shown in figure 2.13. A microscope, with a halogen lamp as a light source, and an objective lens (magnification: ×50) were used. As incident, light within the same frequency range as the PBGs cannot propagate in PCs, most of the light should be reflected. Thus, strong reflection was observed near the PBG frequencies. The samples were cleaved to have a facet surface perpendicular to the Γ-M and Γ-K direction in the Brillouin zone corresponding to the unit cell of the PCs with a hexagonal array. Incident light was irradiated on to the cleaved facets and the reflection was measured using a spectroscopy system. The range of the wavelength investigated was 400-1000 nm. To analyze the reflectance spectra obtained from the patterned BT film, an MIT Photonic Band Gap package was used. PCs were assumed to be perfectly two-dimensional, and that the refractive index for the BT was 2.5.

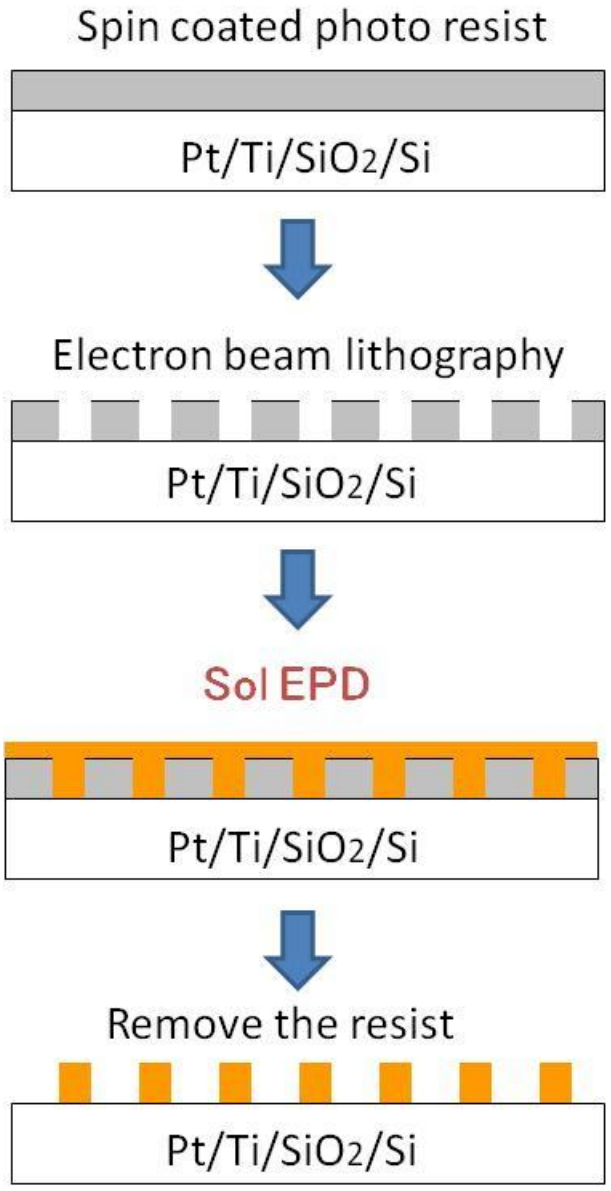

Figure 2.1 Flow chart for the preparation of the microstructure by EPD

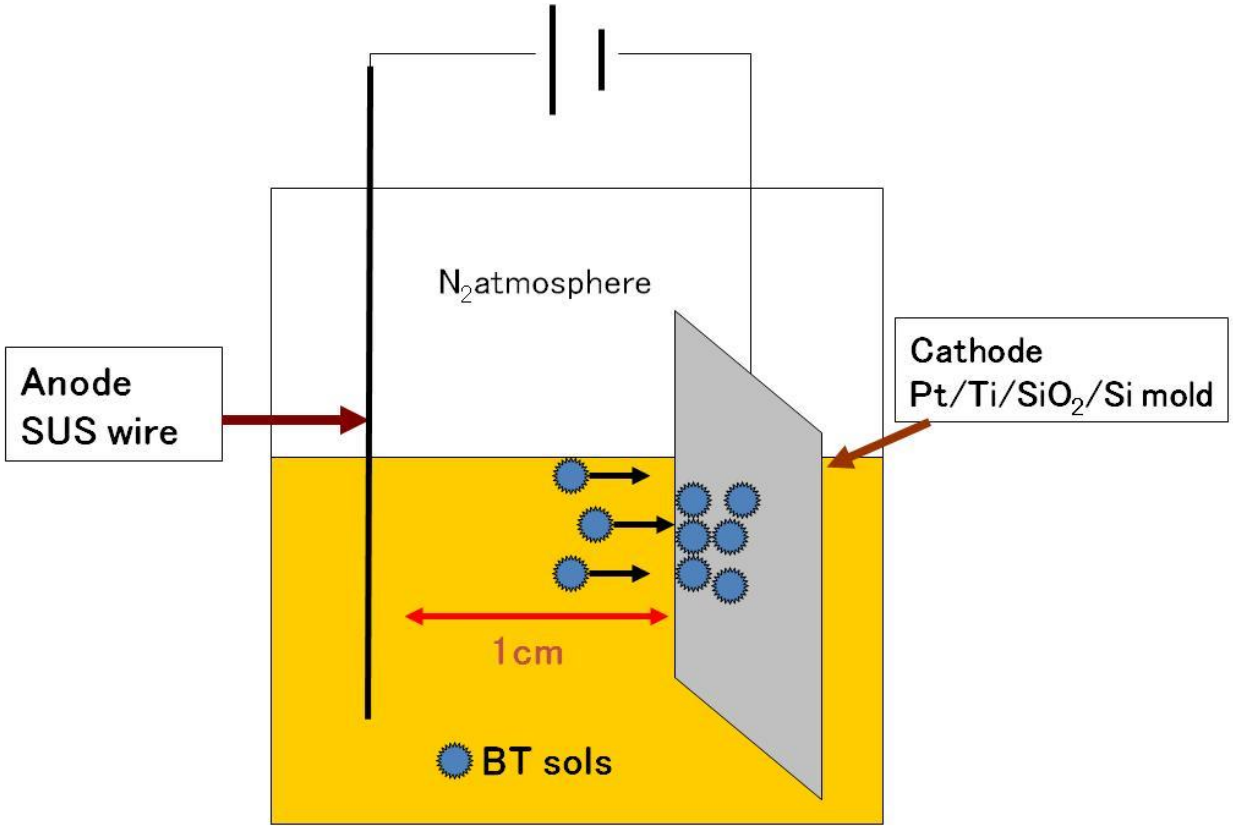

Figure 2.2 Schematic illustration of preparation for the microstructure by EPD process

Figure 2.3 shows the change in current with applied voltage during electrophoretic deposition of $BaTiO_3$ gel from the suspension without addition of DMAE. The voltage was raised by the step of 1 V with keeping time of 1 min. The current was measured 30 sec after the voltage was raised 1 V. A two-step increase in current is seen in the voltage ranges below and above 5 V. One may recognize that a significant increase in current occurs between 6 and 8 V. In this voltage range, generation of the gas bubbles was observed together with the deposition of the gel films on the cathode. Gas chromatography confirmed that bubbles contain hydrogen. Above 6 V, the current did not grow linearly. This is attributed to the limitation of the charge exchange between the hydrogen and the substrate surface. Generation of gas is undesirable for the fabrication of nanostructure pillars, because gas bubbles prevent the sol to deposit a densely film on the cathode. As the suspension is partially hydrolyzed, it contains hydrogen ions. Hydrogen ions play important roles during electrophoretic deposition because hydrogen gas is generated from hydrogen ions and the hydrogen ion concentration affects the polarity of the suspension.

It was reported that the surface charge of particles plays an important role in the formation of thin films by electrophoretic deposition of nanopowders.[23] In the work of reference [23], the surface charge of particles was controlled by adding ethanol to the base solvent (toluene) to change the polarity of the solvent. To prepare thick silica film on the cathode, a cationic polymer surfactant was used in the electrophoretic sol-gel deposition in order to control the surface charge of the silica particles.[13, 14]

DAME was added in order to decrease hydrogen ion concentration in the suspension. It was expected that this would change the polarity of the suspension and increase the positive charge of the sol. At the same time, the decrease of the hydrogen ion concentration resulted in decrease of hydrogen gas generation. Figure 2.4 shows the change in current with applied voltage for the suspension in which DMAE was added during electrophoretic deposition. The gel was deposited on the cathode without the generation of gas bubbles. This figure clearly demonstrates that the addition of DMAE changes the electrophoretic behavior of the sol to give a linear current-voltage characteristic. Besides this characteristic, it was observed that no gas was generated and a much thicker film could be deposited. The role of the DMAE in enhancing the electrophoretic deposition may be interpreted by an assumption that DMAE increases positive charge on the sol particles, making easier the precipitation of gels on the substrate. The mechanism of the electrophoretic deposition cannot explain concretely at

the moment. However it may be understandable that only the movement of the sol particles decides the electronic resistance of the sol, since no significant decline in current with time, that is, little polarization is observed. It may be concluded that the use of DMAE as a charge adjuster is effective for preparation of a sol suitable for electrophoretic deposition.

Fabrication of a ZnO nano-wire array embedded in an anodic alumina membrane by electrophoretic deposition from a nanosized ZnO suspension were reported.[24] Oxide nanorods have also been prepared in polycarbonate, and a membrane was attached to the electrode by electrophoretic deposition 25. The combination of electrophoretic deposition and a mold seems very useful for preparing nanometer-sized arrays because nanometer-sized pillars fabricated in orderly patterns, can be applied to 2-D PCs.[26, 27]

Electron beam lithography was used to form an orderly array of nanometer-sized air holes in the mold. Figure 2.5(a) shows a cross-section FE-SEM photograph of the electron beam resist mold. The dot arrays of the mold have a diameter of 250 nm and a height of 750 nm. Figure 2.5(b) shows a top surface FE-SEM photograph of the mold. The dots of the mold in this image also have diameters of 250 nm and a triangular lattice spacing of 500 nm.

Figure 2.6 shows a tilted (15˚) side view of the FE-SEM photograph of patterned gel. Deposition was carried out at 6 V with deposition times of 1 min, 5 min, 10 min, and 60 min. Sol was deposited not only from the bottom but also from the side of the mold. Growth from the side of the mold is saturated after 10 min of deposition, and the deposition to increase the density of the pillar arrays proceeds after 10 min. Figure 2.7 shows a tilted (15˚) side view of the FE-SEM photograph of patterned gel deposited for 60 min, after deposited for 60 min dense pillar arrays are obtained.

The deposition process seems to have two steps. Schematic growth model is shown in figure 2.8. In the first step, the suspension fills the mold through the action of capillary phenomena. The particles in the sol precipitate on the side and the bottom of the mold. In the second step, the sol particles are deposited from the bottom through the application of an electric field. Particles fill the mold as the deposition proceeds.

Hollow pillars seen in figure 6(a), 6(b) and 6(c) have a hole on the top. This is because a hollow pillar does not have enough mechanical strength to hold the top film after the aging process. Thus, if the pillar is hollow, its top must have a hole; i.e. dense solid

pillars will not have holes. The tops in figure 4(d) do not have a hole. This shows that dense solid pillar arrays had been obtained.

The FE-SEM photograph of the patterned gel in figure 2.7(a) is a side view tilted at an angle of 15˚. The pillars of the array have a diameter of 250 nm and a height of 750 nm, and an aspect ratio of 3. The pillar array stood on the Pt substrate without cracks. Figure 2.5(b) shows an FE-SEM photograph of the top view of the barium titanate patterned microstructures. The pillars have a diameter of 250 nm and are formed into a triangular lattice with a spacing of 500 nm. The mold and the pillar array are similar in height and shape. It is evident that the mold is filled to the top with the gel. This is because the barium titanate particles are nanometer sized and homogeneously dispersed in the suspension, as reference [20] reported. Thus, the pillar arrays were able to fabricate by changing the shape of the mold.

FIB was used to cut pillars on the pillar array. Figure 2.9(a) and 2.9(b) show SIM images of the pillar array before and after cutting with FIB respectively. The cutting plane is smooth and is not collapsed. If the pillars were hollow, their cutting plane would have collapsed. Figure 2.6(c) shows a tilted (60˚) view of the SIM image of the array after cutting with FIB. In figure 2.9(c), the surface of a cutting plane does not reveal holes. If the pillar arrays are hollow, holes would appear in the cutting plane. These results indicate that a dense solid pillar array was obtained.

The mole ratio of barium and titanium in the gel, as analyzed by ICP-AES, was Ba : Ti = 49.9 : 50.1 indicating that the composition of the gel film and the sol is the same.

Figure 2.10 shows an XRD pattern of the gel after aging at 150 °C. The XRD pattern shows that only the cubic barium titanate phase is present and no other phase like $BaCO_3$ is detectable. ICP-AES and XRD observations also showed that the pillars contain crystallized cubic barium titanate and no other secondary phases are present.

The Γ-M and Γ-K directions, which were tied to symmetry points in the Brillouin zone corresponding to the hexagonal array, are shown in figure 11(b). The in-plane reflection spectra for the BT film with a hexagonal array of air-holes with incident light along the Γ-K and Γ-M direction for both transverse electric (TE) and transverse magnetic (TM) polarization are shown in figure 2.12(a) and 2.12(b). The light frequencies were normalized by the period of the hexagonal array. The obtained reflectivity peaks were normalized by their backgrounds. Along the Γ- K direction, no obvious peaks were

detected for TE and TM polarization. In contrast, along the Γ-M direction, an obvious peak for TM polarization and vague peaks for TE polarization were observed. For TM polarization, the reflection peak appeared in the frequency range from 0.57 to 0.67. However, for TE polarization, it was difficult to determine the range of frequencies; the center of the peaks may have been around 0.65 and 0.78. The photonic band structures in the patterned BT film were calculated using the values of the period and radius. The results of calculations of the hexagonal array for the TE and TM modes in the patterned BT film are shown in figure 2.14(a) and 2.14(b), respectively. The gray areas in the figure represent the calculated PBG of the arrays for each direction and polarization.

The calculated PBGs were produced only along the Γ-M direction for both TE and TM polarization. The frequency ranges of the calculated PBGs were 0.50-0.61and 0.68-0.74 (for the TE modes) and 0.54-0.58 and 0.78-0.82 (for the TM modes), respectively. Calculated and experimental photonic band structures for BT PCs in 2D case are shown in figure 2.12. A comparison of the frequency ranges of the experimental reflection spectra and those of the calculated PBGs showed that there were still small differences between the values of the frequencies. To calculate them more accurately, other parameters including the refractive index and surface plasmon of the thin Pt film and the thickness of the BT patterned film have to be considered. However, the reflection spectra obtained for the patterned BT films can be interpreted as indicating that PBGs formed in the crystals.

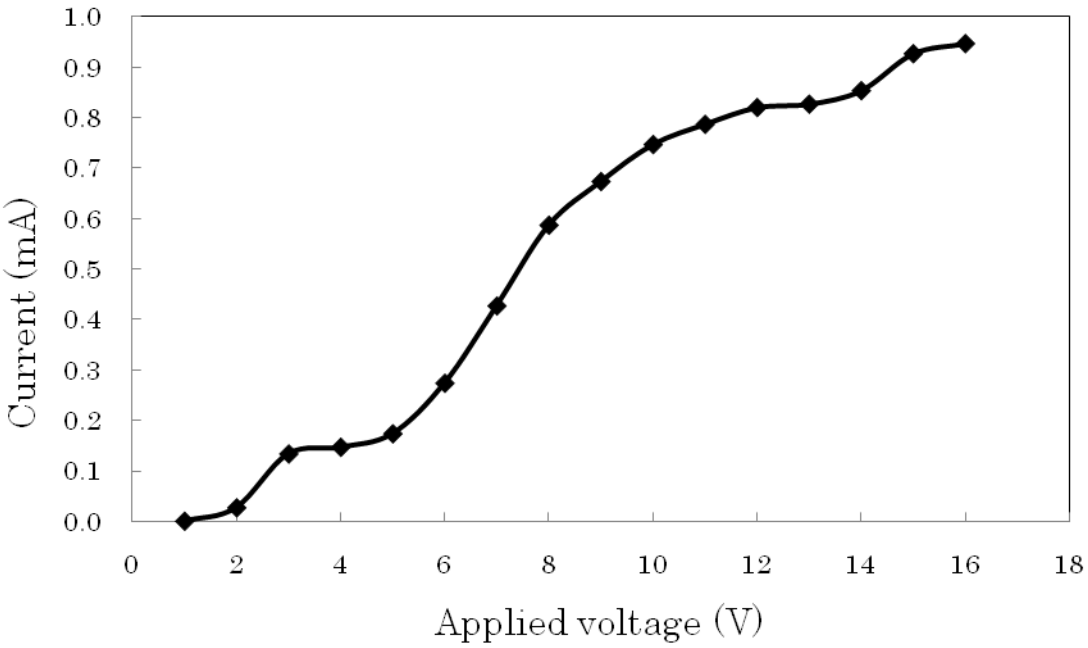

Figure 2.3 Sol-electrodeposition current plotted as a function of applied voltage for a $BaTiO_3$ sol without the addition of DMAE.

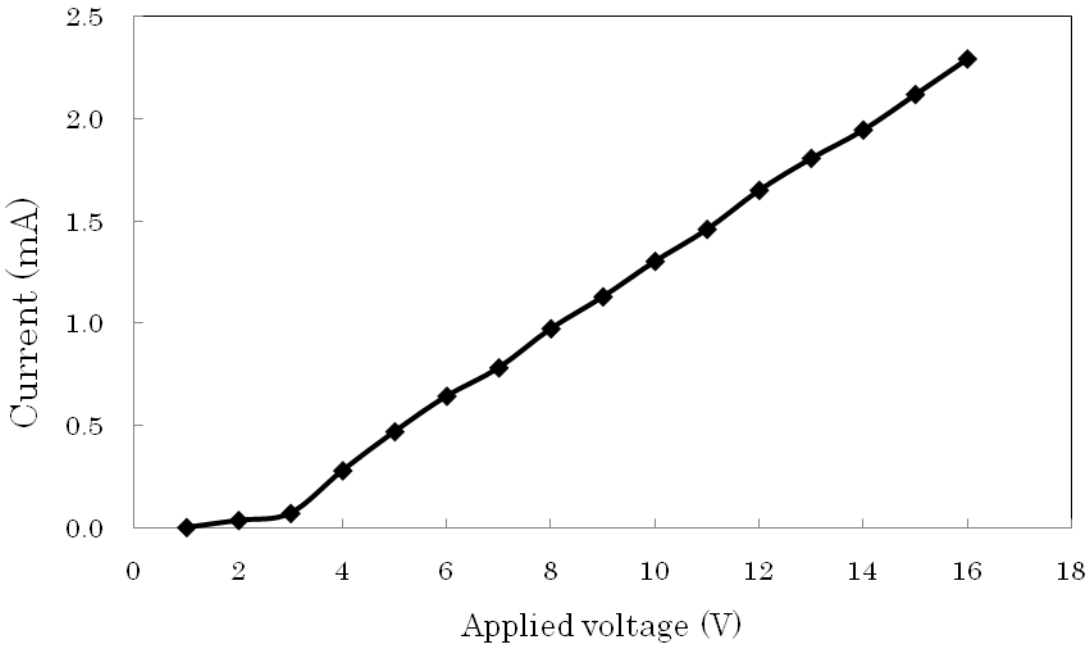

Figure 2.4 Sol-electrodeposition current plotted as a function of applied voltage for a $BaTiO_3$ sol with the addition of DMAE.

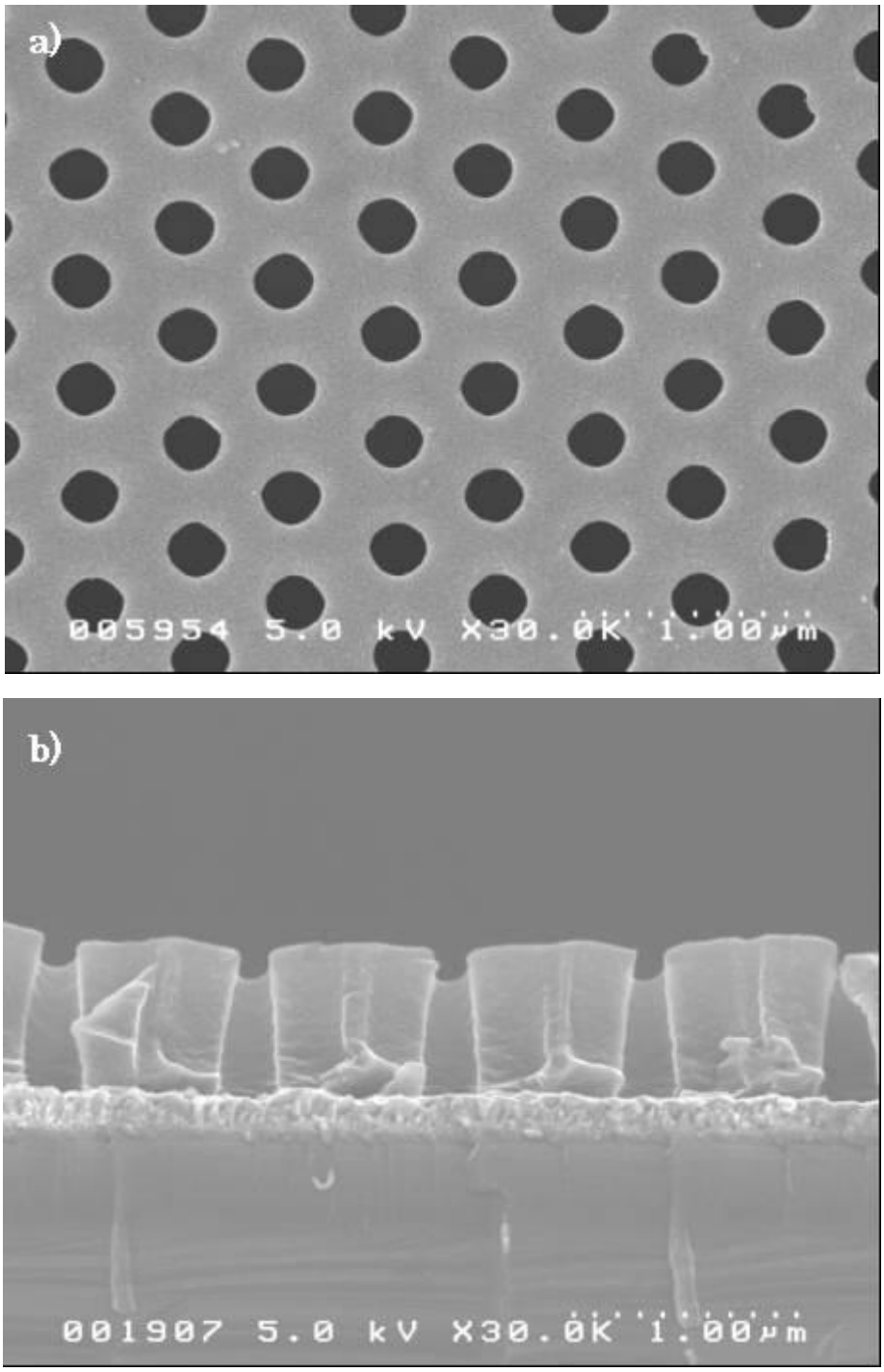

Figure 2.5 FE-SEM photographs of a resist mold prepared by electron beam lithography: (a) Cross section and (b)Top surface of the mold.

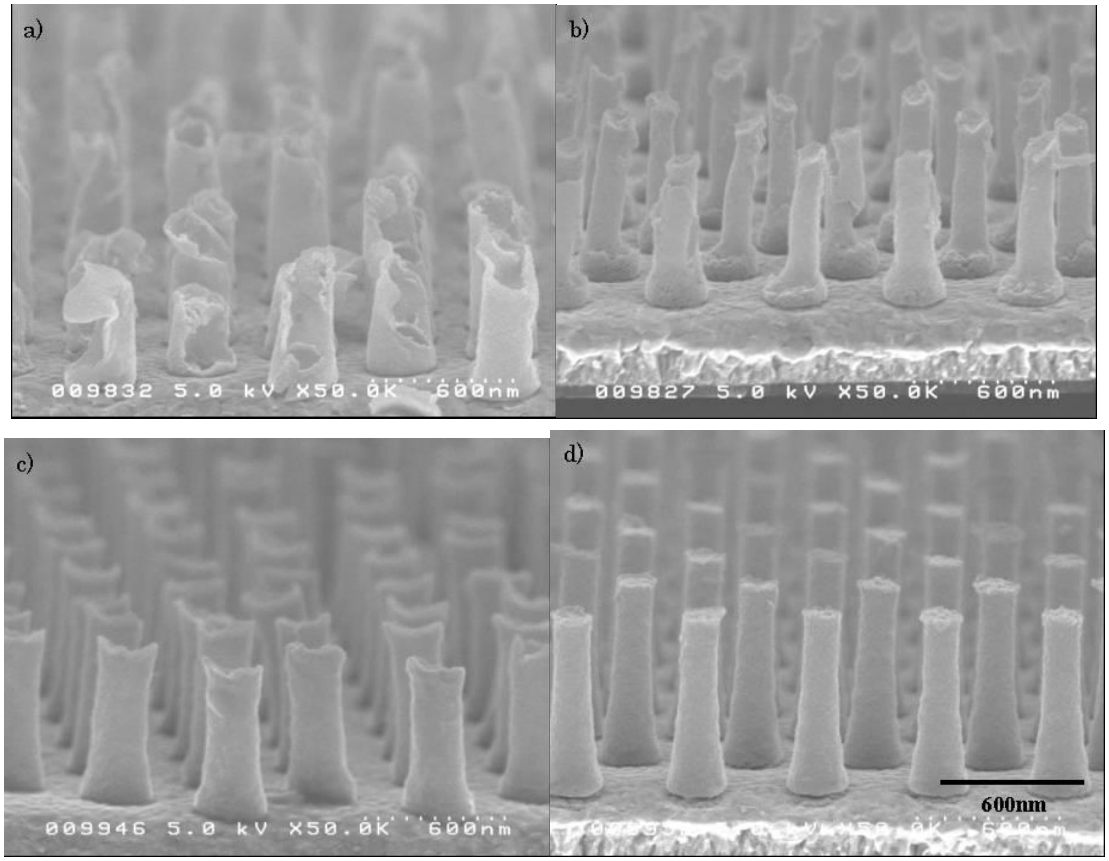

Figure 2.6 FE-SEM photographs of a patterned gel microstructure consisting of $BaTiO_3$ with the side view tilted at an angle of 15˚: deposited for (a) 1 min, (b) 5 min, (c) 10 min, and (d) 60 min.

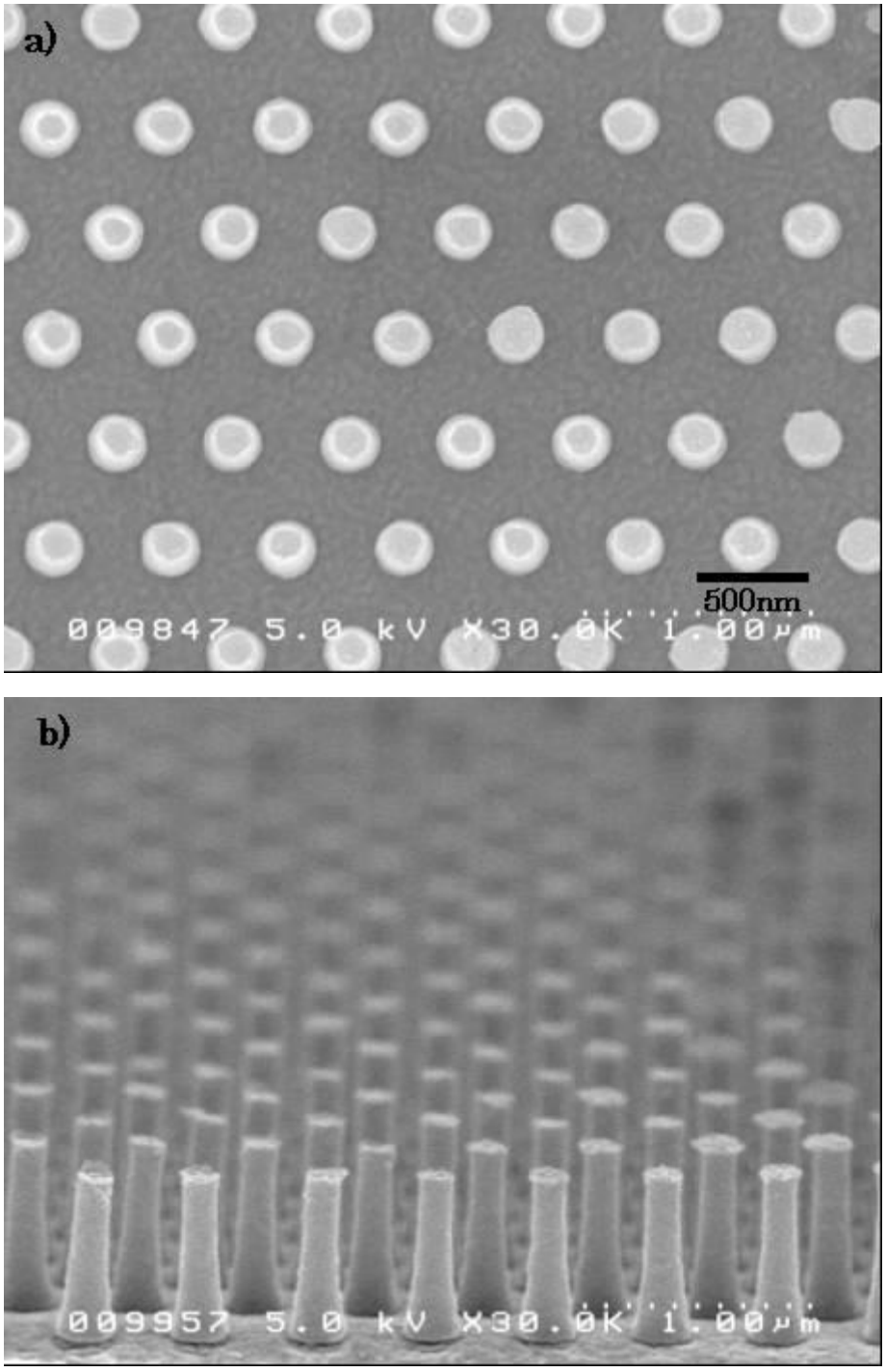

Figure 2.7 FE-SEM photographs of a patterned gel microstructure consisting of $BaTiO_3$: (a) side view tilted at an angle of 15˚ and (b) top view of the patterned $BaTiO_3$ microstructures.

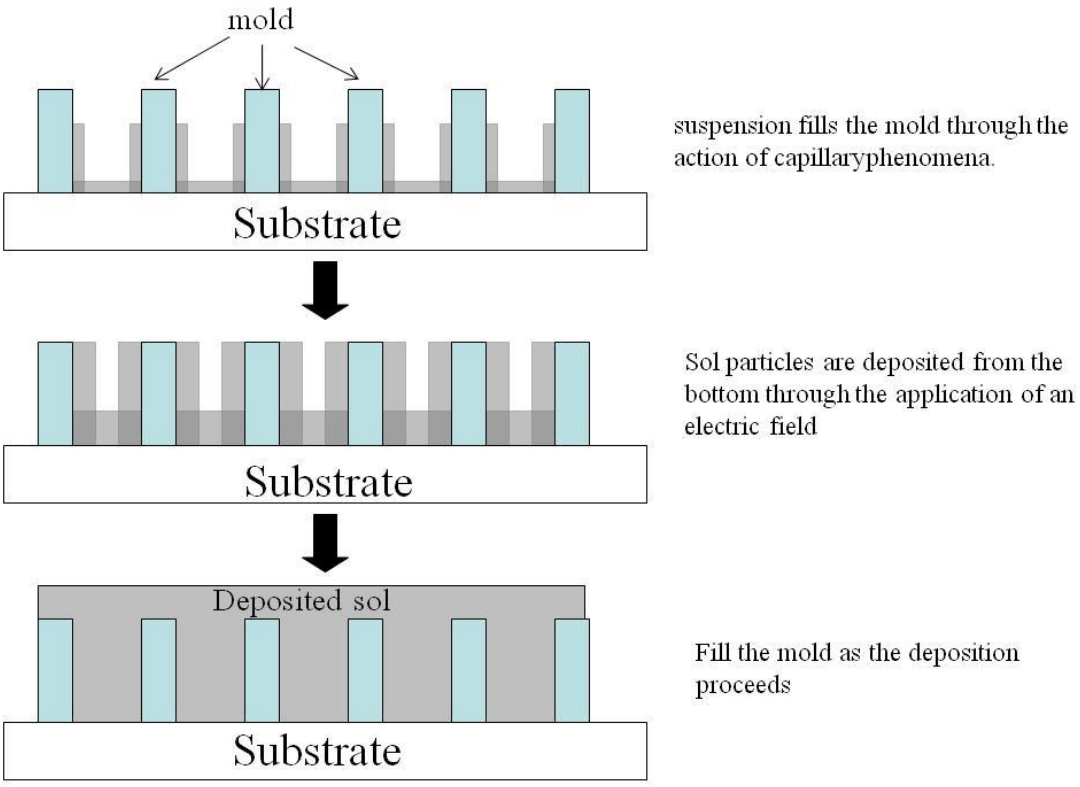

Figure 2.8 Schematic growth model of the deposition process.

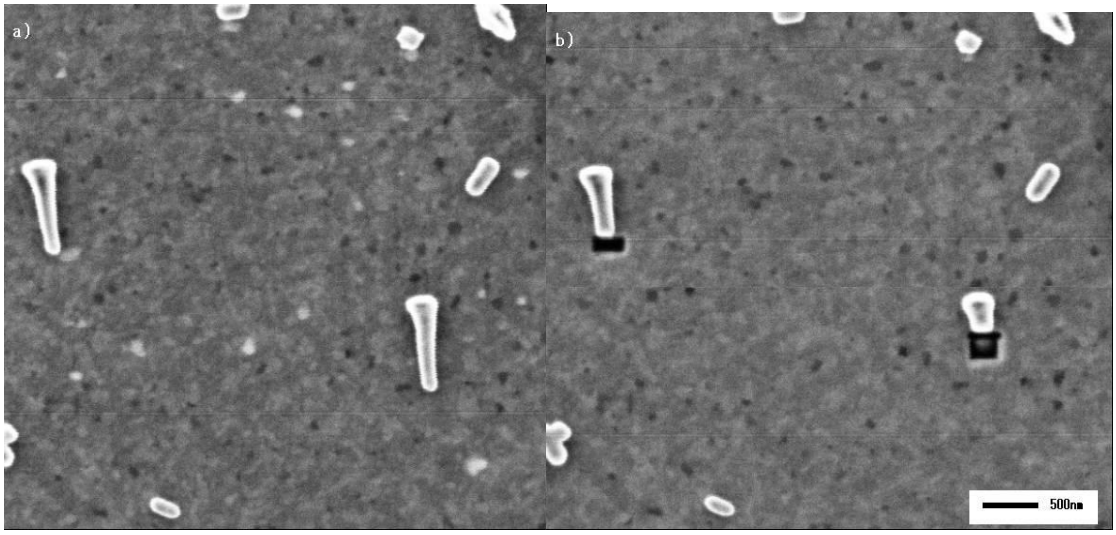

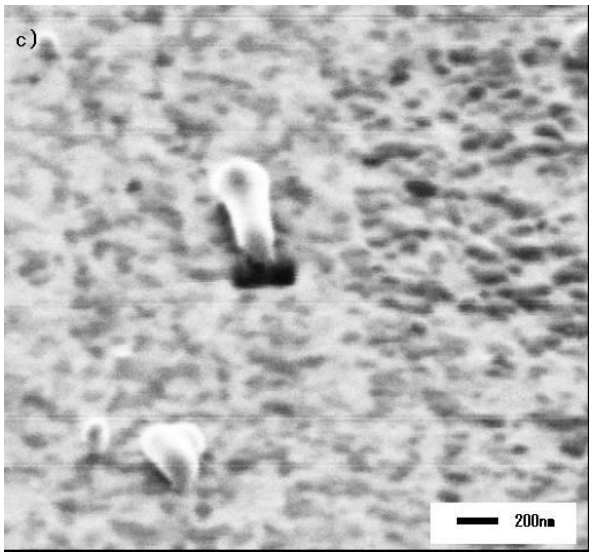

Figure 2.9 SIM images of pillar array: (a) before cutting with FIB (b) after cutting with FIB and (c) tilted at an angle of 60˚.

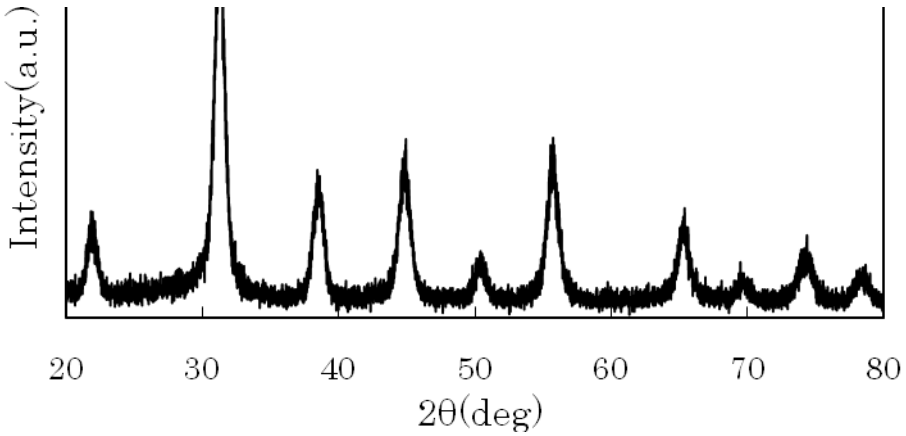

Figure 2.10 XRD pattern of the gel after aging at 150 °C.

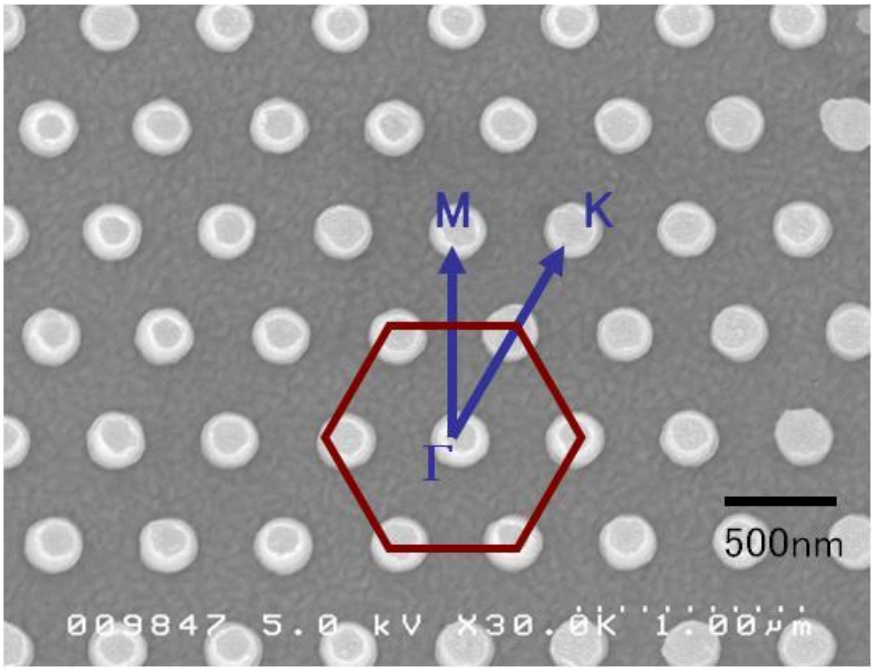

Figure 2.11 SEM image of top view of BT films with hexagonal array.

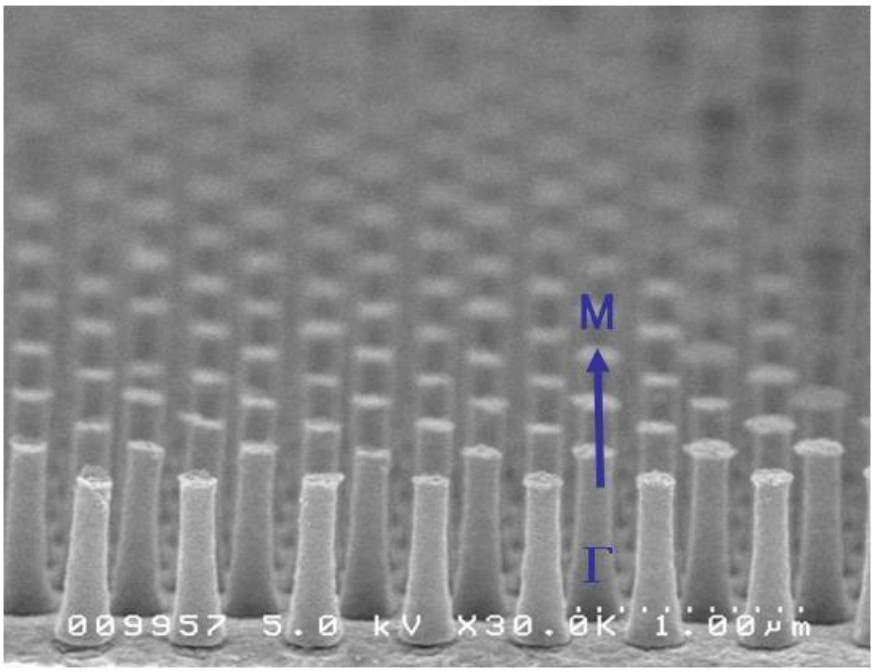

Figure 2.12 Cross-sectional SEM image of BT films with hexagonal array.

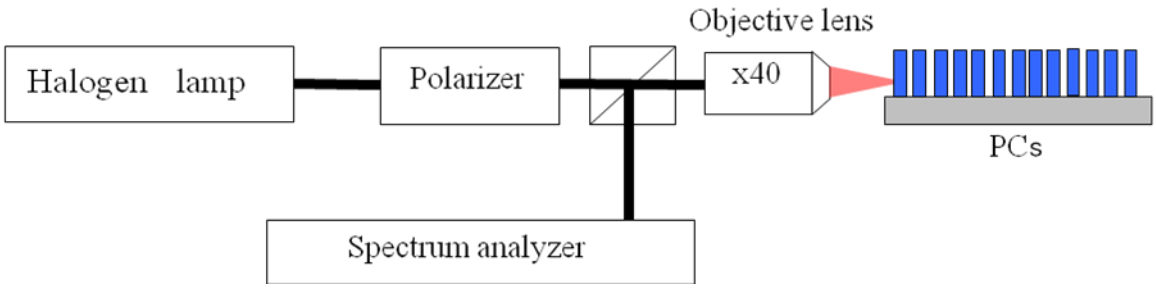

Figure 2.13 Schematic illustrations of optical reflectance measurements.

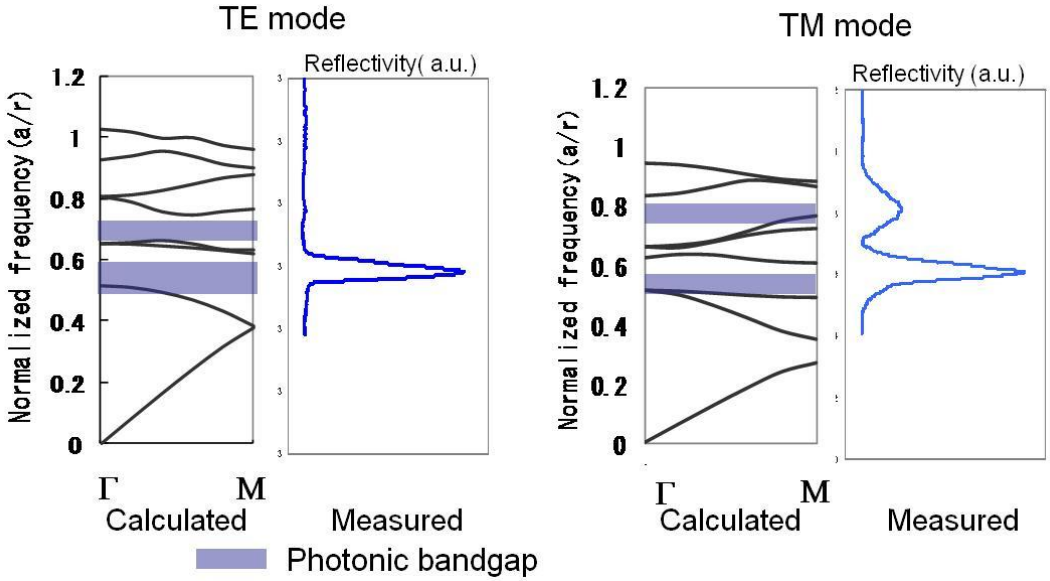

Figure 2.14 Calculated and experimental photonic band structures for BT photonic crystal in 2D case for (a) TE mode and (b), TM mode.

2.3 Conclusion

In order to prepare $BaTiO_3$ with patterned microstructure, a novel electrophoretic method that uses a partially hydrolyzed highly concentrated solution of barium and titanium alkoxides was developed. By using electron beam lithography, a micro-patterned mold, that is a mold with an array of air holes of 250 nm arranged in a triangular lattice with a lattice constant of 500 nm was prepared on a $Pt/Ti/SiO_2/Si$ substrate. Electrophoretic deposition of $BaTiO_3$ gel was carried out by negatively biasing the $Pt/Ti/SiO_2/Si$ substrate as cathode which had the resist mold on the surface. Removal of the resist mold left a gel material with a patterned structure that was transferred from the pattern of the mold. The gel material was confirmed by ICP-AES to have nearly the stoichiometric composition of $BaTiO_3$, that is, a composition in which Ba:Ti=1:1 in molar ratio. By combining high-concentration metal alkoxides sol-gel processing, an electrophoretic deposition technique, and electron-beam lithography, we have succeeded in producing barium titanate patterned microstructures. The obtained barium titanate pillars had diameters of 250 nm and a spacing of 500 nm in a triangular lattice. The reflection spectra obtained for the patterned BT films can be interpreted as indicating that PBGs formed in the crystals. Thus, this deposition technique for formation of barium titanate patterned microstructures is very promising for fabricating PCs.

2.4 References

[1] V. A. Lamb and H. I. Salmon, Am. Ceram. Soc. Bull., **41** (1962) 781.

[2] M. Nagaki, K. Yamashita, T. Umegaki and Y. Takuma, J. Am. Ceram. Soc., **76**, 253 (1993).

[3] S. Okamura, T. Tsukamoto and N. Koura, Jpn. J. Appl. Phys., **32** (1993) 4182.

[4] S. Sugiyama, A. Takagi and K. Tsuzuki, Jpn. J. Appl. Phys., **30** (1991) 2170.

[5] J. A. Lewis, J. Am. Ceram. Soc., **79** (1996) 1987.

[6] P. Sarkar and P. S. Nicholson, J. Am. Ceram. Soc., **83** (2000) 2341.

[7] K. Yamashita, M. Matsuda. Y.Inda, T. Umegaki, M. Ito and T. Okura, J.Am.Ceram.Soc., **80** (1997) 1907.

[8] M. Nagai, K. Yamashita, T. Umegaki, and Y. Takuma, J.Am.Ceram.Soc, **76** (1993) 253.

[9] T. Ishihara, K. Sato, Y. Mizuhara, and Y. Takita, Chem. Lett., **2** (1992) 942.

[10] T. Ishihara, K. Sato, T. Kudo, and Y. Takita, Proceedings of 3rd International Symposium on solid oxide fuel cells,.**93** (2005) 65.

[11] C.E. Baumgarner, V. J. DeCarlo, P. G. Glugla, and J. Grimaldi. J. Electrochem. Soc., **132** (1985) 87.

[12] H. Uchikawa, S. Matsuno, and S. Kinouchi, Jpn. Patent Pending, H05-163005 (1993).

[13] K. Kishida, M.Tatsumisago and T. Minami, J. Ceram. Soc. Japan, **102** (1994) 336.

[14] K. Hasegawa, M.Tatsumisago and T. Minami, J. Ceram. Soc. Japan, **105** (1997) 569.

[15] K. Hasegawa, M.Tatsumisago and T. Minami, J. Mater. Sci., **33** (1998) 1095.

[16] J. Laubersheimer, H. -J. Ritzhaupt-Kleissl, J. Haubelt and G. Emig, J. Europ. Ceram. Soc., **18** (1997) 255.

[17] S. Okamura, T. Tsukamoto and N. Kobayashi Jpn. J. Appl. Phys., **32** (1993) 4182.

[18] H. Shimooka and M. Kuwabara, J. Am. Ceram. Soc., **78** (1995) 2849.

[19] H.Shimooka, K.Yamada, S.Takahashi and M.Kuwabara, J.Sol-Gel Soc. & Technol., **13** (1998) 873.

[20] S. Shindo and M. Kuwabara, J. Ceram. Soc. Japan, **110** (2002)1035.

[21] S. Y. Chou, M. S. Wei, Peter R. Krauss, and P. B. Fisher, J. Appl. Phys, **76** (1994) 6673.

[22] N. Ogata, J Van Tassel, C. A. Randall, Materials Lettres, **49** (2001) 7.

[23] Poborchii, V. V., Tada, T. and Kanayama, T., J. Appl. Phys., **91** (2002) 3299.

[24] Y. C. Wang, I. C. Leu, M. and H. Hon, Journal of Crystal Growth, **564** (2002) 237.

[25] S. J. Limmer, S. Seraji, Y.Wu, T. P. Chou, C. Nguyen and G. Cao, Adv. Funct. Mater. , **59**, (2002) 12.

[26] E.Yablonovich, Phys. Rev. Lett., **58** (1987) 2059.

[27] J. D. Jannopoulos, R. D Meade and J. N. Winn, *Photonic Crystals* (Princeton University Press, Princeton (1995)

Chapter 3

Fabrication and characterization of $(Ba,Sr)TiO_3$ thin films by CSD method

3.1 Introduction

Barium strontium titanate (BST) crystals, ceramics, and thin films have been increasingly desired as ferroelectric materials; ferroelectric memories, multilayer capacitor, optical modulator and so on[1]. Recently, high quality ferroelectric thin films have been used for advanced microwave signal processing devices. Small compact low power microwave devices that can be fabricated from structures based on ferroelectric films include phase shifters, tunable filters, tunable resonators, phased array antennas, and frequency agile microwave radio transceivers. Thin films of BST meet most of the device requirements due to their unique combination of properties. Thin films of BST have been prepared by various techniques such as r.f.-sputtering[2], laser ablation[3, 4], metal-organic chemical vapor deposition (MOCVD)[5] and chemical solution deposition (CSD) processing[6,7]. Among these methods, CSD processing has an edge over other deposition techniques in terms of good homogeneity, chemical composition control, high purity, low processing temperature, and applicable large areas, using simple and inexpensive equipment. In this study, CSD processing has been used to deposit BST thin films on $Pt/BST/SiO_2/Si$ substrates. The films were characterized by different analysis and electrical measurements.

Recently, there have been some studies on the preparation of the BST thin films. From a material point of view, BST is the solid solution of $BaTiO_3$ and $SrTiO_3$. $BaTiO_3$ is a ferroelectric material with the Curie temperature Tc of 120°C, while $SrTiO_3$ is paraelectric material with no ferroelectric phase transition. Therefore, Tc of BST can be suitably controlled by adjusting the ratio of Ba to Sr. At room temperature; it is known that the solid solution system is in a ferroelectric phase when Ba content is in a range of 0.7-1.0, and in a paraelectric phase when Ba content is less than 0.7. Further, very limited information has been known on the kinetics of perovskite phase formation. TG-DTA measurement under changing heating rate enables to express the decomposition and the crystallization reaction of CSD solution by using thermal dynamic method. This method implies that heating- rate may effect to the morphology and the dielectric properties of the BST film prepared by

CSD method.

3.2 Fabrication and electrical characterization of one-axes oriented epitaxially grown (Ba,Sr)TiO_3 thin films prepared by sol-gel method

Precursor solution was prepared by dissolving $Ba(CH_3COO)_2$, $Sr(CH_3COO)_2$ and $Ti(O\text{-}i\text{-}C_3H_7)_4$ with a molar ratio of 70 : 30 : 100 in a mixed solvent of acetic acid and ethylene glycol monoethyl ether (EGMME). Illustration of the preparation for the BST precursor solution is shown in figure 3.1. Precursor solutions deposited by spin-coating on platinum coated silicon substrates, i.e. 100 nm Pt (111)/20 nm (Ba,Sr)TiO_3 /1000 nm SiO_2 /(100) Si-wafer. Schematic flow of the precursor solutions deposition is shown in figure 3.2. This solution was dispersed on the substrates and then spin coated at 4000 rpm for 30 s. Spin coated films were sintered at 600 °C, 700 °C and 800 °C for 20 min at heat rate of 300 °C/min. In order to prepare thicker (Ba,Sr)TiO_3 films, a multilayer deposition procedure was followed. Pt dots with a diameter of 0.5 mm were sputtered by placing a mask on the film to form metal–dielectric–metal (MDM) capacitors. Schematic illustration of the metal–dielectric–metal (MDM) structured BST capacitor is shown in figure 3.3

Cross section images of the obtained films were taken with a field emission-scanning electron microscope (FE-SEM) and transmission electron microscope (TEM). Crystal characterization was done by X-ray diffraction (XRD). Several Pt dots were evaporated through a mask on the film to form metal–ferroelectric–metal (MFM) capacitors. Small signal ac (100 mV, 1 kHz) capacitance, loss tangent, and ac conductivity were measured with HP 4284A LCR meter. Capacitance–voltage (C-V) measurements were done with HP 4284A LCR meter.

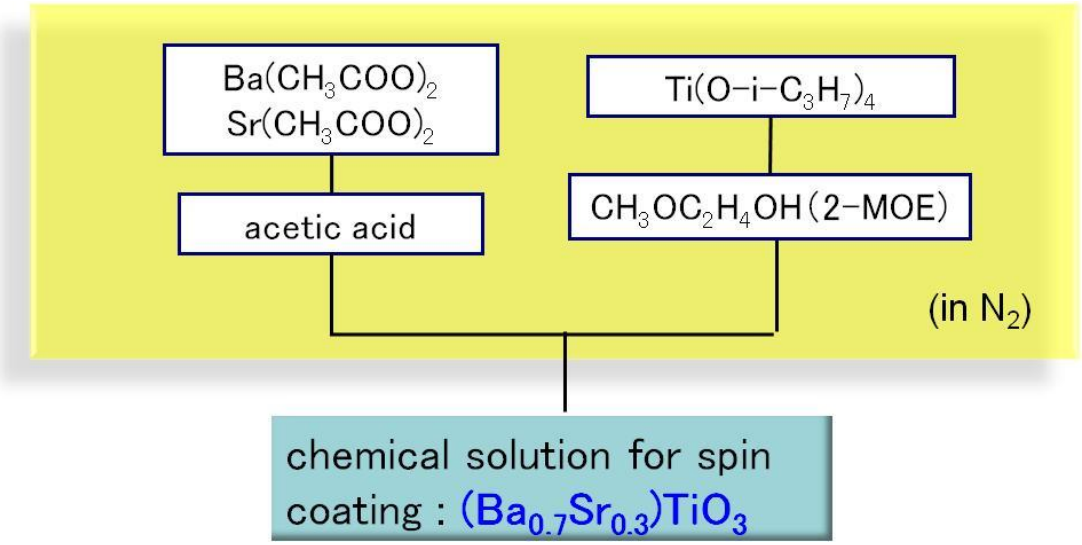

Figure 3.1 Illustration of the preparation for the BST precursor solution.

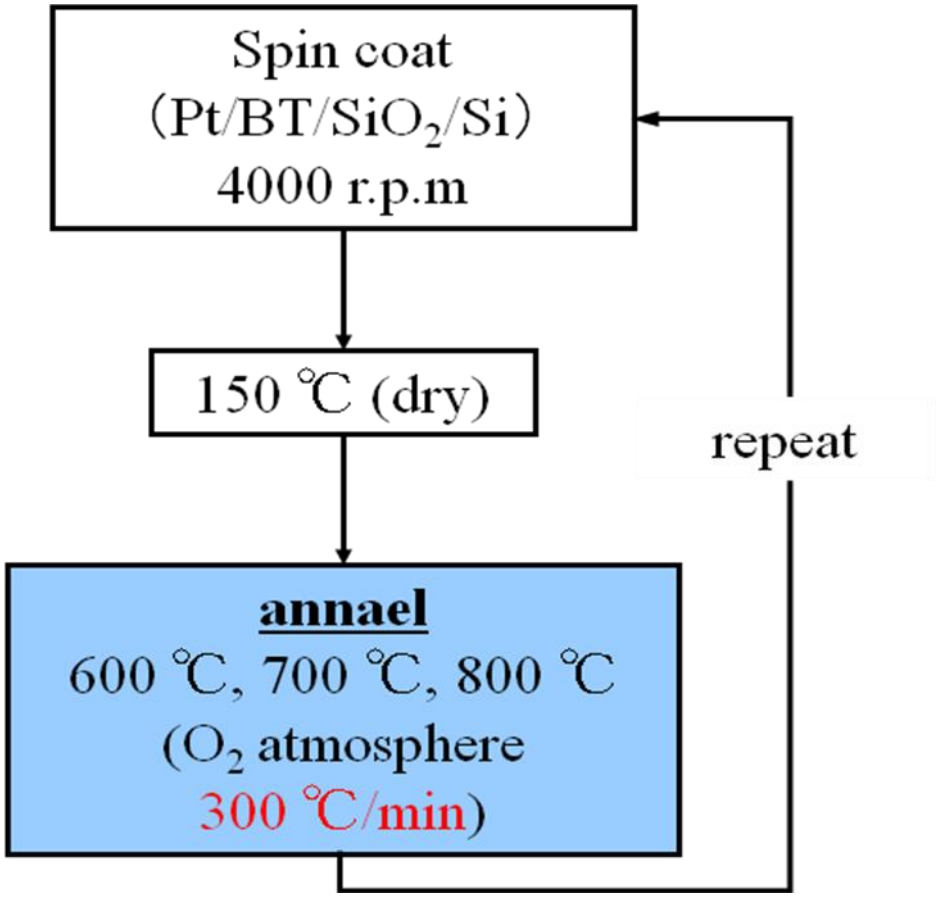

Figure 3.2 Schematic flow of the precursor solutions deposition.

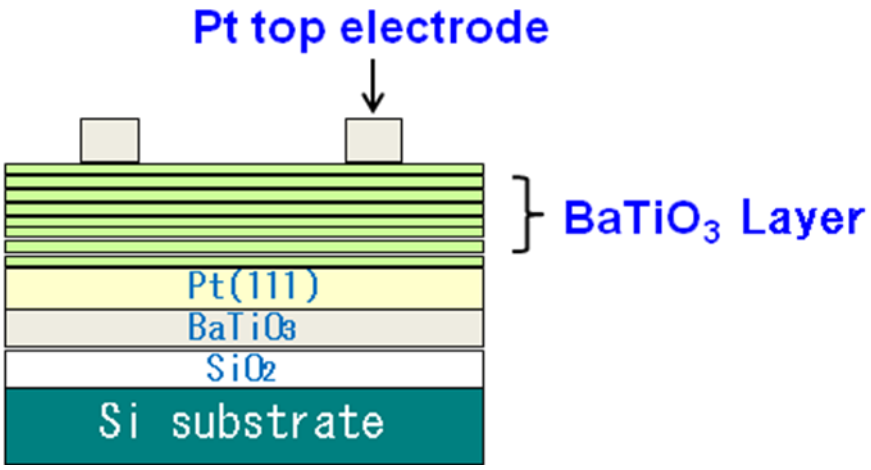

Figure 3.3 Schematic of the metal–dielectric–metal (MDM) structured BST capacitors.

Figure 3.4(a) shows the film annealed at 600 °C is composed of 20 nm average-sized particles. Figure 3.4(b) shows the cross sectional SEM image of the film annealed at 700 °C. The film annealed at 700 °C is composed of 40 nm average-sized particles. Particle size grows as annealing temperature rises. Figure 3.4 (c) shows the cross sectional SEM image of the film annealed at 800 °C. The film annealed at 800 °C is composed of columnar grains. Figure 3.4 (d) shows the cross sectional SEM image of the film annealed at 800 °C after the film was prepared at 600 °C. The film annealed at 800 °C after the film was prepared at 600 °C is composed of 60 nm average-sized particles. This indicates that grain growth occurs after crystallization occurred. The morphology of the films was found to depend on the annealing condition. Crystallization occurred annealing at 600 °C. Morphology of the film changes from fine particles to columnar grains above annealing temperature of 800 °C. Annealing after film was crystallized, crystallized fine grain growths instead of occurring columnar grain growth.

These results indicate that columnar grain growth occurs when annealing condition is above decomposition temperature and crystallize temperature.

Figure 3.5(a) shows XRD pattern of BST thin film annealed at 600 °C on Pt(111)/BST/SiO_2/Si substrate. XRD pattern of BST thin film annealed at 600 °C shows typical poly-crystal perovskite diffraction spectra. Figure 3.5 (b) shows XRD pattern of BST thin film annealed at 800 °C on Pt(111)/BST/SiO_2/Si substrate. XRD pattern of BST thin film annealed at 800 °C shows that the columnar grains induce a higher degree of

oriented growth. The columnar grown film exhibits a preferred (111) orientation that follows the (111) orientation of Pt substrate.

Figure 3.6 shows the cross sectional TEM images of the film annealed at 800 °C. Bright field TEM image (figure 3.6a) shows columnar grain growth with a grain size of 250 nm. Dark field TEM image (figure 3.6b) indicates that a single columnar grain seen in bright field image is consisted of a single crystal.

The nonlinear dielectric ferroelectric properties of the sol-gel grown BST films were studied by observing the variation of the capacitance at different bias voltages of the films annealed at 600 °C and 800 °C (figure 3.7). A small ac signal of 100 mV was applied and the dc field was swept from negative bias to positive bias and back again. Figure 3.7 (a) and 3.7 (b) show the C-V plot for the films at 1 kHz. Measurement of the C-V in MFM configuration demonstrates the ferroelectric properties and gives the information about domain switching, although there is no exact determination of spontaneous polarization and remnant polarization. The two maximums, which are due to the ferroelectric polarization reversal, are clearly seen in figure 3.7 (a) and 3.7 (b). These butterfly loops are an indication of ferroelectricity in the film. At the zero bias, dielectric constant of the film annealed at 600 °C is around 550, and dielectric constant of the film annealed at 800 °C is around 2000. Dielectric constant of the film annealed at 700 °C is around 900 and dielectric constant of the film annealed at 800 °C after the film was prepared at 600 °C is 1200 respectively.

Above results can be explained based on the morphology as determined by SEM and TEM analysis. The film annealed at 600 °C and 800 °C differs in the morphology. Dielectric constant of the film consisted of columnar grains is higher than dielectric constant of the film consisted of nano-sized particles. These results indicate that the columnar grains induce a higher dielectric constant.

The temperature dependence of the dielectric constant in the films annealed at 600 °C and 800 °C is sown in fig. 3.9.The dielectric constant was measured at 1 kHz, with 0.1 V at zero-biased from -60 °C to 150 °C. Temperature dependence of the capacitance of the film heat treated at 600 °C was stable from -50 °C to 40 °C and decreased continuously with increasing temperature above 40 °C. This change at 40 °C is corresponded to some kind of a phase transition. The dielectric constant of the film heat treated at 800 °C constant capacitance continuously increase from -50 °C to 40 °C from 10 nF to 12 nF, then decreased continuously with increasing temperature above 40 °C from 12 nF to 6 nF with

increasing temperature. The film heat treated at 800 °C shows ferroelectric behavior though BST is dielectric materials. This was affected to the grain growth of the BST thin film. In spite of, the CSD method being kinetically limited as compared with physical vapor deposition (PVD) method, $(Ba_{0.7}Sr_{0.3})TiO_3$ three-axis-oriented thin films can be obtained by selecting optimum type of substrate and optimum conditions for epitaxial growth by the CSD method.

It is important to reveal the decomposition and crystallization temperature by thermo dynamical method to control the structure and properties of the BST thin films.

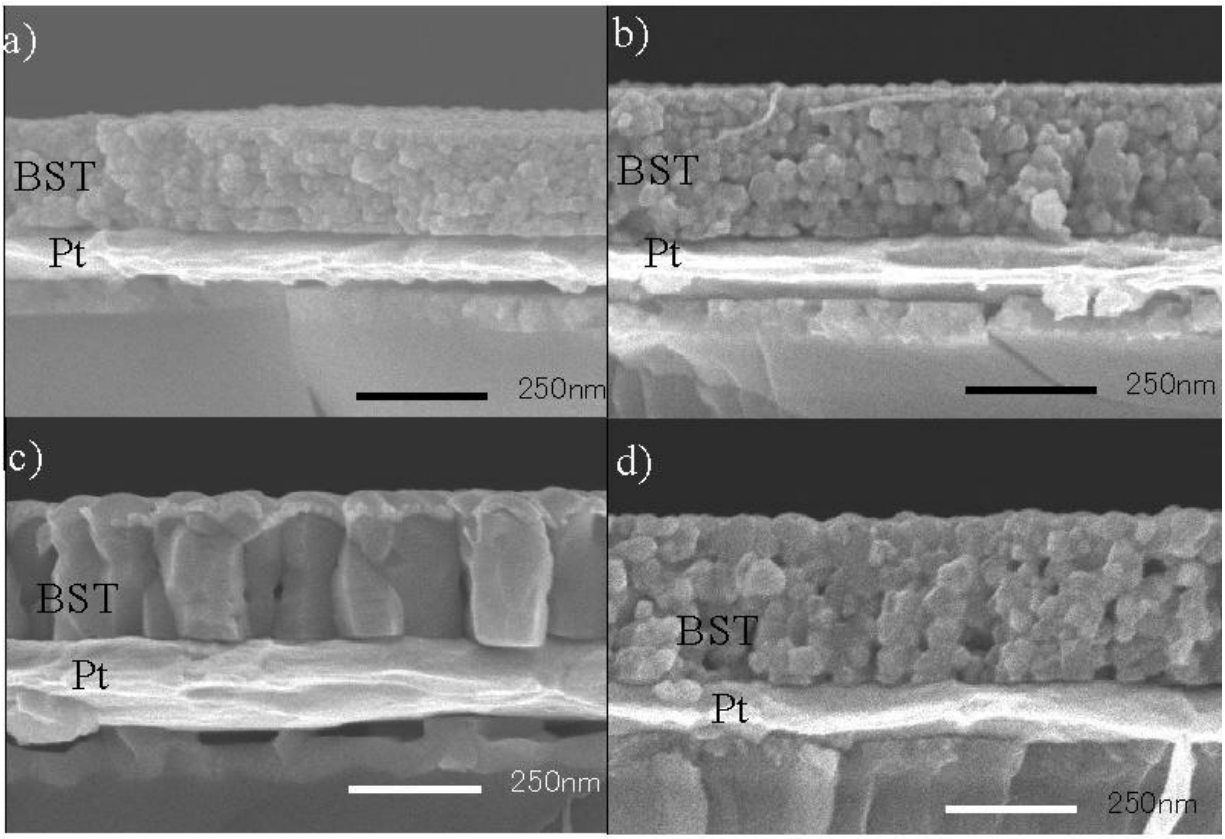

Figure 3.4 Cross sectional SEM image of the film: a) annealed at 600 °C, b) annealed at 700 °C, c) annealed at 700 °C and d) annealed at 800 °C after the film was prepared at 600 °C.

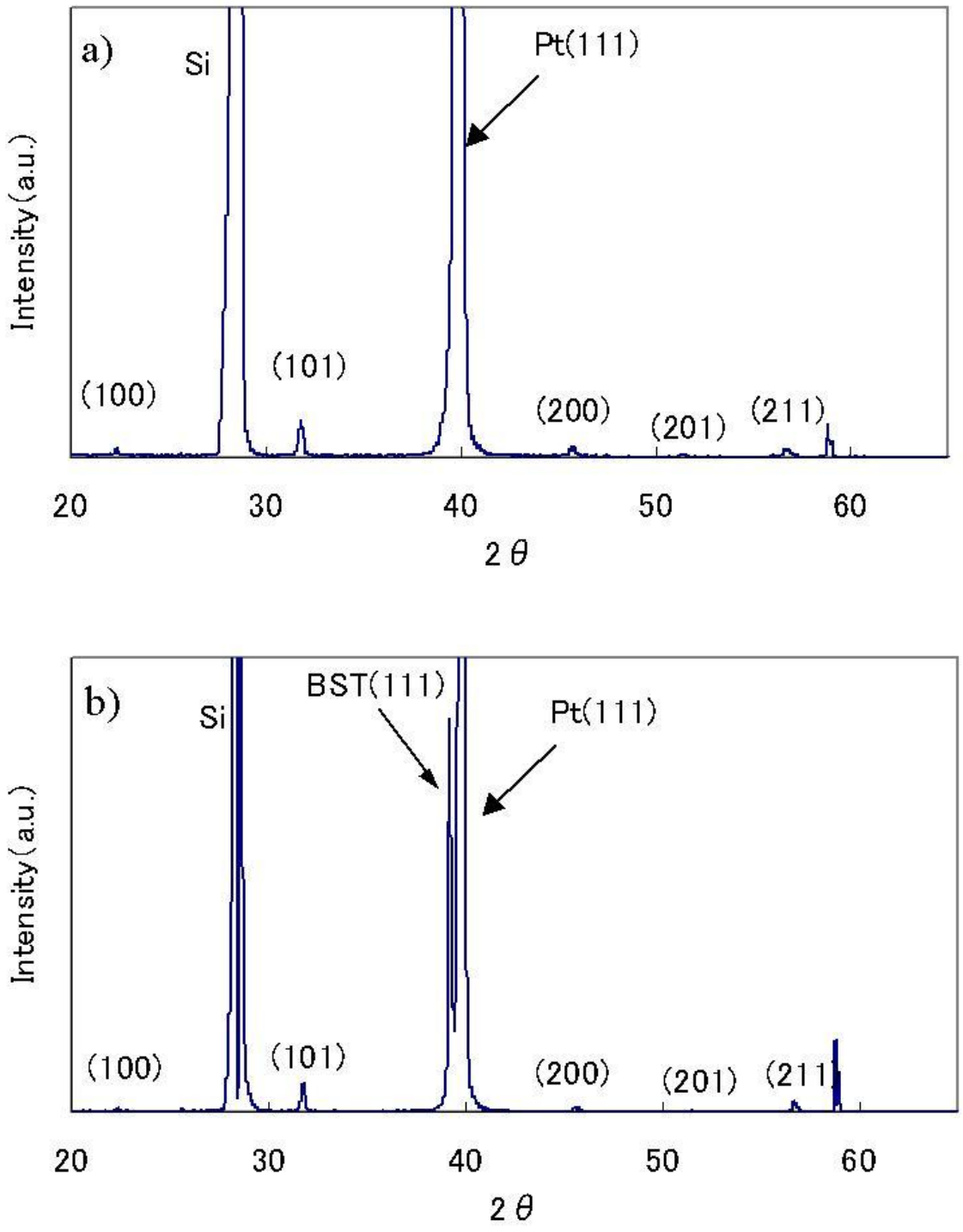

Figure 3.5 XRD diffraction XRD pattern of BST thin film: a) annealed at 600 °C on Pt(111)/BST/SiO_2/Si substrate and b) annealed at 800 °C on Pt(111)/BST/SiO_2/Si substrate.

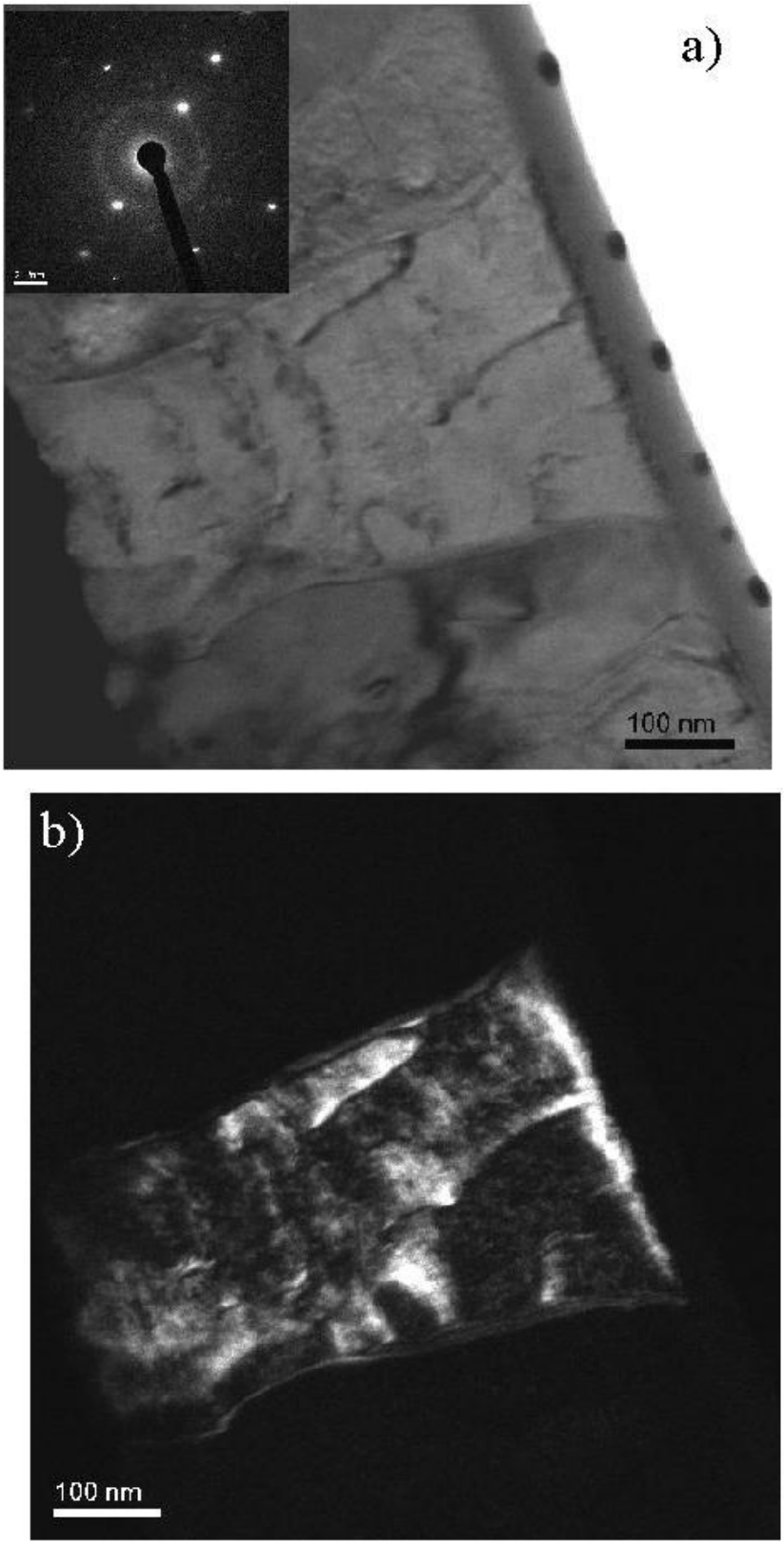

Figure 3.6 a) Bright field and b)Dark field TEM image of (Ba,Sr)TiO_3 thin film annealed at 800 °C.

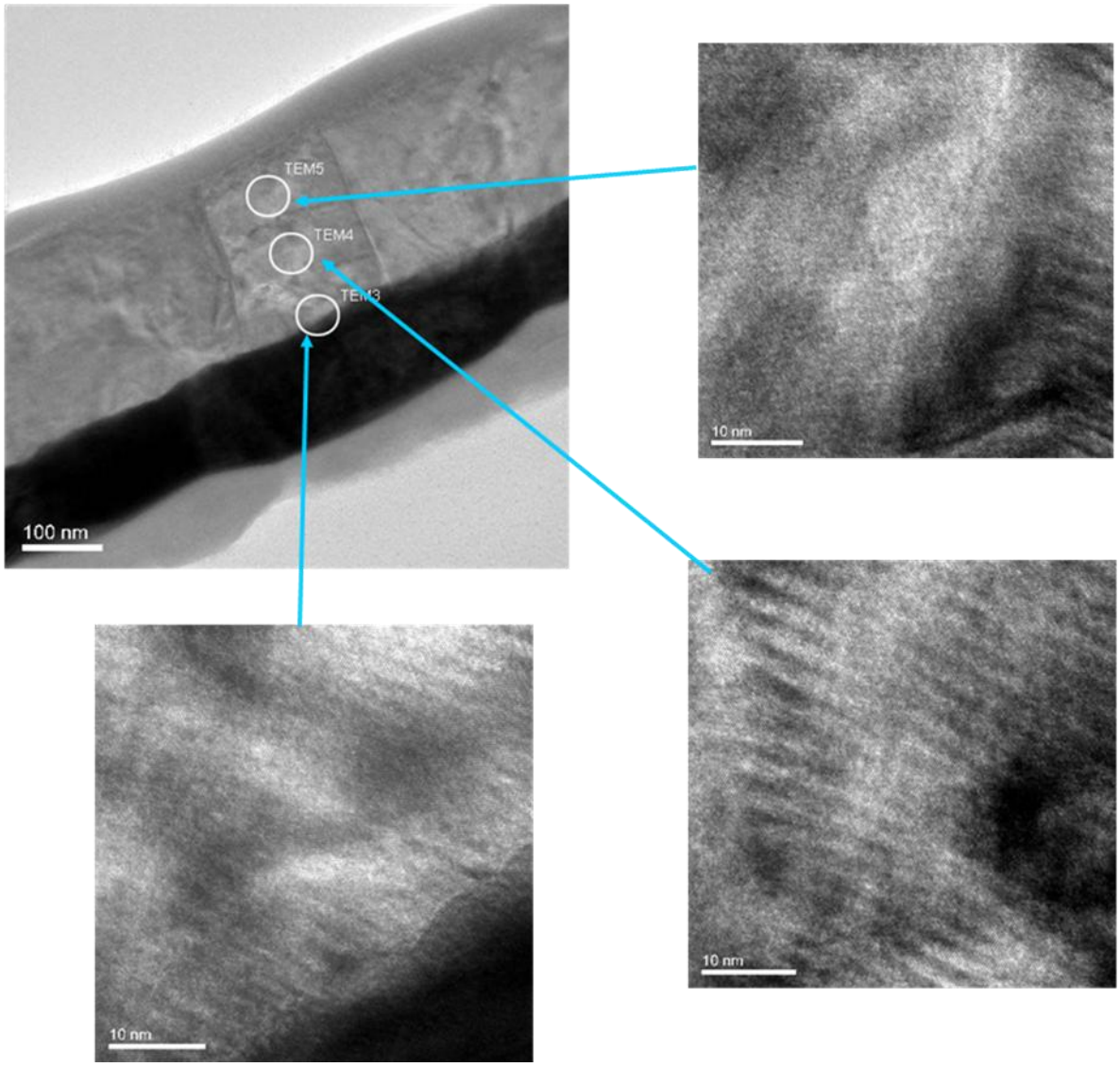

Figure 3.7 Bright field TEM images of (Ba,Sr)TiO_3 thin film annealed at 800 °C.

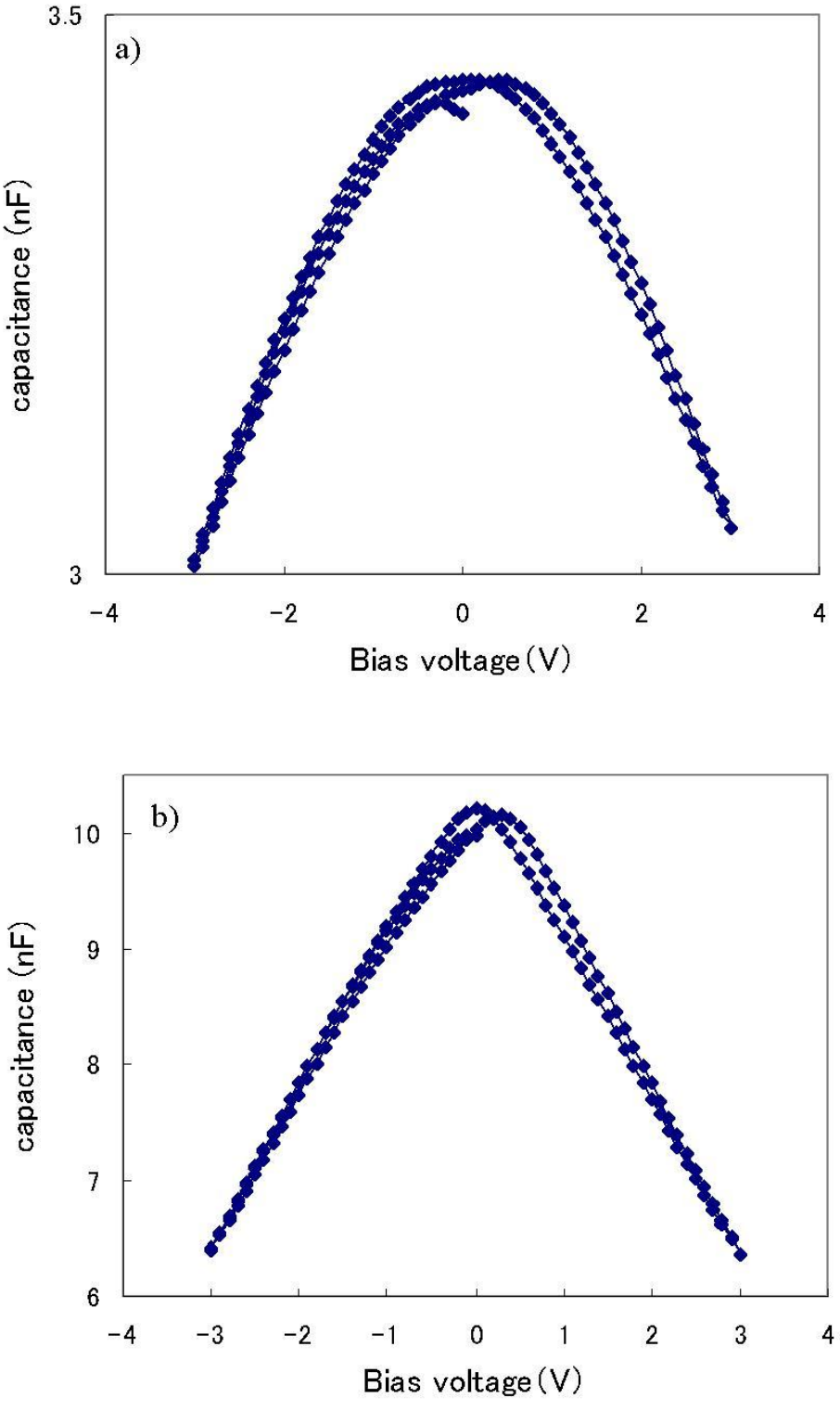

Figure 3.8 C-V plot for the films at 1 kHz: a) annealed at 600 °C and b) annealed at 800 °C.

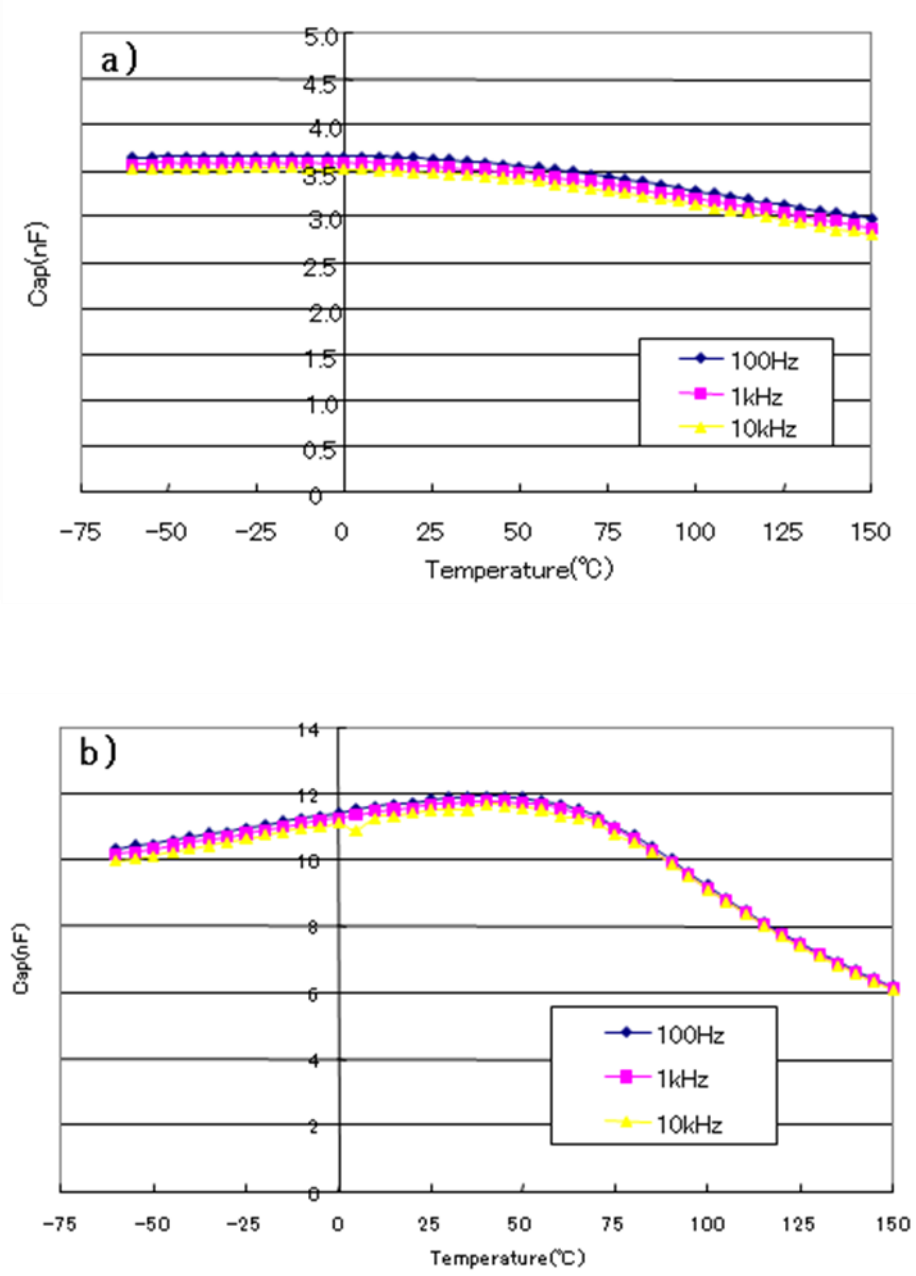

Figure 3.9 Temperature dependence of dielectric constant in the BST film annealed at a) 600 °C and b) 800 °C.

3.3 Crystallization and decomposition kinetics of $Ba_{0.7}Sr_{0.3}TiO_3$ CSD films

Though it is very important to express the decomposition and the crystallization reaction of CSD solution by using thermal dynamic method, very limited information has been known on the kinetics of perovskyte phase formation.[8.9] The aim of this research is to study the crystallization behavior of BST, to determine some important parameters in the kinetic equations that described the process of crystallization, and further, to prepare BST thin films. A chemical solution was prepared by dissolving $Ba(CH_3COO)_2$ and $Ti(O\text{-}i\text{-}C_3H_7)_4$ in a 1:1 molar ratio in a mixed solvent of acetic acid and ethyleneglycol monoethylether. The concentration of the solution was 0.3 M. Prepared CSD solution was dried at 150 °C by hotplate to obtain dry-gel. Dry-gel was kept under vacuum dryer for 12h. TG-DTA measurement was carried out to investigate the decomposition temperature and crystallization temperature. TG-DTA was performed under air atmosphere flow late of 200ml/min at temperature from 100°C to 700°C at a heating rate of 5 °C /min, 10°C /min, 15 °C /min, 30 °C /min, and 50 °C /min. (figure 3.10 - 3.14)

Decomposition temperature and crystallization temperature was determined when the DTA derivative value is 0.

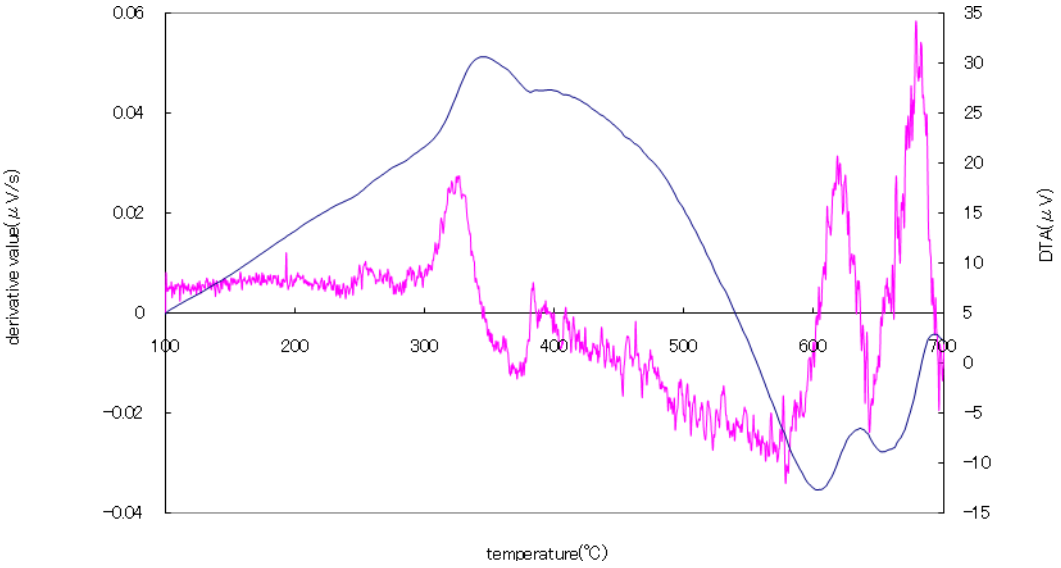

Figure 3.10 DTA curve and derivative curve at a heating rate of 5 °C /min.

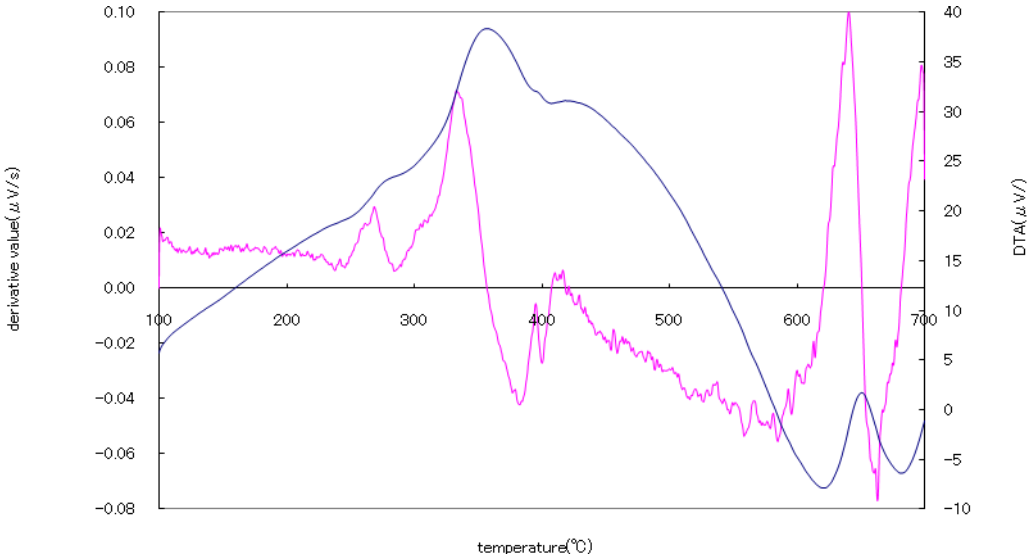

Figure 3.11 DTA curve and derivative curve at a heating rate of 10 °C /min.

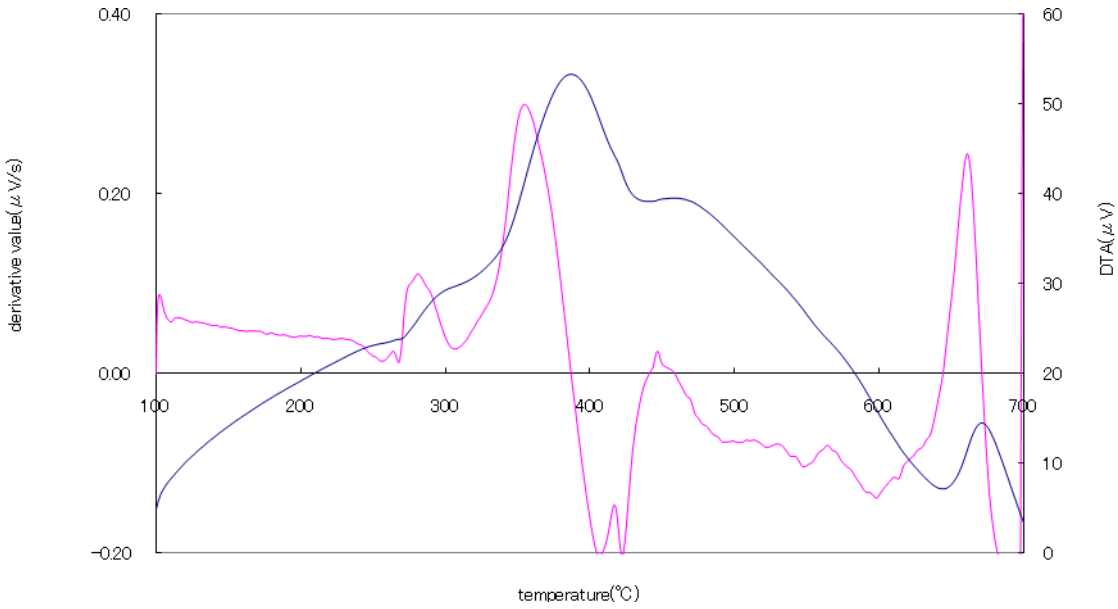

Figure 3.12 DTA curve and derivative curve at a heating rate of 15 °C /min.

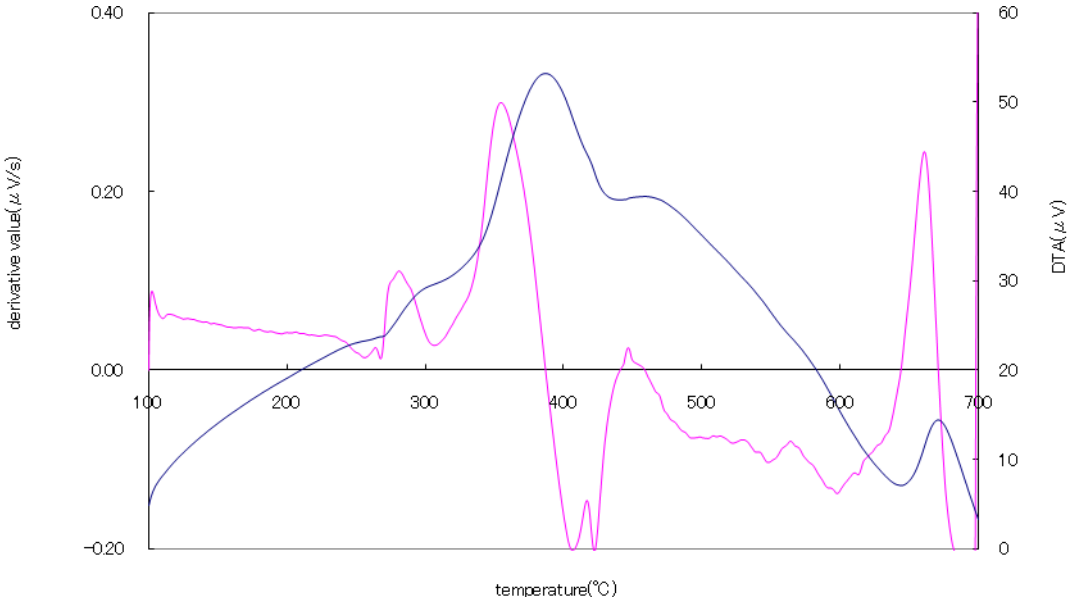

Figure 3.13 DTA curve and derivative curve at a heating rate of 30 °C /min.

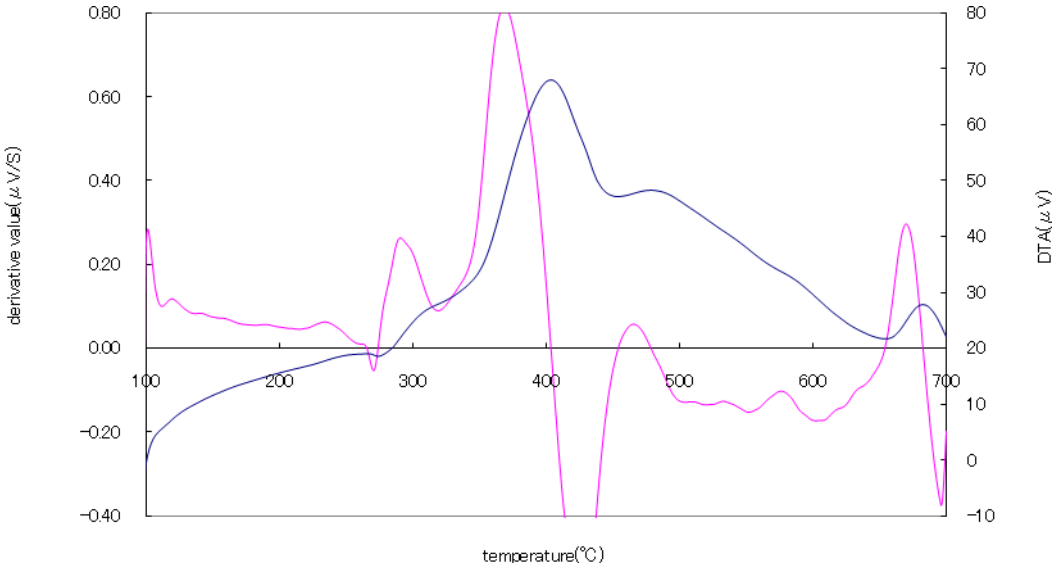

Figure 3.14 DTA curve and derivative curve at a heating rate of 50 °C /min.

Table 3.1 Decomposition temperature and crystallization temperature.

Heating rate Q (°C /min)	Decomposition temperature (°C)	Crystallization temperature (°C)
5	345.6	635.6
10	357.0	650.8
15	368.2	656.9
30	387.1	670.5
50	402.9	680.0

The decomposition temperature and crystallization temperature of the BST dry gel at various heating rates are shown in table 3.1.

The effective Arrhenius activation energy (Ea) for crystallization of perovskite phase was determined by Kissinger equation. The method is based on the dependence of the crystallization peak temperature (T_M) on the DTA heating rate (Q) as follows [10]:

$$\text{Ln } C + \text{Ln } V_0 - Ea/RT_M - \text{Ln } Ea = \text{Ln } (Q/RT_M^2) \quad (3.1)$$

$$C = n[-\text{Ln } (1 - x)]^{(n-1)/n} \quad (3.2)$$

where T_M is the temperature for the maximum rate of phase conversion, i.e. the crystallization peak temperature. Q the constant heating rate in the DTA experiment, Ea the activation energy for crystallization ($Jmol^{-1}$), R the gas constant (8.314 $Jmol^{-1}$), T the absolute temperature. V_0 is a pre-exponential factor for crystallization appearing in the Arrhenius expression of the effective reaction-rate constant, k, whose temperature dependence is generally expressed by the Arrhenius equation:

$$k = V_0 \exp(- Ea/RT) \quad (3.3)$$

According to the transition-state theory, V_0 can be identified with the vibration (parallel to the reaction coordinate) frequency of the atom in the transition state incorporating into a new growing phase (nucleus) and is, therefore, a frequency factor (s^{-1}). The fraction of the transformed phase (x) at time t is expressed by k according to the following well-known

phenomenological Johnson-Mehl-Avrami (JMA) equation [11],

$$x = 1 - \exp[-(kt)^n] \qquad (3.4)$$

Ea can be obtained by plotting the relation between $-1/RT_M$ and Ln (Q/RT_M^2) as figure 3.12 and 3.13.

Values of Avrami exponent n for various crystallization mechanisms is shown in table 3.2.

Table 3.2 Values of Avrami exponent of n for various crystallization mechanisms.

Mechanism Avrami exponent	n
Three-dimensional growth	4
Two-dimensional growth	3
One-dimensional growth	2
Surface nucleation	1

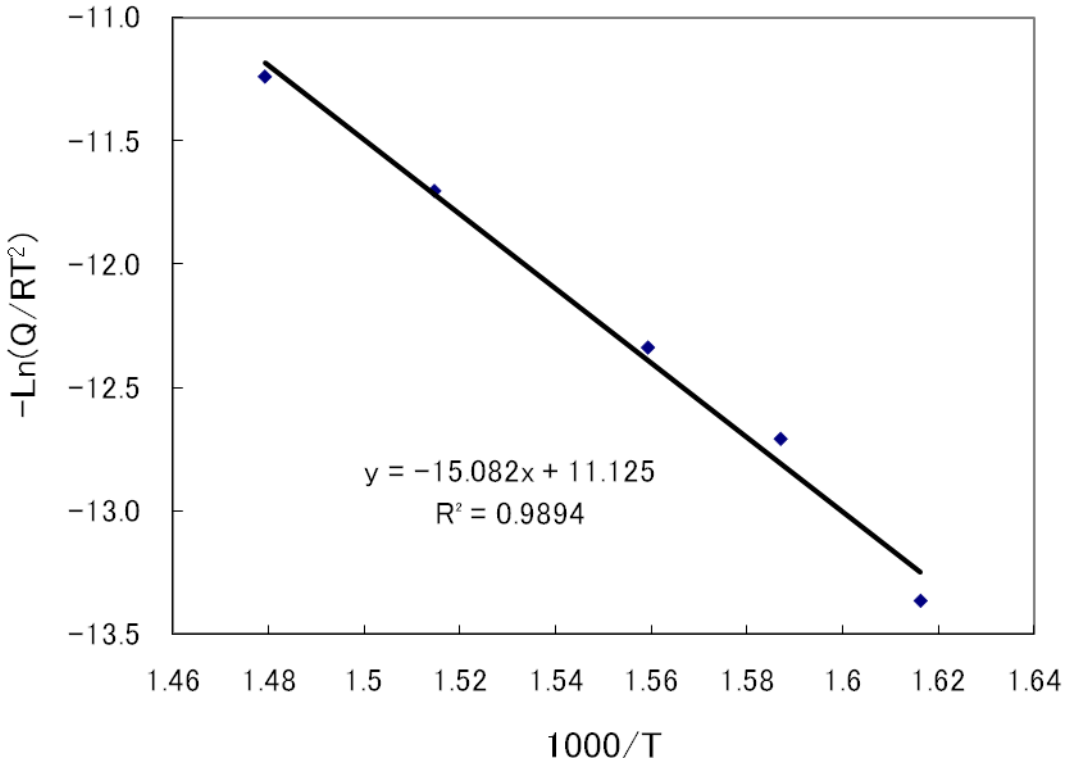

Figure 3.12 Relation between $-1000/RT_M$ and Ln (Q/RT_M^2) of decomposition temperature.

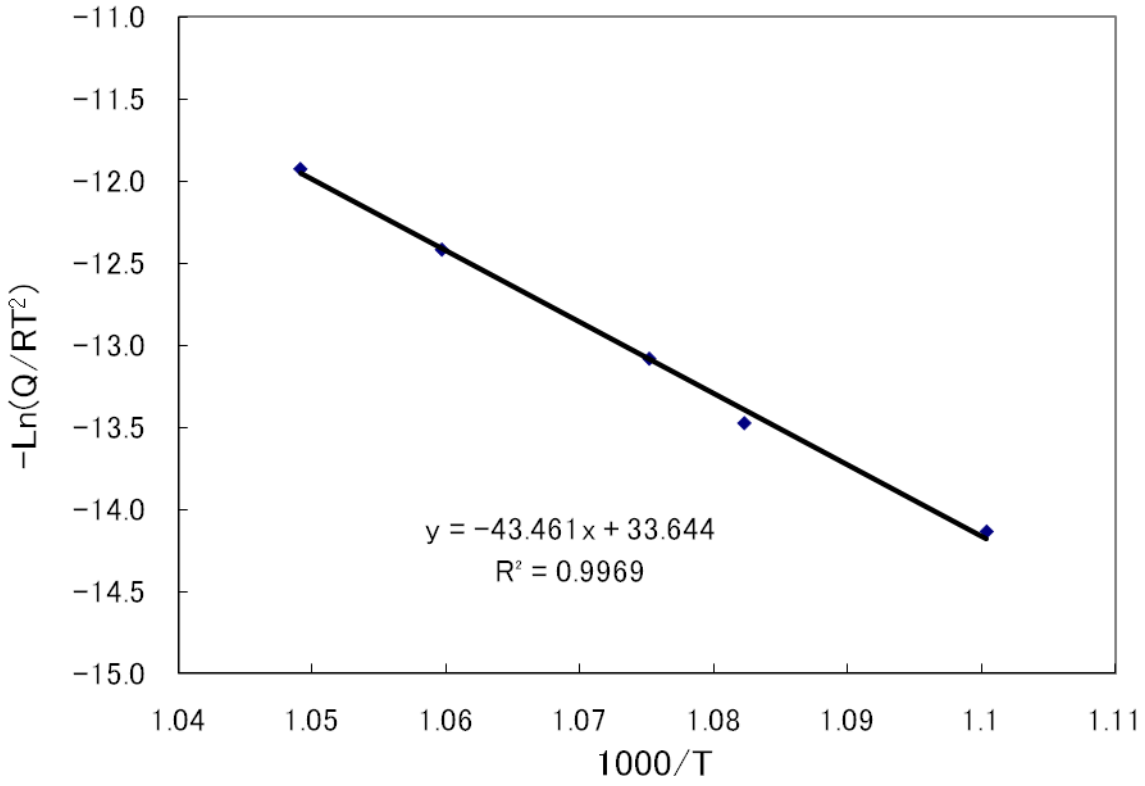

Figure 3.13 Relation between -1000/RT_M and Ln (Q/RT_M^2) of crystallization temperature.

The relation between $-1000/RT_M$ and Ln (Q/RT_M^2) of decomposition temperature and crystallization temperature is shown in figure 3.12 and figure 3.13, respectively. By the least-squares method, the slope of the relation between $-1000/RT_M$ and Ln (Q/RT_M^2) at decomposition temperature was 15.062. Ea is calculated to be 124.76 kJ/mol. By the least-squares method, the slope of the relation between $-1000/RT_M$ and Ln (Q/RT_M^2) at crystallization temperature was 43.46. Ea is calculated to be 361.33 kJ/mol.

From equation (3.2) and (3.3), v_0 is expressed

$$V_0 = (Ea\ Q/RT_M^2)\ \exp(Ea/RT_M) \qquad (3.5)$$

Calculated values of $V_{0\ at}$ different heating rates are shown in table 3.3.

Table 3.3 calculated value of V_0.

Heating rate (°C /min)	V_0 for decomposition (min^{-1})	V_0 for crystallization (min^{-1})
5 °C /min	$6.68E^9$	$1.55E^{20}$
10 °C /min	$8.31E^9$	$1.36E^{20}$
15 °C /min	$7.94E^9$	$1.48E^{20}$
30 °C /min	$7.68E^9$	$1.47E^{20}$
50 °C /min	$7.16E^9$	$1.52E^{20}$

The effective decomposition-rate constant and crystallization-rate constant (k) can be calculated from Eqs. (3.3)

Decomposition-rate constant and crystallization-rate constant at 30 °C/min were calculated. Decomposition-rate constant and crystallization-rate constant are shown in table 3.4 and 3.5, respectively.

Table 3.4 Decomposition-rate constant at 30 °C /min.

Temperature (°C)	350	360	370	380	390
Rate constant (min^{-1})	0.265	0.388	0.561	0.802	1.13

Table 3.5 Crystallization-rate constant at 30 °C /min.

Temperature (°C)	630	640	650	660	670
Rate constant (min^{-1})	0.184	0.311	0.522	0.865	1.41

The result suggests that the growth of perovskite phase is a diffusion-controlled process [9].Considering the case of n=1, the half-life time ($t_{1/2}$) can be directly calculated by substituting x=1/2 into Eq. (3.4), namely,

$$t_{1/2} = (Ln2)/k \qquad (3.6)$$

The half-life time as a function of temperature is shown in table 3.6 and plotted data is shown in figure 3.14 and 3.15.

Table 3.6 Half-life time as a function of temperature.

Decomposition		Crystallization	
Temperature (°C)	Half-life time (min)	Temperature (°C)	Half-life time (min)
260	152.5	540	775.4
280	55.10	560	214.8
300	21.37	580	63.22
320	8.836	600	19.68
340	3.870	620	6.452
360	1.786	640	2.222
380	0.864	660	0.801

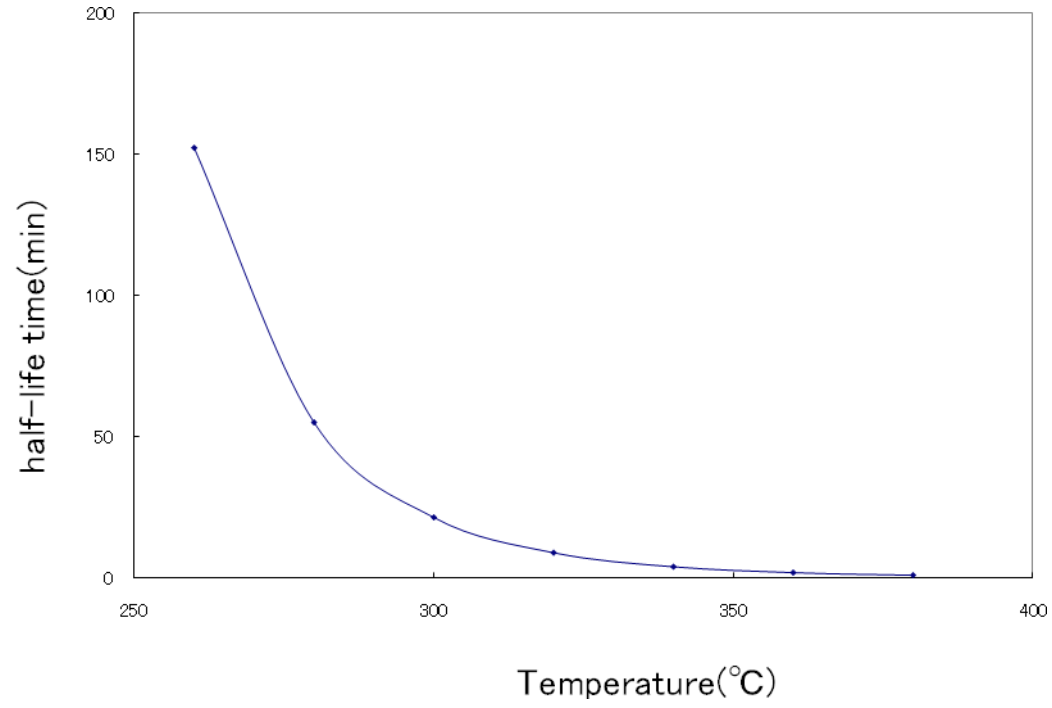

Figure 3.14 Decomposition half-life time as a function of temperature.

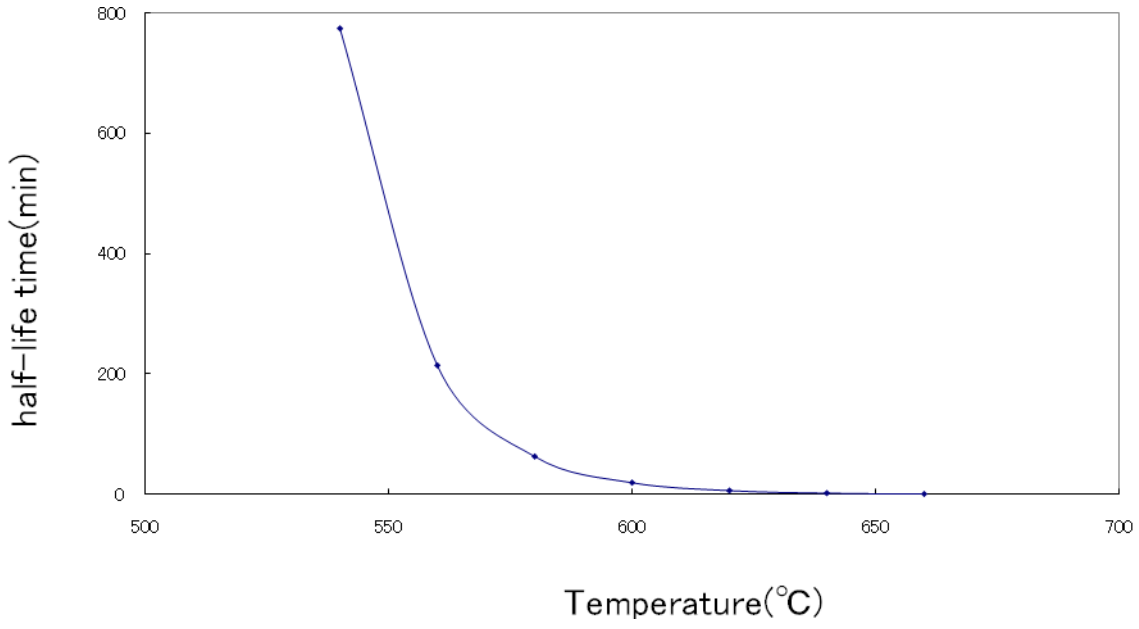

Figure 3.15 Crystallization half-life time as a function of temperature.

The effective Arrhenius activation energy (Ea) for decomposition and crystallization of the CSD solution for BST film are 124.76 kJ/mol and 361.33 kJ/mol respectively. For heating rate at 300 °C/min (normal annealing speed by RTA), decomposition temperature and crystallization temperature are calculated to be 454 °C and 719 °C respectively. The calculated result implies to decide the drying temperature and annealing temperature for CSD solution.

When the half-life time long, intermediate phase appears so it is effective reveal the half-life time to decide the decomposition temperature and crystallization temperature.

3.4 Effect of the heating- rate to the properties of BST thin film by CSD

TG-DTA measurement under changing heating rate enables to express the decomposition and the crystallization reaction of CSD solution by using thermal dynamic method. For heating-rate at 300 °C /min (normal annealing speed by RTA), decomposition temperature and crystallization temperature are calculated to be 454 °C and 719 °C respectively. These calculations imply that heating- rate may effect to the morphology and the dielectric properties of the BST film prepared by CSD method.

Precursor solution was prepared by dissolving $Ba(CH_3COO)_2$, $Sr(CH_3COO)_2$ and $Ti(O\text{-}i\text{-}C_3H_7)_4$ with a molar ratio of 70 : 30 : 100 in a mixed solvent of acetic acid and ethyleneglycol monoethylether (EGMME). Precursor solutions deposited by spin-coating on platinum coated silicon substrates, i.e. 100 nm Pt (111)/20 nm $(Ba,Sr)TiO_3$/1000 nm SiO_2/(100) Si-wafer. These solutions was dispersed on the substrates and then spin coated at 4000 rpm for 30 s. Spin coated films were sintered at 600 °C - 850 °C for 20 min at heat rate of 50 °C/min, 150 °C/min, 300 °C/min, and 500 °C/min. In order to prepare thicker $(Ba,Sr)TiO_3$ films, a multilayer deposition procedure was followed.

Cross section images of the obtained films were taken with a field emission-scanning electron microscope (FE-SEM) and transmission electron microscope (TEM). Crystal characterization was done by X-ray diffraction (XRD). Several Pt dots were evaporated through a mask on the film to form metal–ferroelectric–metal (MFM) capacitors. Small signal ac (100 mV, 1 kHz) capacitance, loss tangent, and ac conductivity were measured with HP 4284A LCR meter. Capacitance–voltage (C-V) measurements were done with HP 4284A LCR meter.

The properties of the BST thin films prepared by different annealing conditions are shown in table 3.7. At 650 °C, the grain size and the dielectric constant of the BST films heating rate by 300 °C /min is relatively higher than the BST films heating rate by 150 °C /min or 50 °C /min.

Surface and cross-sectional FE-SEM images of the film prepared by different heating rates are shown in figure 3.16-3.29. The FE-SEM images indicate that grain size of the BST films differs by heating rate. Comparing the BST films annealed at 650 °C, grain size is 20 nm by 50 °C/min, 35nm by 150 °C/min, 60 nm by 300 °C/min, and 50 nm by 500 °C/min respectively. These differences are induced by the effective crystallization Arrhenius activation energy (Ea) of each the heating rate. The crystallization temperature differs by

the effective crystallization Arrhenius activation energy (Ea).The BST was crystallized at lower temperature at heating rate by 50 °C/min and 150 °C/min compared with the heating rate by 300 °C/min, and 500 °C/min.

When the crystallization occurred at low temperature, free energy of the clusters is low so as not the clusters to derive grain growth. In comparison, the BST thin film of the heating rate by 500 °C/min, crystallization occurred at high temperature so that free energy of the clusters is high and grain growth was accelerated.

The dielectric constant as a function of temperature by different heating speed is shown in figure 3.30. The dielectric constants are inclined to grow as the annealing temperature increased. This incretion is affected by the grain growth. At the same annealing temperature dielectric constants differs as grain sizes are different. Though the annealing temperature is same, the dielectric constant of the BST film changes by the heating rate. The heating rate affects the dielectric constant by changing the grain size of the BST films.

Schematic image of the precursor phase as a function of temperature is shown in figure 3.31. In CSD method, decomposition of the solution occurs then crystallization of the film follows. The epitaxial growth occurs occasionally when the annealing temperature and heating speed is high enough for the BST to grow epitaxially.

Table 3.7 Properties of the BST thin films prepared by different annealing condition.

Heating- rate (°C/min)	Heating temperature(°C)	Capacitance (nF)	Thickness (nm)	Dielectric constant
50	650	1.42	302	247
50	750	2.91	230	230
150	600	1.83	268	247
150	650	2.63	244	370
150	700	4.33	215	534
300	600	3.26	227	425
300	650	4.41	190	481
300	675	4.61	205	544
300	700	5.47	180	566
300	750	5.66	196	618
300	800	6.62	187	673
500	600	2.71	213	331
500	650	3.53	223	451
500	700	4.65	192	503

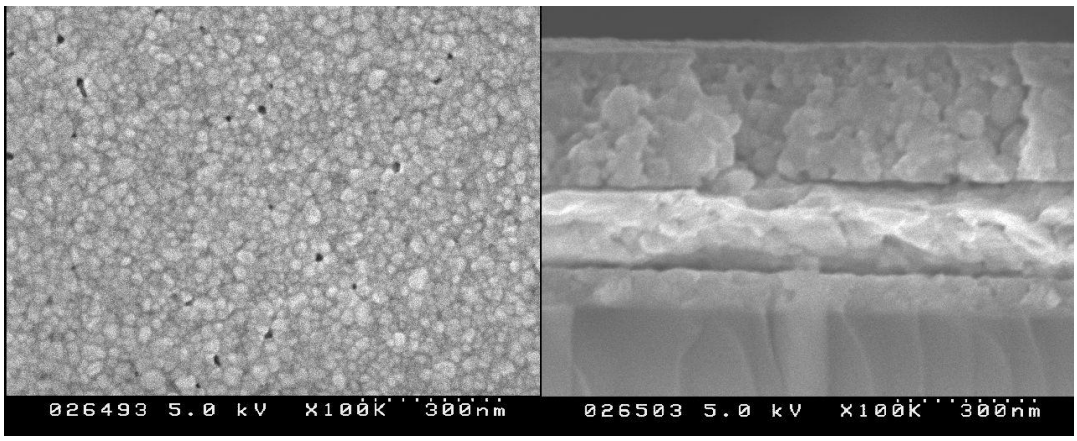

Figure 3.16 Surface and cross-sectional images of the film prepared by heating rate of 50 °C/min at 650 °C.

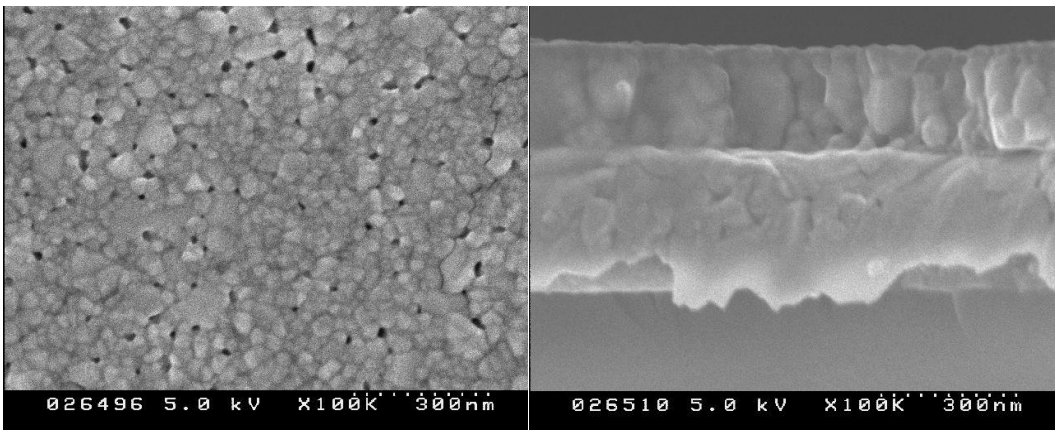

Figure 3.17 Surface and cross-sectional images of the film prepared by heating rate of 50 °C/min at 700 °C.

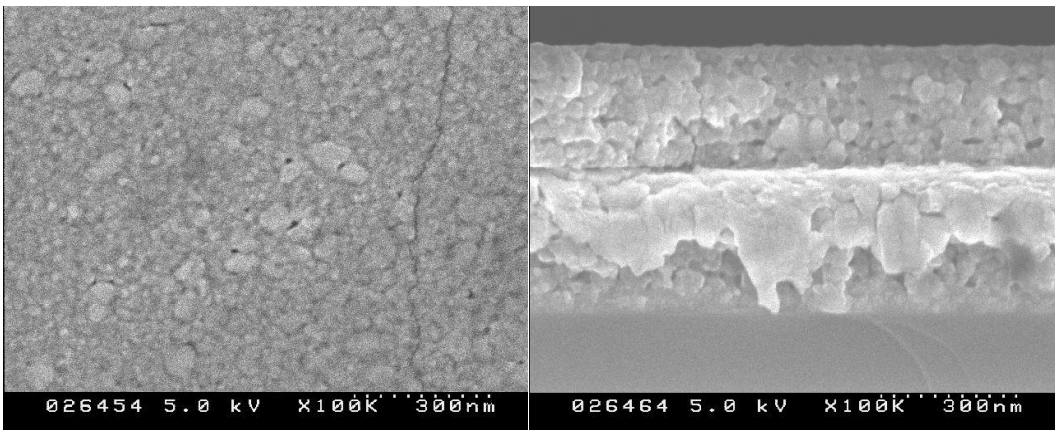

Figure 3.18 Surface and cross-sectional images of the film prepared by heating rate of 150 °C/min at 600 °C.

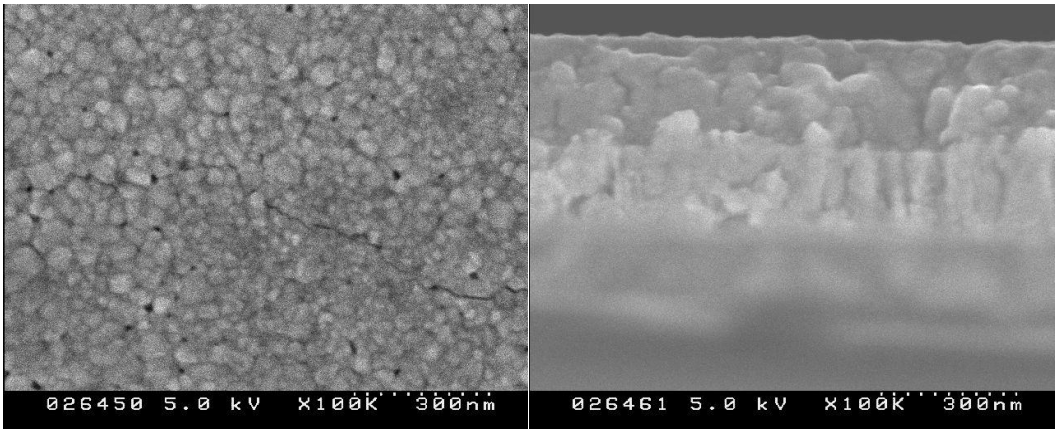

Figure 3.19 Surface and cross-sectional images of the film prepared by heating rate of 150 °C/min at 650 °C.

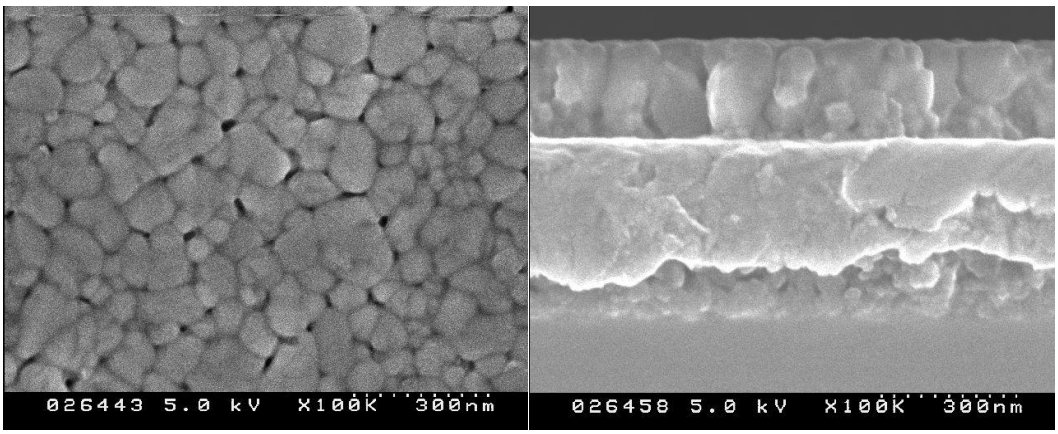

Figure 3.20 Surface and cross-sectional images of the film prepared by heating rate of 150 °C/min at 700 °C.

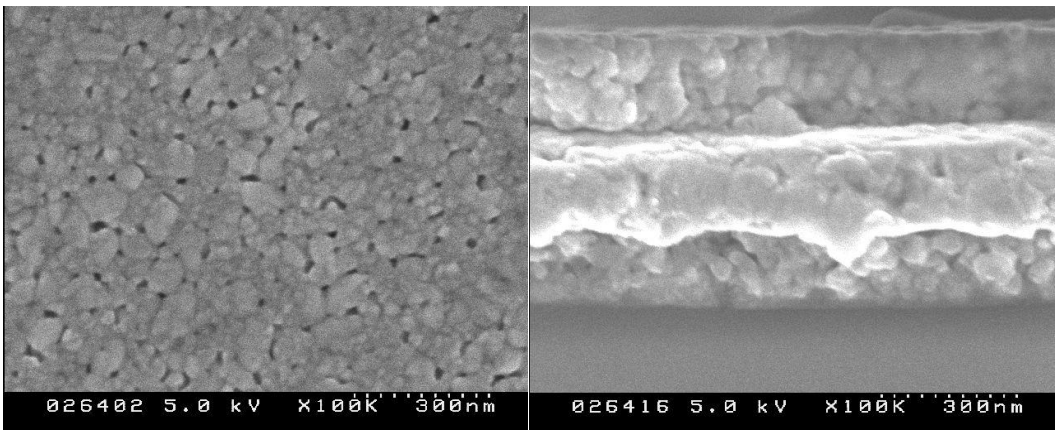

Figure 3.21 Surface and cross-sectional images of the film prepared by heating rate of 300 °C/min at 600 °C.

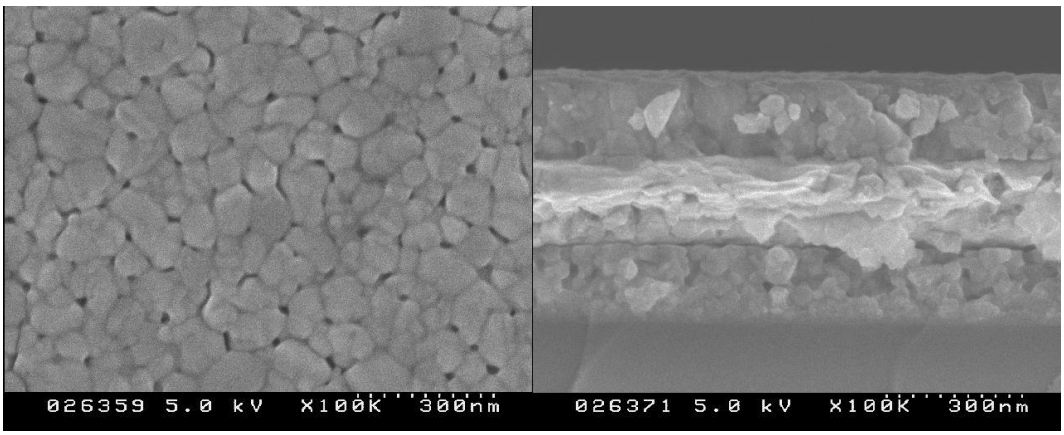

Figure 3.22 Surface and cross-sectional images of the film prepared by heating rate of 300 °C/min at 650 °C.

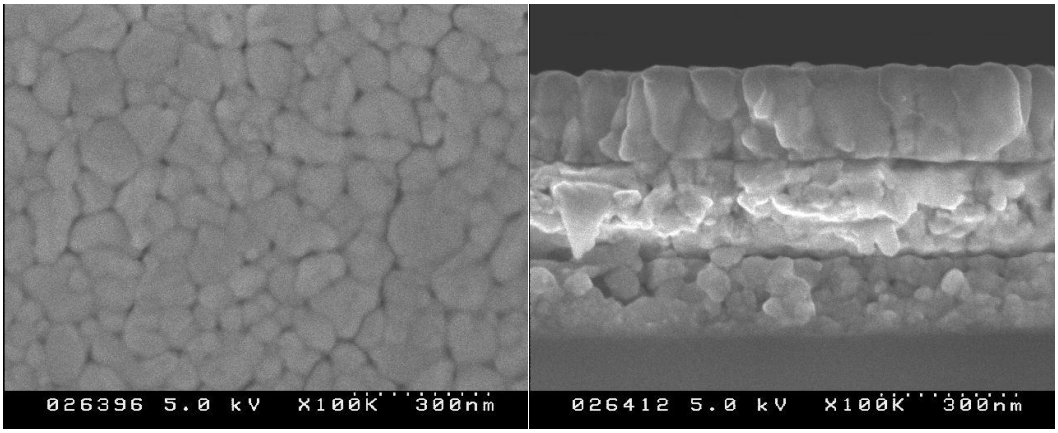

Figure 3.23 Surface and cross-sectional images of the film prepared by heating rate of 300 °C/min at 675 °C.

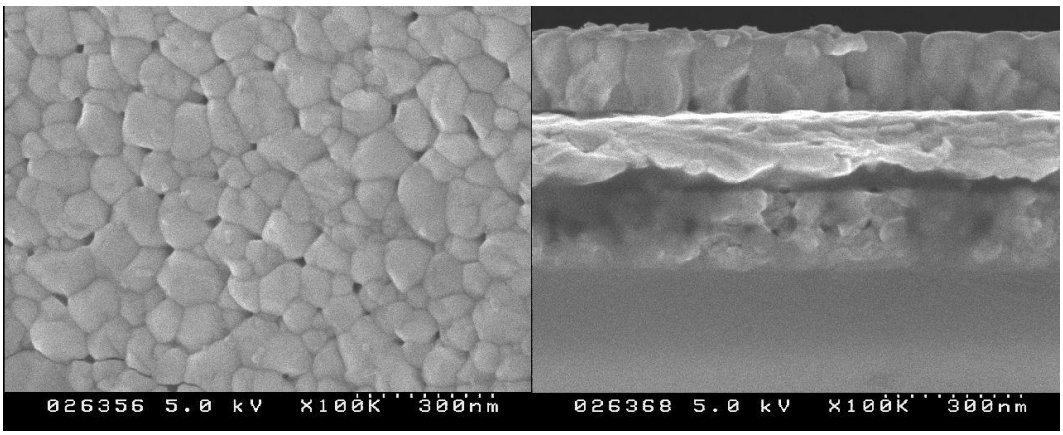

Figure 3.24 Surface and cross-sectional images of the film prepared by heating rate of 300 °C/min at 700 °C.

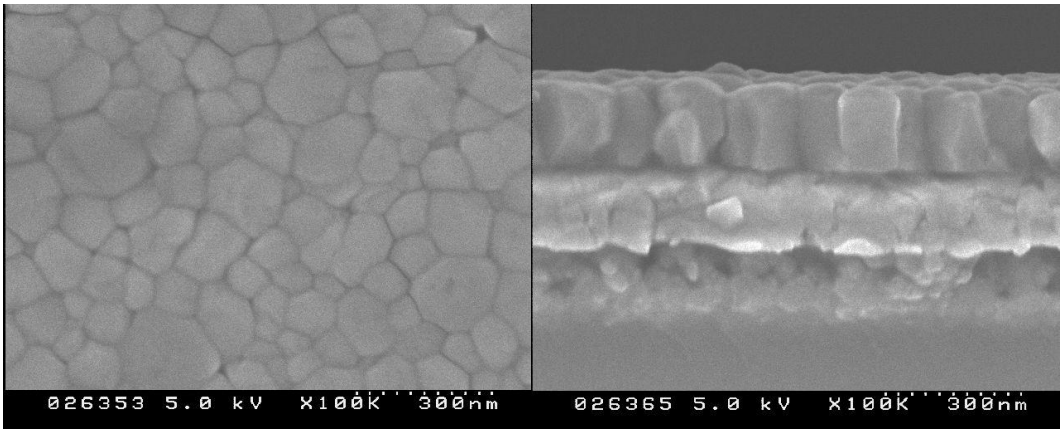

Figure 3.25 Surface and cross-sectional images of the film prepared by heating rate of 300 °C/min at 750 °C.

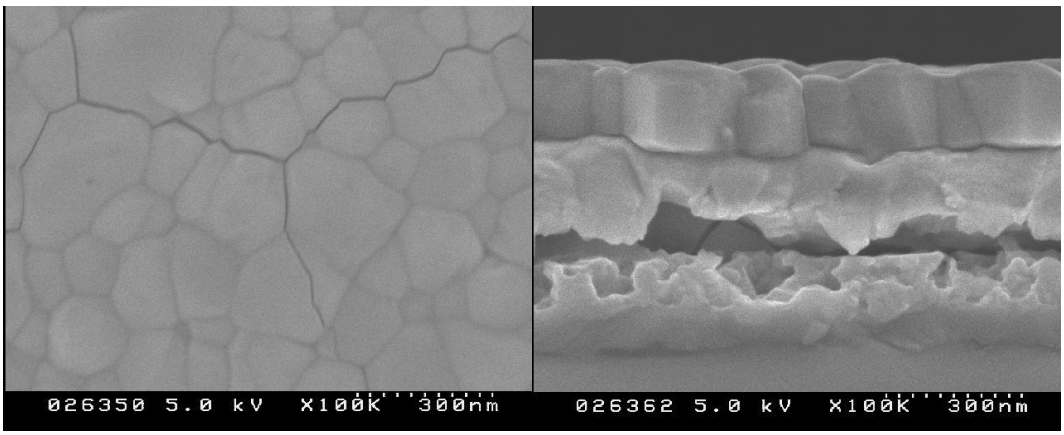

Figure 3.26 Surface and cross-sectional images of the film prepared by heating rate of 300 °C/min at 800 °C.

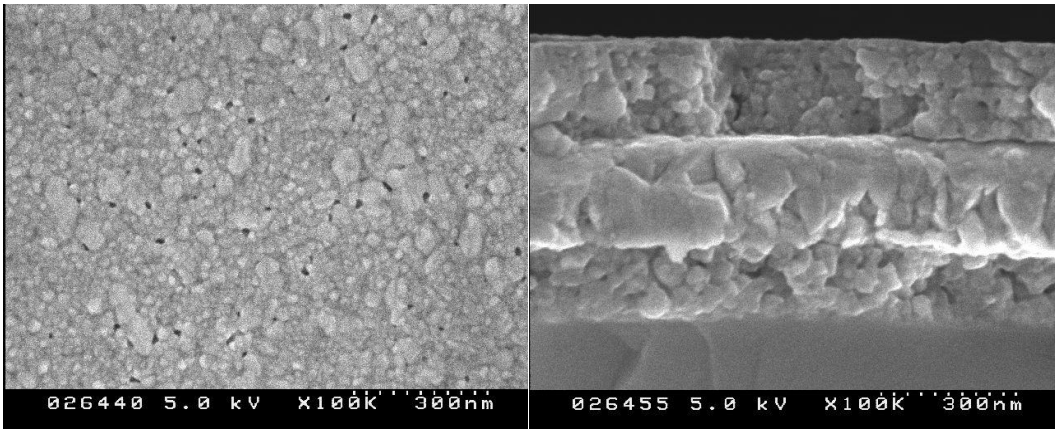

Figure 3.27 Surface and cross-sectional images of the film prepared by heating rate of 500 °C/min at 600 °C.

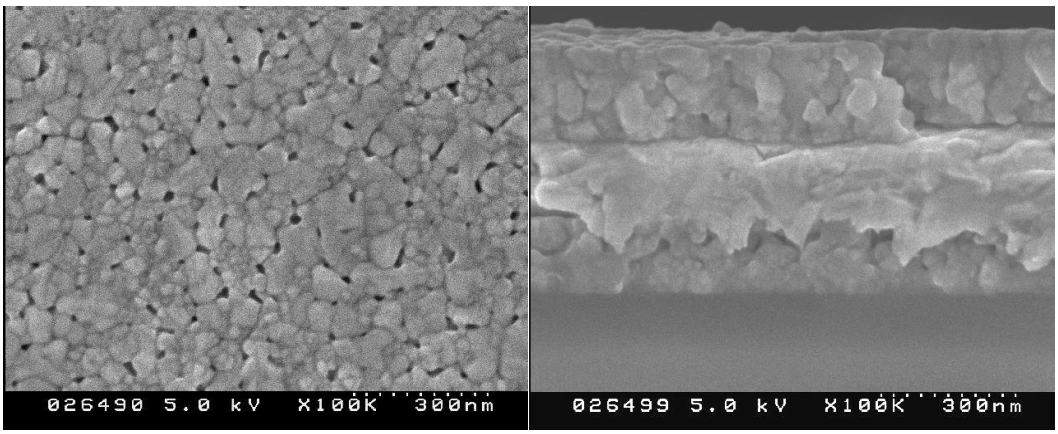

Figure 3.28 Surface and cross-sectional images of the film prepared by heating rate of 500 °C/min at 650 °C.

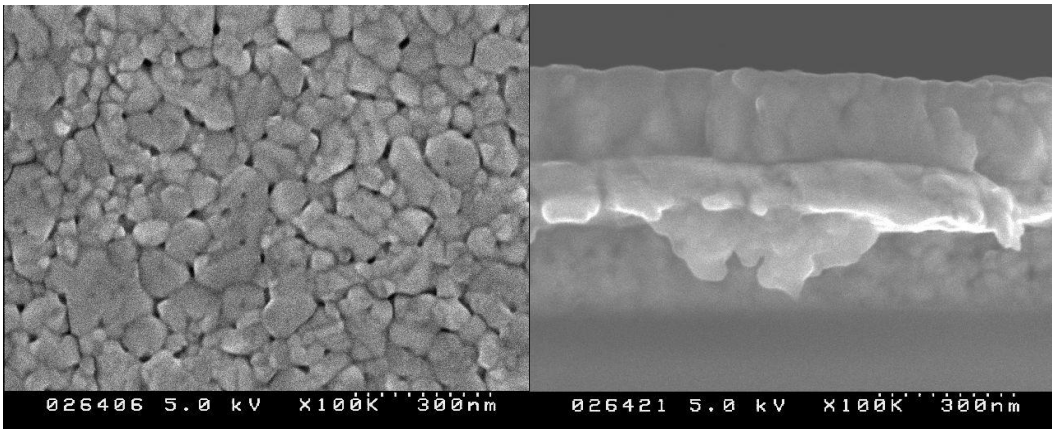

Figure 3.29 Surface and cross-sectional images of the film prepared by heating rate of 500 °C/min at 700 °C.

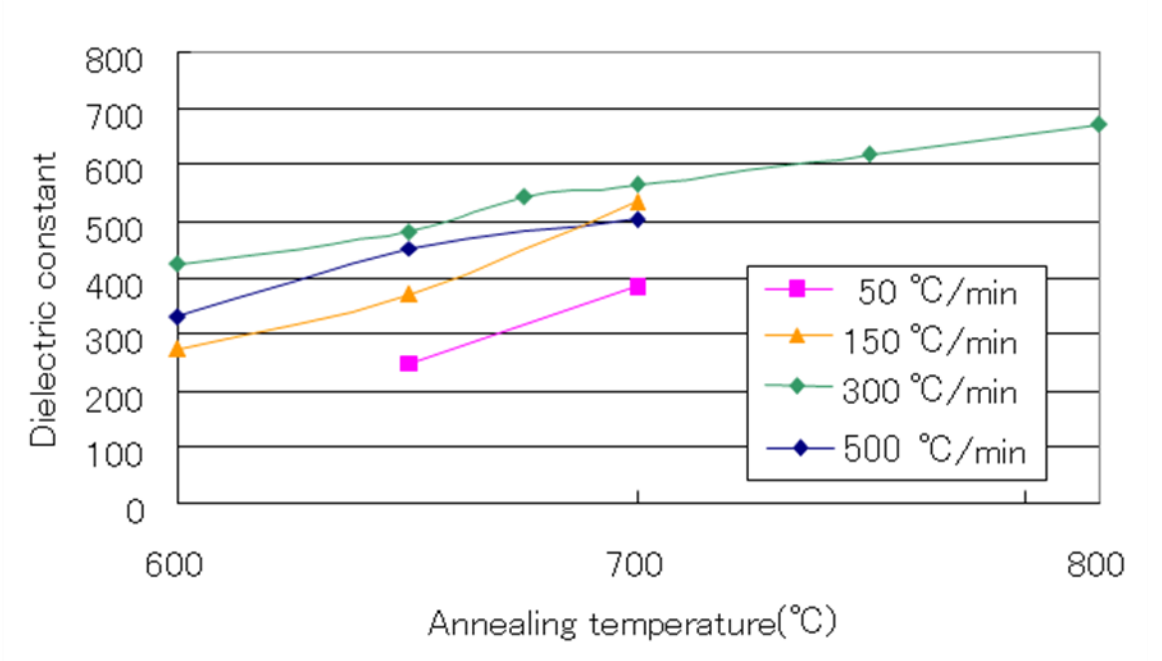

Figure 3.30 Dielectric constant as a function of annealing temperature by different heating speed.

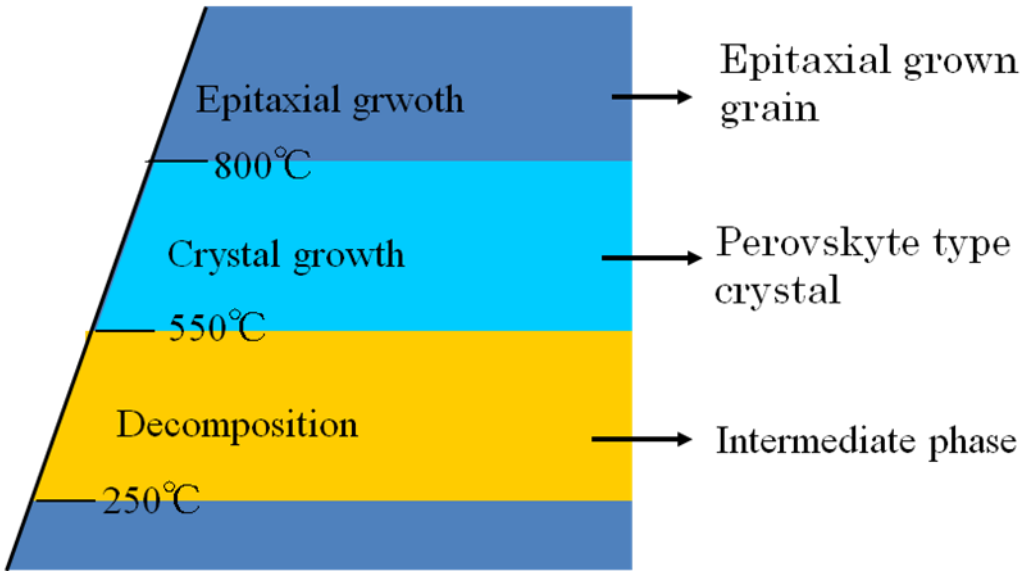

Figure 3.31 Schematic image of the precursor phase as a function of temperature.

3.5 Conclusion

Epitaxially grown $(Ba,Sr)TiO_3$ thin films were prepared on platinum-coated silicon substrate by sol-gel method using a $(Ba,Sr)TiO_3$ sol derived from $Ba(CH_3COO)_2$, $Sr(CH_3COO)_2$ and $Ti(O\text{-}i\text{-}C_3H_7)_4$. The morphology of the films was found to depend on the annealing condition. A columnar structure was obtained for $(Ba,Sr)TiO_3$ thin film by annealing at 800 °C and a columnar grain was found to be single crystal by TEM. The columnar grown film exhibits a preferred (111) orientation that follows the (111) orientation of Pt substrate. Measurement of the C-V in MFM was configured in order to demonstrate the ferroelectric properties. Obtained butterfly loops indicate ferroelectricity in the film. Morphology of BST films was controlling by controlling annealing condition by using CSD method. The prepared BST films showed the ferroelectric polarization reversal that indicates ferroelectricity in the film. Columnar grain growth occurs when annealing condition is above decomposition-temperature and crystallise-temperature. The columnar grown film exhibits a preferred (111) orientation that follows the (111) orientation of Pt substrate. A single columnar grain in BST film is consisted of a single crystal. Dielectric constant of the film differs by the morphology of the film. Columnar grains induce a higher dielectric constant.

TG-DTA measurement under changing heating rate enables to express the decomposition and the crystallization reaction of CSD solution by using thermal dynamic method. The effective Arrhenius activation energy (Ea) for decomposition and crystallization of the CSD solution for BST film are 124.76 kJ/mol and 361.33 kJ/mol respectively. For heating rate at 300 °C/min (common annealing speed by RTA), decomposition temperature and crystallization temperature are calculated to be 454 °C and 719 °C respectively. The calculated result implies to decide the suitable drying temperature and annealing temperature for CSD solution. Appling thermal dynamic method is effective to control the decomposition and crystallization of the thin film prepared by CSD deposition method.

Though the annealing temperature is same, the dielectric constant of the BST film changes by the heating rate. The heating rate affects the dielectric constant by changing the grain size of the BST films. These affects was explained by thermo dynamic method. Using thermo dynamic method enables to reveal the crystallization temperature and to obtain high quality BST film. Appling thermal dynamic method is not effective only to control the

decomposition and crystallization of the thin film but also to control the grain growth and the dielectric constant of the films.

The epitaxial growth occurs occasionally when the annealing temperature and heating speed is high enough for the BST to grow epitaxially.

3.6 References

[1] L.M. Sheppard, Ceram. Bull., **71** (1992) 85.

[2] P.Bhattachary, T. Komeda, D. park, Y. Nishida, Jpn. J. Appl. Phys., **32** (1993) 4103.

[3] P. Kirlin, S. Bilodeau, P. van Buskik, Integrted Ferroelectrics, **7** (1995) 307.

[4] S.-G. Yoon, J. Lee, A. Safari, Integrted Ferroelectrics, **7** (1995) 329.

[5] D. M. Tahan, A. Safari, L.C. Klein, J. Am. Ceram. Soc., **79** (1996) 1593.

[6] H. Kumazawa, K. Masuda Thin solid films, **353** (1999) 144.

[7] S. Hoffmann, R. Waser J. Euro. Ceram. Soc., **19** (1999) 1339.

[8] Dinghua Bao, Zhihong Wang, Wei Ren, Liangying Zhang, and Xi Yao, Ceramics International, **25** (1999) 261.

[9] S.I. Jang, B.C. Choi, H.M. Jang, J. Mater. Res., **12** (1997) 1327.

[10] H.E. Kissinger, Anal. Chem., **29** (1957) 1702.

[11] V. Znidarsic, and P.O. Kolar, J. Mater. Sci., **26** (1991) 2490.

Chapter 4

(100) three-axis-oriented thin film prepared by CSD

4.1 Introduction

Barium titanate and/or barium strontium titanate thin films have been increasingly desired as ferroelectric materials for fabricating ferroelectric memory devices, multilayer capacitor, optical modulator, etc.[1,2] BST paraelectric thin films are attractive dielectrics for use in decoupling capacitors and for use in high-frequency voltage-tunable microwave circuits such as voltage-controlled oscillators (VCOs), tunable filters and phase shifters.[3] The BT(100)/ST(100), SZ(100)/ST(100), and BT(100)/BZ(100) superlattices were fabricated by molecular beam epitaxy (MBE) method to investigate the origin of the unique dielectric properties of the perovskite-type artificial superlattice by Tsurumi et.al.[4] The thin films with controlled orientation and morphology can be used for fabricating small, compact, and low power devices. Epitaxial grown BT and BST thin films have been prepared by various vapor deposition techniques such as RF sputtering,[5,6] pulsed laser deposition,[7,8] metal-organic chemical vapor deposition.[9,10]

In contrast, chemical Solution deposition (CSD) of $BaTiO_3$ or $SrTiO_3$ at temperatures of about 600 - 800 °C typically results in polycrystalline, granular film due to the trend toward homogenous nucleation in the pyrolyzed precursor.[11, 12] CSD method utilized for the synthesis of various perovskite-type thin films, possesses definite advantages for the formation of such films with typical thickness from 100 nm to 400 nm, e.g., good compositional homogeneity, stoichiometry control, high purity, intermediate processing temperatures, and can be applied to large size wafers (typically from 4 to 8-inch). In addition, CSD processing requires inexpensive and standard laboratory equipment for the formation of such thin films.[13]

In this chapter, a controlling the orientation and the morphology of the barium strontium titanate thin film prepared by CSD method is descried.

4.2 (100) three-axis-oriented $(Ba_{0.7}Sr_{0.3})TiO_3$ thin film prepared by CSD

A Pt(111)/MgO(100) and Pt(100)/MgO(100) substrates were used for fabricating a BST thin film by the CSD method. The Pt(111) film was grown on the MgO (100) wafer at 200 °C by dc sputtering. The Pt(100) films was epitaxially grown on the MgO (100) wafer at 600 °C by dc sputtering.

The substrates were annealed at 750 °C for 20 min at a heating rate of 300 °C/min by rapid thermal annealing (RTA) to obtain the clean surface. A chemical solution was prepared by dissolving $Ba(CH_3COO)_2$, $Sr(CH_3COO)_2$, and $Ti(O\text{-}i\text{-}C_3H_7)_4$ with a molar ratio of 70 : 30 : 100 in a mixed solvent of acetic acid and ethyleneglycol monoethylether. The concentration of the solution was 0.3 M.

The chemical solution was deposited by dispersing it on the substrates, following which spin coating was performed at 4000 rpm for 30 s. After spin coating, the film was dried on a hot plate at 150 °C for 3 min. The dried and coated films were annealed at 650 °C or 800 °C for 20 min at a heating rate of 300 °C/min by RTA. In order to prepare a thicker film, the deposition procedure was repeated 6 times. Pt dots with a diameter of 0.5 mm were sputtered by placing a mask on the film to form metal–dielectric–metal (MDM) capacitors.

Cross-sectional images of the obtained films and the selected area electron diffraction (SAED) patterns were obtained by using a transmission electron microscope (TEM) (Model EM-002B, TOPCON, Tokyo, Japan). Crystal characterization was performed by X-ray diffraction (XRD) (Model RINT-KI, Rigaku, Tokyo, Japan). The orientation of the film along the axis parallel to that of the substrate was characterized by an X-ray pole figure measurement (Model X'pert, Philips, Eindhoven, The Netherlands). The cross-sectional images of the films were taken by a field emission-scanning electron microscope (FE-SEM) (Model S-5000, Hitachi, Tokyo, Japan). Small signal ac (100 mV, 1 kHz) capacitance, loss tangent, and capacitance–voltage (C-V) were measured using an LCR meter (HP 4284A, Hewlett-Packard, California, USA).

Cross-sectional images of the films showed that the film morphology depends on the condition used in the CSD method.

Figure 4.1(a) shows a cross-sectional SEM image of the BST thin film on Pt(111)/MgO(100) substrate annealed at 650 °C. The BST thin film comprised 30 nm average-sized grains. The grains were randomly nucleated and crystallized during

annealing.

Figure 4.1(b) shows the cross sectional SEM image of the film annealed at 800 °C. The BST film is composed of columnar grains.

Figure 4.1(c) shows a cross-sectional SEM image of the BST thin film on Pt(100)/MgO(100) substrate annealed at 650 °C. The BST thin film comprised 40 nm average-sized grains. The grains were randomly nucleated and crystallized during annealing.

Figure 4.1(d) shows the cross-sectional SEM image of the BST thin film on Pt(100)/MgO(100) substrate annealed at 800 °C. This BST thin film indicated no evidence of grain boundaries. Crystal structure of the substrate plays an important roll to decide the crystal structure of the deposited layer.

Annealing at 800 °C gives the high ion mobilities. This enabled the formation of a high density layer and giant grain growth. In comparison, BST annealed at 650 °C gives the low ion mobilities. This led to the grains being randomly nucleated, and the grain growth ceased at 30 nm. These SEM images indicated that the morphology of the films depended on the annealing conditions as described in ref. 16. Figure 4.2 shows XRD pattern of BST thin film deposited on Pt(111)/MgO(100) substrate and Pt(100)/MgO(100), respectively.

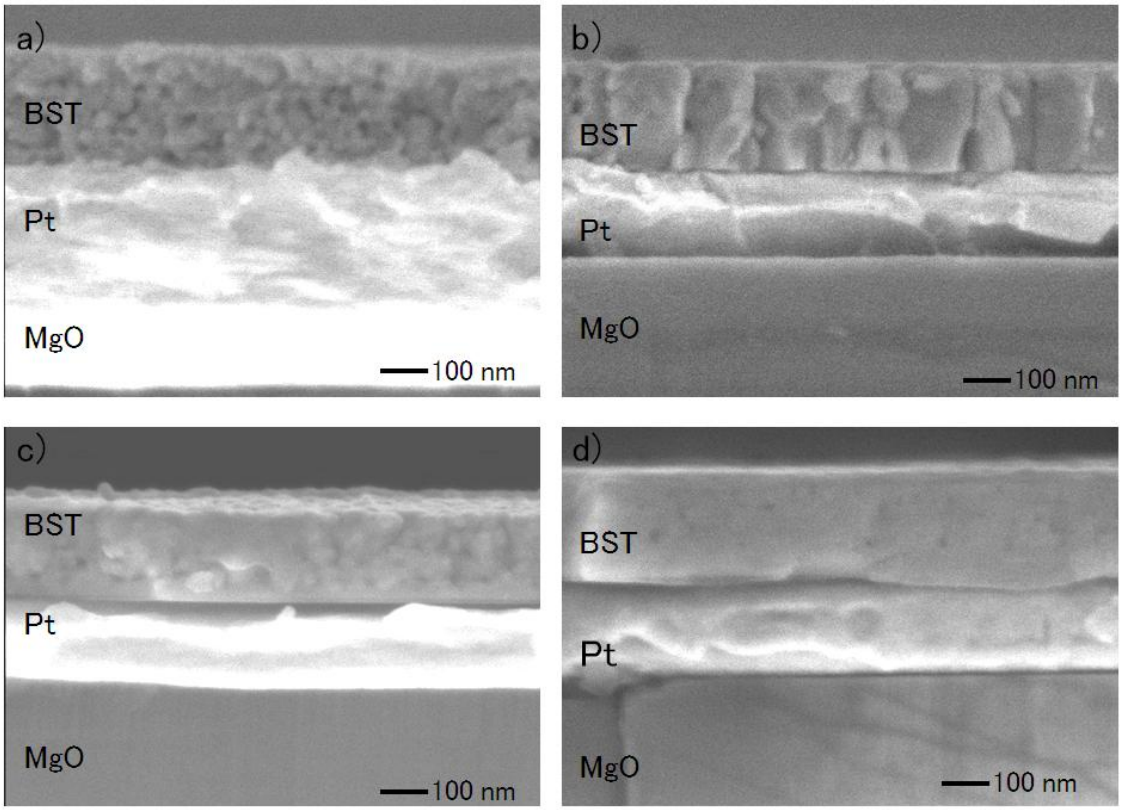

Figure 4.1 (a) Cross-sectional SEM image of the BST thin film on Pt(111)/MgO(100) substrate annealed at 650 °C. (b) Cross-sectional SEM image of the BST thin film on Pt(111)/MgO(100) substrate annealed at 800 °C. (c) Cross-sectional SEM image of the BST thin film on Pt(100)/MgO(100) substrate annealed at 650 °C. (d) Cross-sectional SEM image of the BST thin film on Pt(100)/MgO(100) substrate annealed at 800 °C.

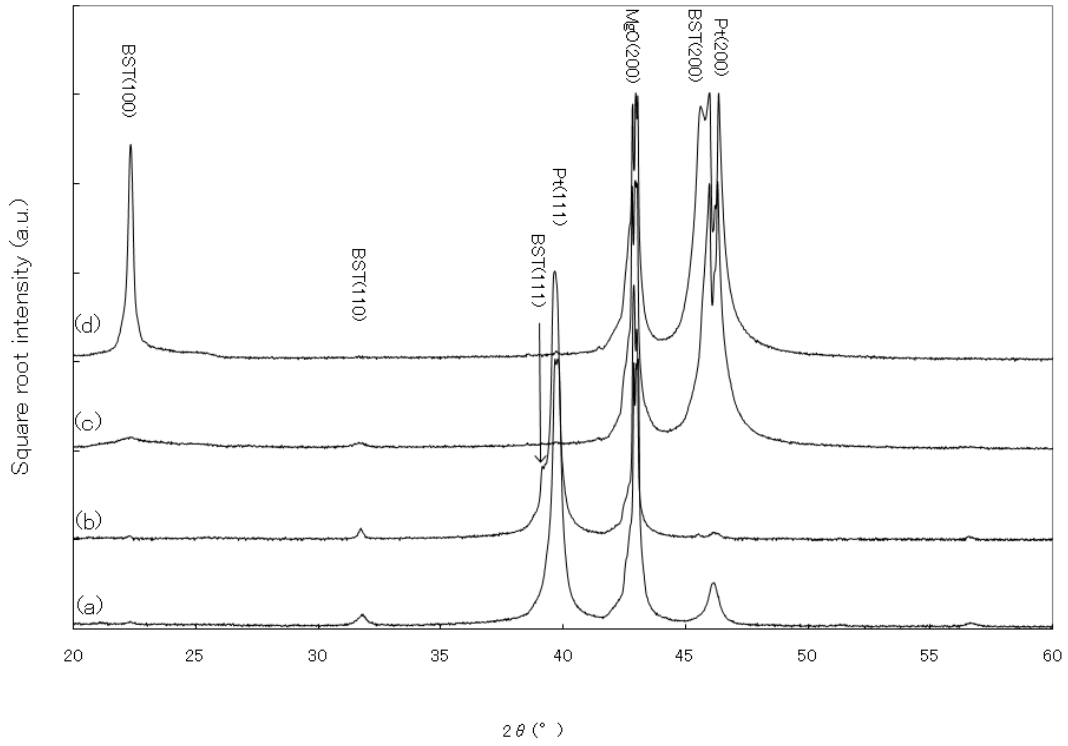

Figure 4.2 (a) XRD pattern of the BST thin film on Pt(111)/MgO(100) substrate annealed at 650 °C. (b) XRD pattern of the BST thin film on Pt(111)/MgO(100) substrate annealed at 800 °C. (c) XRD pattern of the BST thin film on Pt(100)/MgO(100) substrate annealed at 650 °C. (d) XRD pattern of the BST thin film on Pt(100)/MgO(100) substrate annealed at 800 °C.

Figure 4.2(a) and figure 4.2(c) XRD pattern of BST thin film annealed at 650 °C shows typical poly-crystal perovskite diffraction spectra. Figure 2(b) and figure 2(d) show XRD pattern of BST thin film annealed at 800 °C on Pt(111)/MgO(100) substrate and Pt(100)/MgO(100), respectively.

In figure 2(b), the shoulder and the peak appear at 39 ° and 39.5 ° respectively. The shoulder at 39 ° indicates strong orientation of BST(111) and the peak at 39.5 ° indicates strong orientation of Pt(111) .

XRD pattern of BST thin film annealed at 800 °C on Pt(111)/MgO(100) shows that the columnar grains induce a higher degree of oriented growth. The columnar grown film exhibits a preferred (111) orientation that follows the (111) orientation of Pt substrate. This columnar grown is similar to the BST growth on Pt(111)/Si substrate.[17]

Figure 4.2(c) shows an XRD pattern of the BST thin film on Pt(100)/MgO(100) substrate annealed at 650 °C. In the XRD pattern of this BST thin film, (100) reflection and (110) reflection were observed. This result indicated that the film annealed at 650 °C was a poly crystal perovskite BST thin film. Figure 2(d) shows XRD pattern of the BST thin film on Pt(100)/MgO(100) substrate annealed at 800 °C. Strong (*h*00) reflections were observed for this BST thin film deposited. This result indicated that the perovskite BST(100) thin film was hetero-epitaxially grown on Pt(100)/MgO(100) substrate. These results indicated that the crystallinity of thin films can be controlled by varying the annealing conditions. The film annealed at 800 °C on Pt(100)/MgO(100) was further studied by X-ray pole figure measurement and TEM to confirm its epitaxial nature.

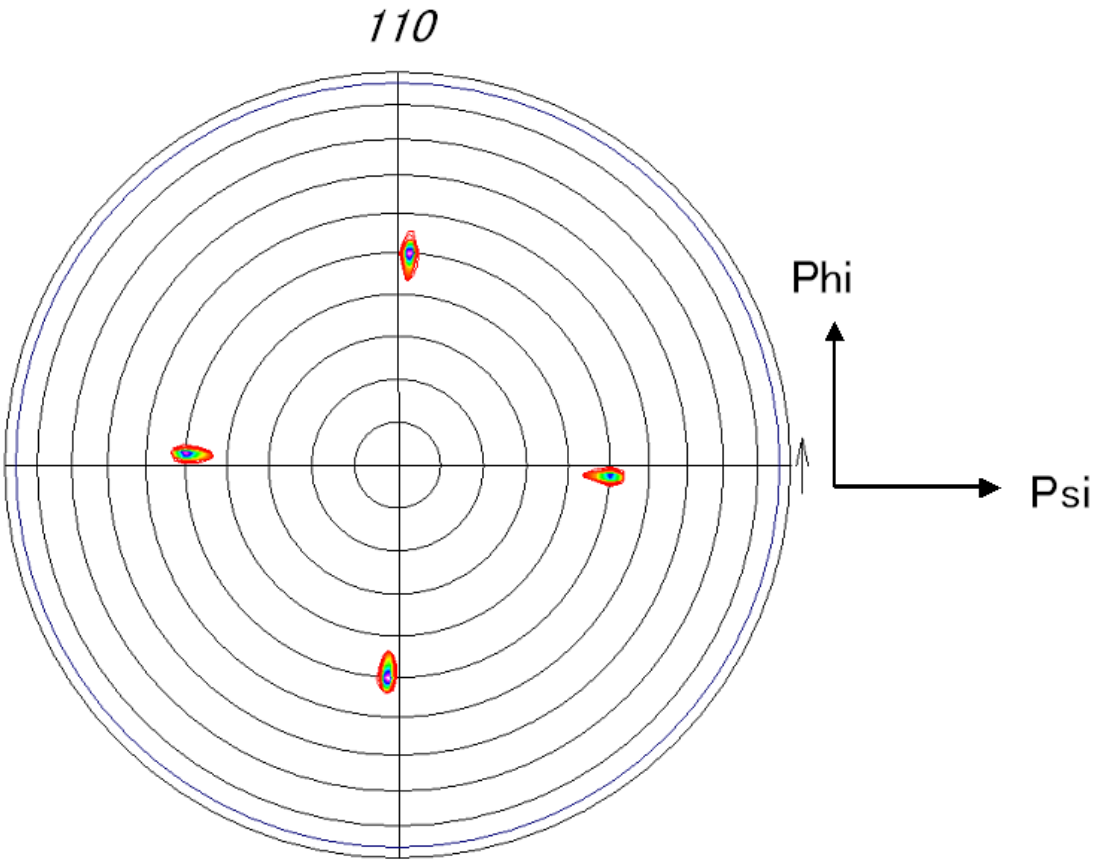

Figure 4.3 X-ray pole figure measured at fixed 2-theta angle corresponding to BST *110* of the BST thin film on Pt(100)/MgO(100) substrate annealed at 800 °C.

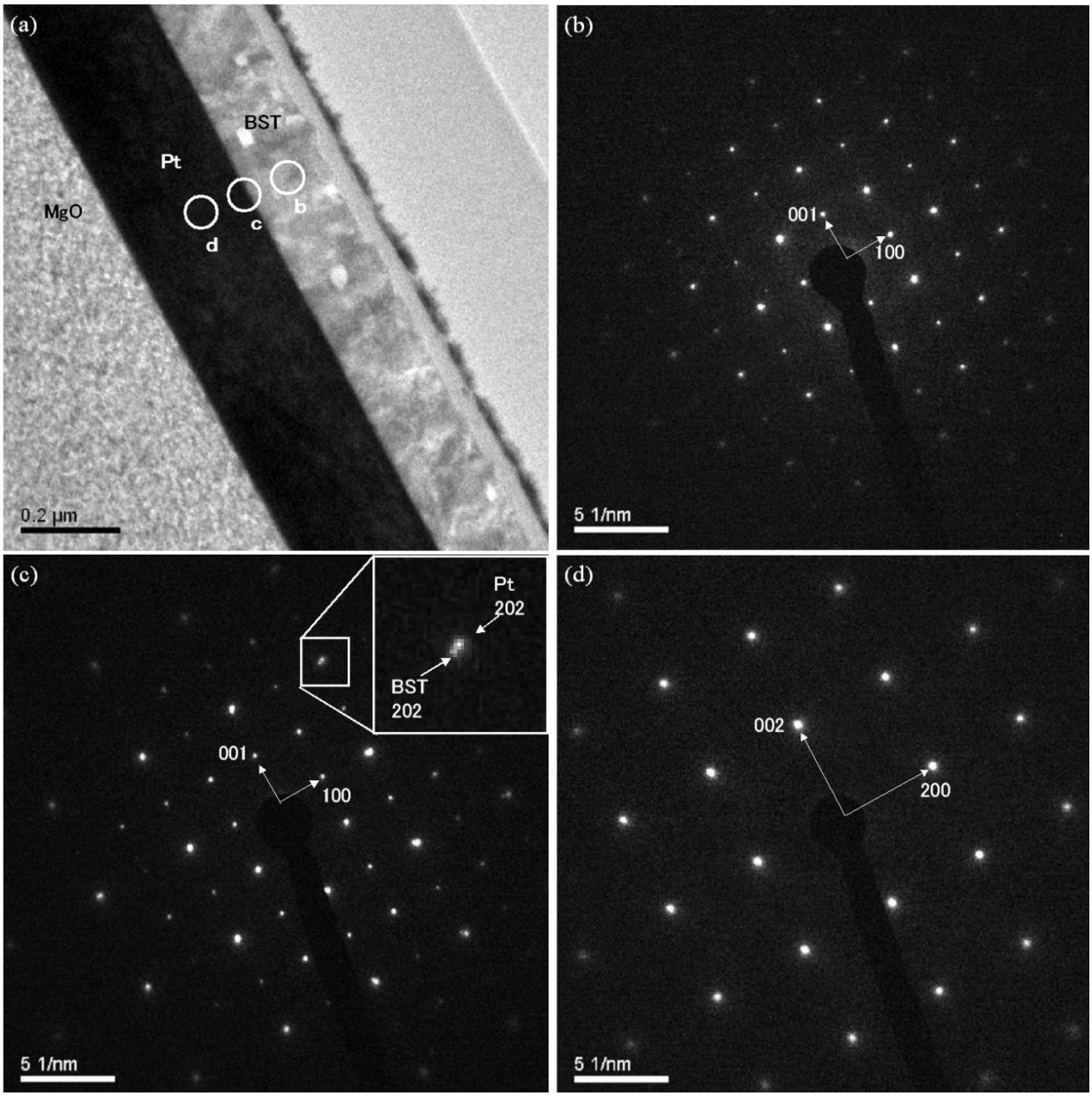

Figure 4.4 (a) Cross-sectional TEM images of the BST thin film on Pt(100)/MgO(100) substrate annealed at 800 °C. (b) The SAED pattern from the BST thin film. (c) The SAED pattern from the boundary of the Pt-sputtered film and the BST thin film. In set shows Pt diffraction spot and BST diffraction spot of (202). (d) SAED pattern from the Pt-sputtered film.

Figure 4.3 shows X-ray pole figure measured at a fixed 2-theta angle corresponding to the 110 reflection of the BST thin film annealed at 800 °C on Pt(100)/MgO(100). Four-fold symmetry and a pole was observed at angle theta of about 45^{o}. This result indicated that the (100) three-axis-oriented BST thin film was deposited on the Pt(100)/MgO(100) substrate. This result agreed with the result of XRD pattern.

Figure 4.4(a) show cross-sectional TEM images of the BST thin film deposited on Pt(100)/MgO(100) substrate. The SAED pattern of the BST thin film, the boundary of the Pt sputtered film and the BST thin film, and the Pt-sputtered film are also shown in figure 4(b), 4(c), and 4(d), respectively. The SAED patterns were obtained when the direction of the electron beam was parallel to the [010] axis of the Pt-sputtered film. Figure 4.4(b) indicates that the Pt(100) film was hetero-epitaxially grown on the MgO(100) wafer. Figure 4.4(c) indicates that spot of Pt and BST superimposed on each other due to the same preferred orientation of (100). Figure 4.4(d) indicates that the orientation of the hetero-epitaxally grown BST thin film was the (100) direction. The BST thin film was highly hetero-epitaxial with respect to the Pt-sputtered film. These results indicated that the (100) three-axis-oriented the BST thin film was deposited on the Pt(100)/MgO(100) substrate. These results agreed with the results of the XRD pattern and X-ray pole figure measurement.

Figure 4.5 shows a cross-sectional bright field TEM image of the boundary of the Pt-sputtered film and the BST thin film annealed at 800 °C on Pt(100)/MgO(100). The BST thin film was highly hetero-epitaxial with respect to the Pt-sputtered film, and was effectively single-crystal-like with no visible grain boundaries. The TEM observation results revealed that the BST thin film annealed at 800 °C exhibited a strong cube-on-cube epitaxy.

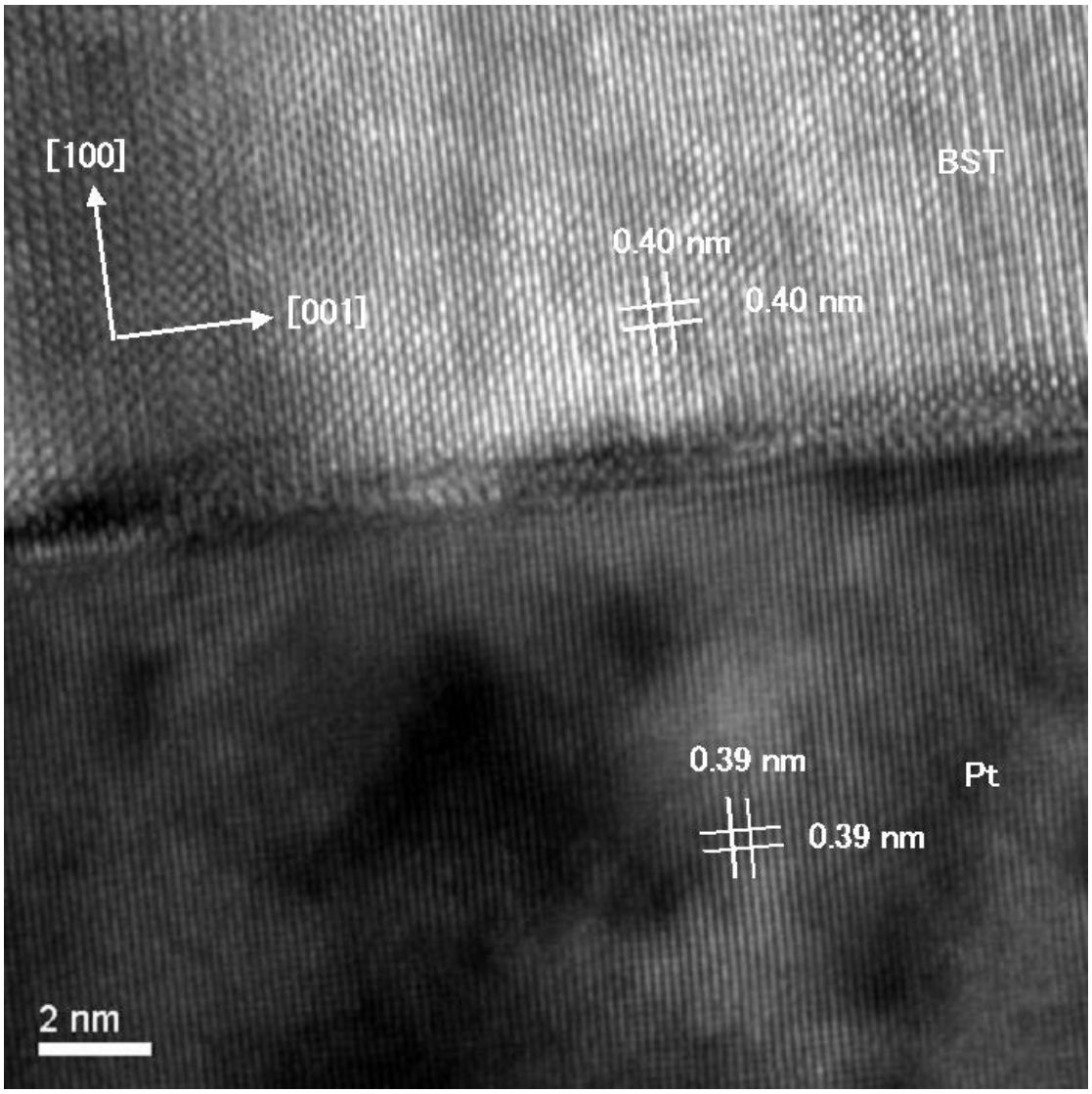

Figure 4.5 Cross-sectional bright field TEM image of the boundary of the Pt-sputtered film and the BST thin film on MgO(100) substrate annealed at 800 °C.

Figure 4.6 shows a C-V plot for the films at a frequency of 1 kHz. The measurement of the C-V plot in the MDM configuration revealed the dielectric properties. At zero bias, the dielectric constant and tan delta of the BST thin film on Pt(111)/MgO(100) substrate annealed at 650 °C were approximately 850 and 0.042, the dielectric constant and tan delta of the BST thin film on Pt(111)/MgO(100) substrate annealed at 800 °C were approximately 2700 and 0.033, the dielectric constant and tan delta of the BST thin film on Pt(100)/MgO(100) substrate annealed at 650 °C were approximately 600 and 0.036, and dielectric constant and tan delta of the BST thin film on Pt(100)/MgO(100) substrate annealed at 800 °C is around 1200 and 0.022, respectively.

C-V curve of the BST thin film on Pt(111)/MgO(100) substrate annealed at 800 °C indicates high dielectric constant and high tunability compared with the other BST thin film. Two maximums were clearly observed in the BST thin film on Pt(100)/MgO(100) substrate annealed at 800 °C. Butterfly-shaped C-V curve is associateable with redistribution of near-electrode charging/discharging processes.[18, 19] The mechanism of this phenomenon had been discussed in ref 20. The dielectric constant of the $(Ba_{0.6}Sr_{0.4})TiO_3$ film epitaxally grown on the Pt(100)/MgO(100) substrate by the CVD method was 1200, as mentioned in ref. 21. This indicated that identical electric properties were observed though the film deposition processes were different. Dielectric constant of the film differs by the morphology of the film. The dielectric constant of the three-axis-oriented BST thin film was twice as high as that of the poly crystal BST thin film. Columnar grains induce a higher dielectric constant and high tunability. The temperature dependence of the dielectric constant in the films on Pt(100)/MgO(100) substrate is shown in figuer 4.7. The dielectric constant was measured at 1 kHz, with 0.1 V at zero-biased from -60 °C to 150 °C. Temperature dependence of the dielectric constant of the film heat treated at 650 °C was stable from -50 °C to 40 °C and decreased continuously with increasing temperature above 40 °C. This change at 40 °C is corresponded to some kind of a phase transition. The dielectric constant of the film heat treated at 800 °C constant decreased continuously from 1367 to 626 with increasing temperature. In spite of, the CSD method being kinetically limited as compared with physical vapor deposition (PVD) method, $(Ba_{0.7}Sr_{0.3})TiO_3$ three-axis-oriented thin films can be obtained by selecting optimum type of substrate and optimum conditions for epitaxial growth by the CSD method.

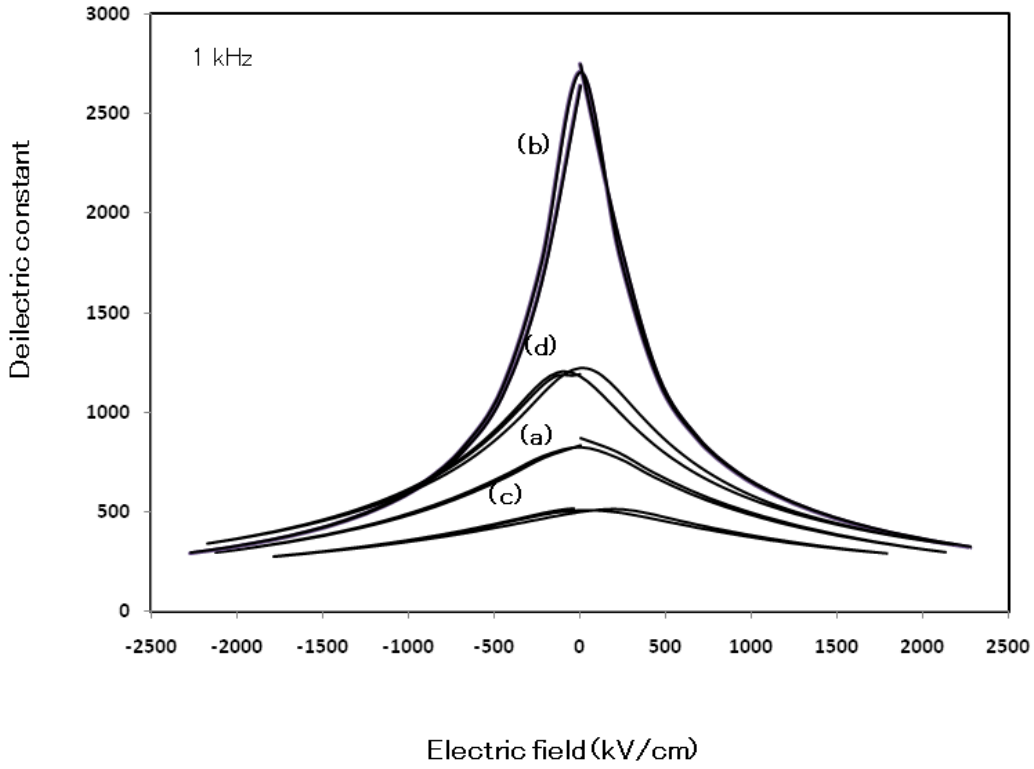

Figure 4.6 C-V plots for the BST thin films. (a) The BST thin film on Pt(111)/MgO(100) substrate annealed at 650 °C. (b)The BST thin film on Pt(111)/MgO(100) substrate annealed at 800 °C. (c) The BST thin film on Pt(100)/MgO(100) substrate annealed at 650 °C. (d)The BST thin film on Pt(100)/MgO(100) substrate annealed at 800 °C.

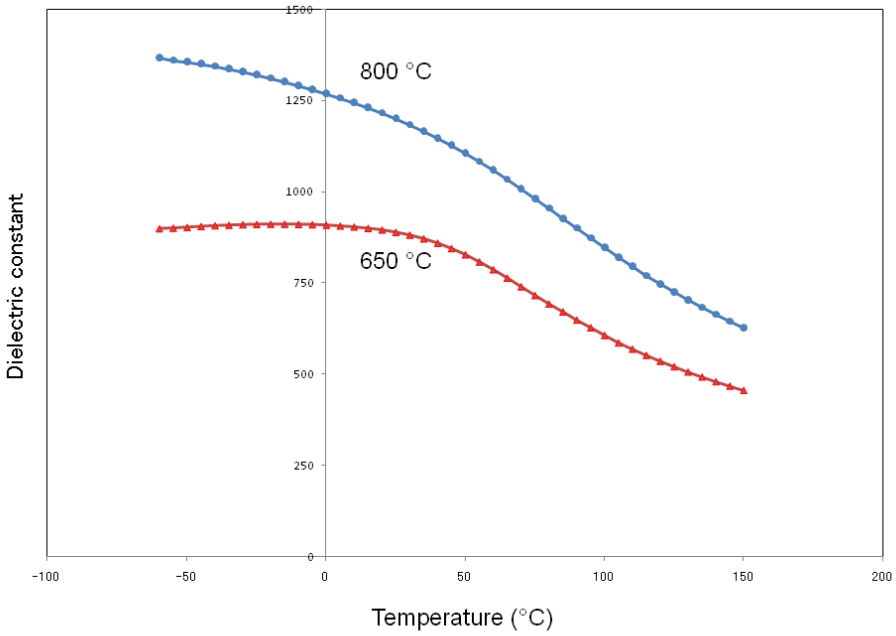

Figure 4.7 Temperature dependence of the dielectric constant in the BST film annealed at 650 °C and 800 °C Pt(100)/MgO(100) substrate

4.3 (100) three-axis-oriented $BaTiO_3$ thin film with $BaZrO_3$ buffer layer

$BaZrO_3$(100)/MgO(100) substrate was used for fabricating a $BaTiO_3$ (BT) thin film by the CSD method. The lattice parameters of MgO, $BaZrO_3$, and $BaTiO_3$ are 0.4211 nm, 0.4192 nm, and 0.4004 nm, respectively.[14, 15]

$BaZrO_3$ was chosen as the bottom layer because the value of its lattice parameter lies between those of the lattice parameters of MgO and $BaTiO_3$. A $BaZrO_3$(100)/MgO(100) substrate was fabricated as follows. The MgO(100) substrate was annealed at 750 °C for 20 min at a heating rate of 300 °C/min by RTA to obtain the clean surface. A chemical solution was prepared by dissolving $Ba(CH_3COO)_2$ and $Zr(O\text{-}i\text{-}C_3H_7)_4$ in a 1:1 molar ratio in mixed solvent of acetic acid and ethyleneglycol monoethylether. The concentration of the solution was 0.3 M.

The chemical solution was deposited on the MgO (100) substrate by dispersion and annealed at 800 °C; coating and annealing were also performed by the same condition as mentioned above. In order to prepare a thicker $BaZrO_3$ thin film, the deposition procedure was repeated 3 times.

A chemical solution of $Ba(CH_3COO)_2$ and $Ti(O\text{-}i\text{-}C_3H_7)_4$ was deposited by dispersing it on the $BaZrO_3$(100)/MgO(100) substrate; The chemical solution was deposited on the MgO (100) substrate by dispersion annealed at 800°C; coating and annealing were also performed by the same condition as mentioned above. In order to prepare a thicker $BaTiO_3$ thin film, the deposition procedure was repeated 3 times.

Cross-sectional images of the obtained films and the selected area electron diffraction (SAED) patterns were obtained by using a transmission electron microscope (TEM) (Model EM-002B, TOPCON, Tokyo, Japan). Crystal characterizations were performed by X-ray diffraction (XRD) (Model RINT-KI, Rigaku, Tokyo, Japan). The orientation of the film along the axis parallel to that of the substrate was characterized by an X-ray pole figure measurement (Model X'pert, Philips, Eindhoven, The Netherlands). The cross-sectional images of the films were taken by a field emission-scanning electron microscope (FE-SEM) (Model S-5000, Hitachi, Tokyo, Japan).

Figure 4.7 shows image of $BaTiO_3/BaZrO_3$/MgO thin film. As seen in figure 4.7, transparent $BaTiO_3$ thin film was obtained. Figure 4.8 shows the UV-VIS transmission spectra of the MgO(100) substrate and the $BaTiO_3/BaZrO_3$ thin film deposited on MgO(100) substrate from 700 nm to 200 nm. For MgO(100) substrate the transmittance

was about 87 % from 250 nm to 700 nm and reaches zero at about 200 nm.

For the $BaZrO_3/BaTiO_3$ thin film deposited on MgO(100) substrate the transmittance was about 70 % from 700 nm to 400 nm and reaches zero at about 280 nm. The absorption band seems to exist from 400 nm to 330 nm. This is a typical absorption band for $BaTiO_3$ as written in ref. (22, 23). The UV-VIS transmission spectra observation indicates that the transparent $BaTiO_3$ thin film is obtained by our method.

Figure 4.9(a) shows the AFM image of the $BaZrO_3$ film deposited on the MgO substrate. The surface roughness (Ra) of the $BaZrO_3$ film was 0.639 nm. Figure 4.9(b) shows the AFM image of the $BaTiO_3$ film deposited on the $BaZrO_3$/MgO substrate. The surface roughness (Ra) of the $BaTiO_3$ film was 1.093 nm.

Figure 4.10 shows the cross-sectional SEM image of the $BaTiO_3/BaZrO_3$ thin film deposited on the MgO(100) substrate annealed at 800 °C. This $BaTiO_3/BaZrO_3$ thin film indicated no evidence of grain boundaries.

Figure 4.11 shows an XRD pattern of the $BaTiO_3/BaZrO_3$/MgO thin film annealed at 800 °C. Strong (*h*00) reflections were observed in this pattern. The perovskite $BaTiO_3$(100)/$BaZrO_3$(100) oriented thin film is deposited on the MgO(100) substrate as the lattice mismatch between MgO and $BaZrO_3$ is sufficiently small for epitaxial growth to occur.

Figure 4.12 shows an X-ray pole figure measured at a fixed 2θ angle corresponding to the *110* reflection of the $BaTiO_3/BaZrO_3$/MgO thin film annealed at 800 °C. Four-fold symmetry and a pole were observed at $\theta = 45°$. This result indicated that a (100) three-axis-oriented $BaTiO_3/BaZrO_3$ thin film was deposited on the MgO(100) substrate. This result agreed with the result of the XRD pattern.

Figure 4.13(a) shows cross-sectional TEM images of the $BaTiO_3/BaZrO_3$ thin film deposited on the MgO(100) substrate. The thickness of the $BaTiO_3/BaZrO_3$ thin film was confirmed to be 150 nm. The $BaTiO_3/BaZrO_3$ thin film indicated no evidence of grain boundaries. The boundaries of each coat are observed in the image, and the thickness of the each coat was confirmed to be 25 nm.

Figure 4.13(b) shows the SAED pattern of the $BaTiO_3/BaZrO_3$ thin film deposited on an MgO(100) substrate. The SAED patterns were obtained when the direction of the electron beam was parallel to the [010] axis of the MgO(100) substrate. The orientation of the epitaxially grown $BaTiO_3/BaZrO_3$ thin film was along the (100) direction. The spots of

$BaZrO_3$ and $BaTiO_3$ overlapped due to the same preferred orientation of (100). These results indicated that a (100) three-axis-oriented $BaTiO_3/BaZrO_3$ thin film was deposited on the MgO(100) substrate. These results agreed with the results of the XRD pattern and X-ray pole figure measurement.

Figure 4.14 shows a cross-sectional bright-field TEM image of the boundary between the $BaZrO_3$ layer and the $BaTiO_3$ layer of the $BaTiO_3/BaZrO_3$ thin film deposited on the MgO(100) substrate. The $BaZrO_3$ layer was highly epitaxial with respect to the MgO(100) substrate, and it was effectively single-crystal-like with no visible grain boundaries. The TEM observation results revealed that the $BaZrO_3$ layer of the $BaTiO_3/BaZrO_3$ thin film deposited on the MgO(100) substrate exhibited a strong cube-on-cube epitaxy. Defects are observed with a regular spacing of 10 nm at the boundary between the $BaZrO_3$ and $BaTiO_3$ layers.

Figure 4.7 Image of $BaTiO_3/BaZrO_3/MgO$ thin film.

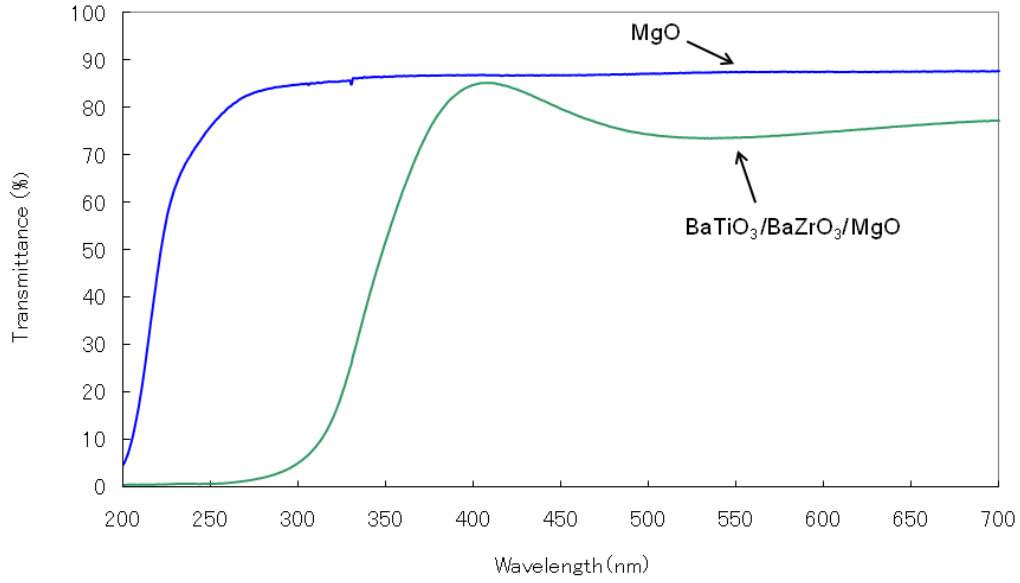

Figure 4.8 UV-VIS transmission spectra of the MgO(100) substrate and the $BaTiO_3/BaZrO_3$ thin film deposited on MgO(100) substrate.

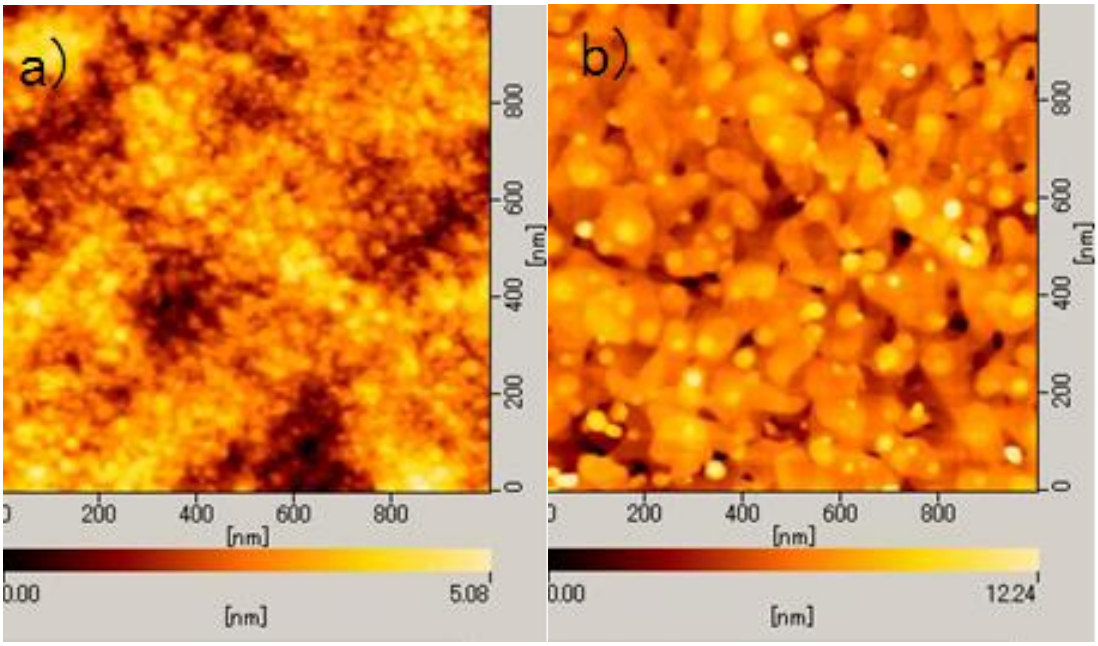

Figure 4.9 AFM image of the $BaZrO_3$ film deposited on the MgO substrate.

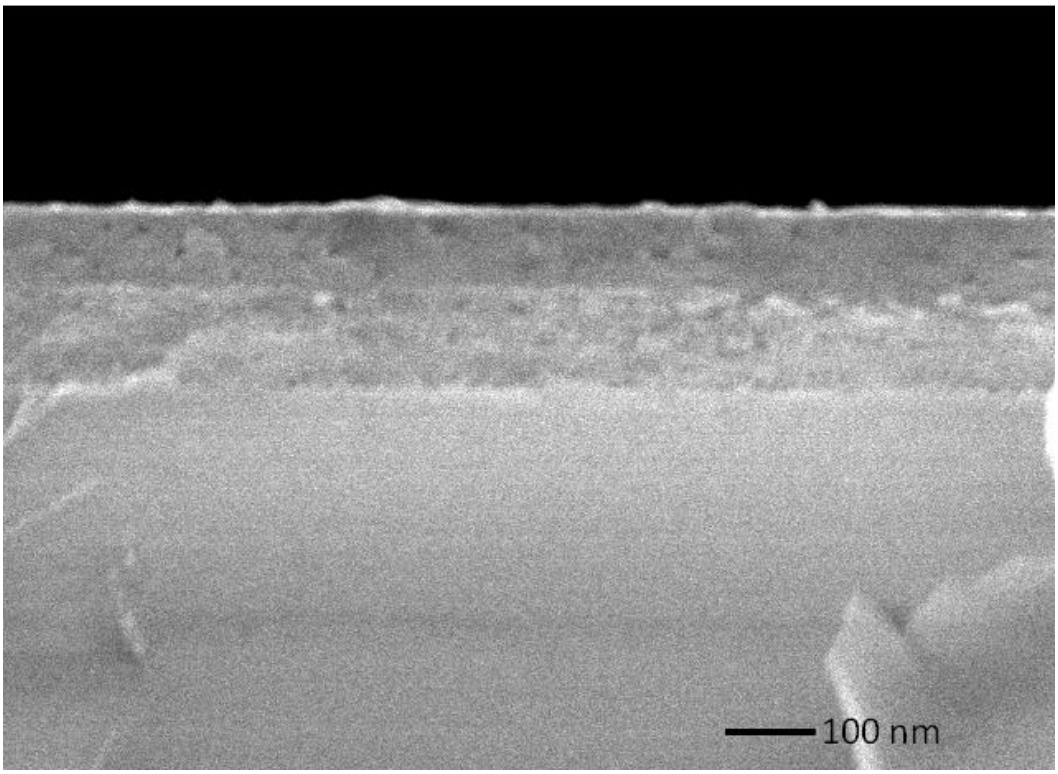

Figure 4.10 Cross-sectional SEM image of the $BaTiO_3/BaZrO_3$ thin film deposited on MgO(100) substrate annealed at 800 °C.

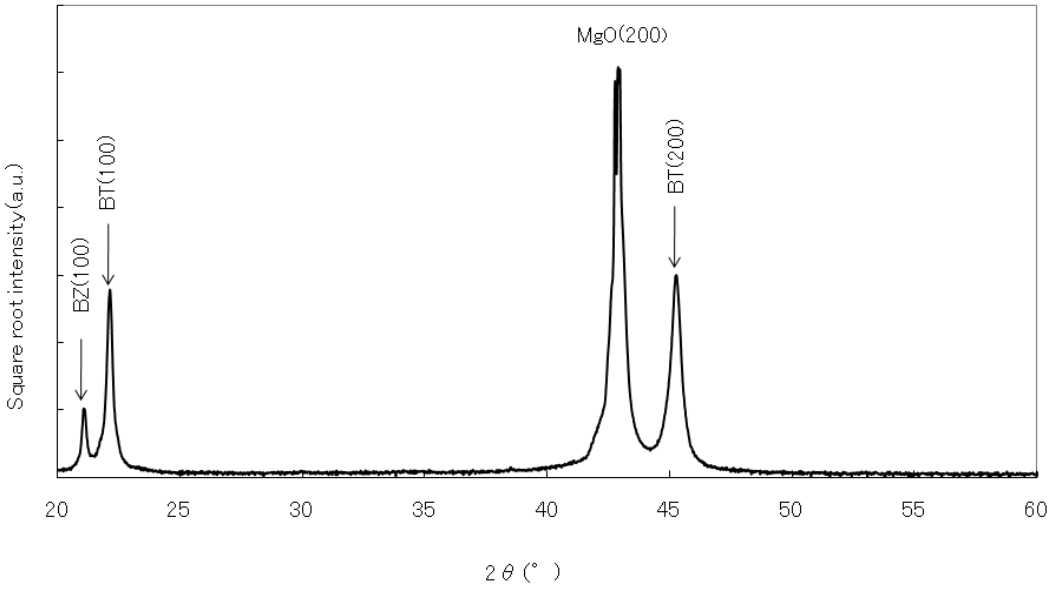

Figure 4.11 XRD pattern of the $BaTiO_3/BaZrO_3$ thin film deposited on MgO(100) substrate annealed at 800 °C.

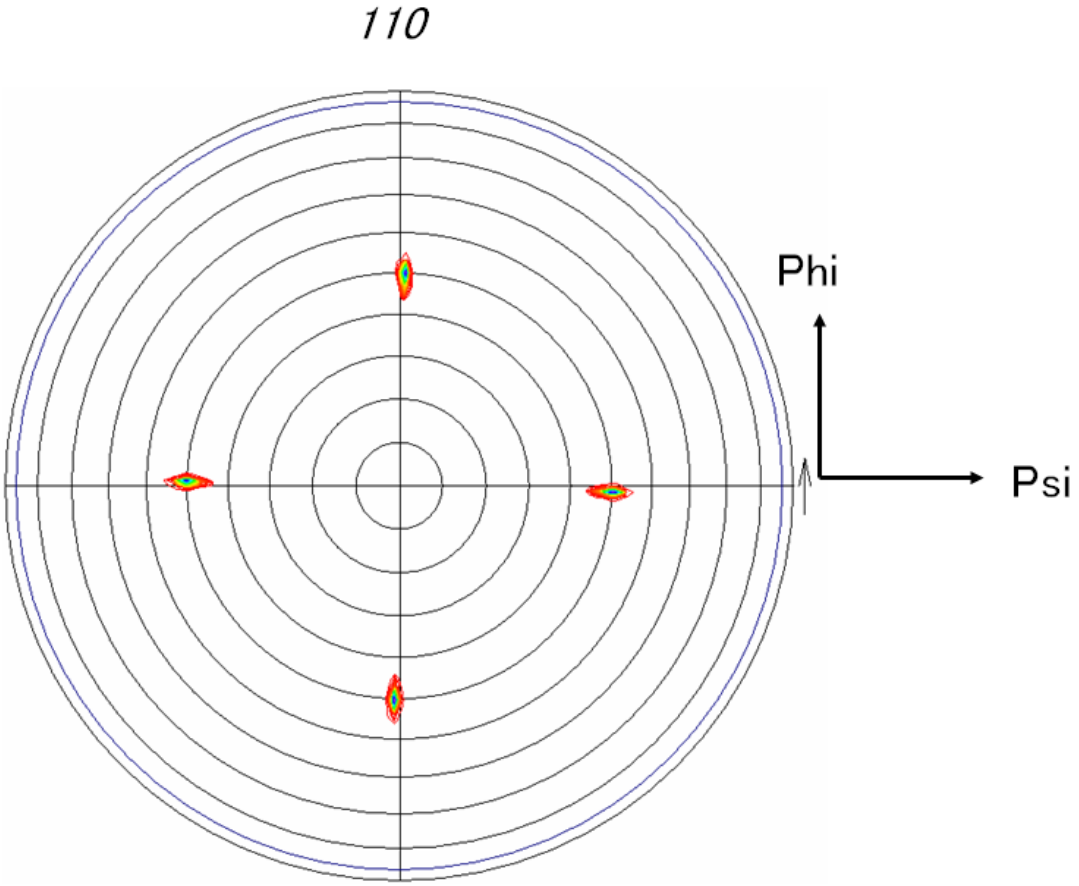

Figure 4.12 X-ray pole figure measured at a fixed 2θ angle corresponding to the *110* reflection of the $BaTiO_3/BaZrO_3$ thin film deposited on MgO(100) substrate annealed at 800 °C.

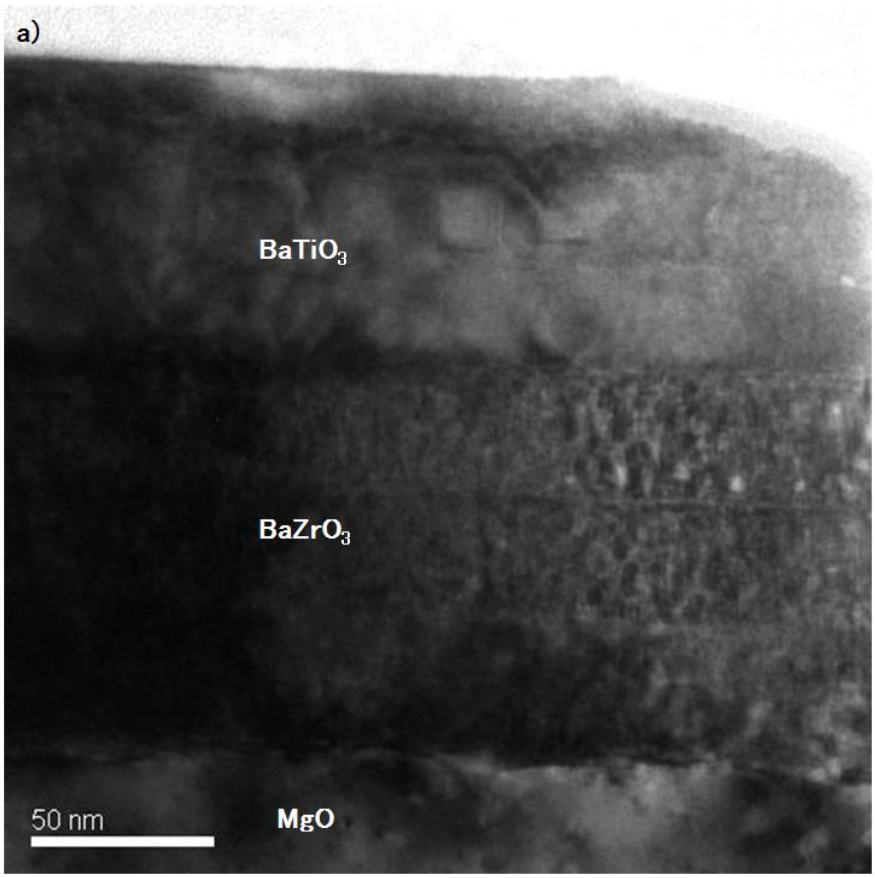

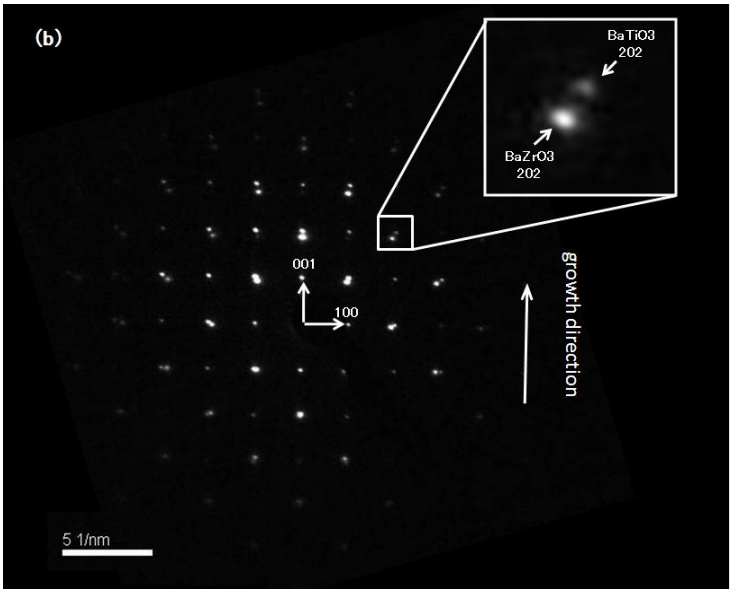

Figure 4.13 (a) Cross-sectional TEM images of the $BaTiO_3/BaZrO_3$ thin film deposited on the MgO(100) substrate. (b) SAED pattern of the $BaTiO_3/BaZrO_3$ thin film deposited on the MgO(100) substrate.

Figure 4.15 shows a cross-sectional bright-field TEM image of the boundary between the $BaZrO_3$ layer and the $BaTiO_3$ layer of the $BaTiO_3/BaZrO_3$ thin film deposited on the MgO(100) substrate. The number of unit cells in 10 nm of the $BaTiO_3$ and $BaZrO_3$ layers was found to be 25 and 24, respectively. The lattice constant of the $BaZrO_3$ and $BaTiO_3$ layers was calculated to be 0.400 nm and 0.417 nm, respectively.

From the calculation, the lattice mismatch of $BaZrO_3$ and $BaTiO_3$ is 0.017 nm. The lattice mismatch for 25 lattices is 0.425 nm; this is the same as the length of a single lattice of $BaZrO_3$. Edge dislocations were observed periodically along the entire interface with a period of approximately 25 and 24 unit cells in the $BaTiO_3$ and $BaZrO_3$ lattices, respectively, which is in good agreement with the lattice mismatch of $BaZrO_3$ and $BaTiO_3$.

Though the epitaxially grown $BaTiO_3$ thin film is able to prepare on MgO(100) by PVD method,[24] epitaxially grown $BaTiO_3$ thin film was not obtained by our method. Inducing the $BaZrO_3$(100) bottom layer enables $BaTiO_3$(100) to grow on $BaZrO_3$(100)/MgO(100) substrate.

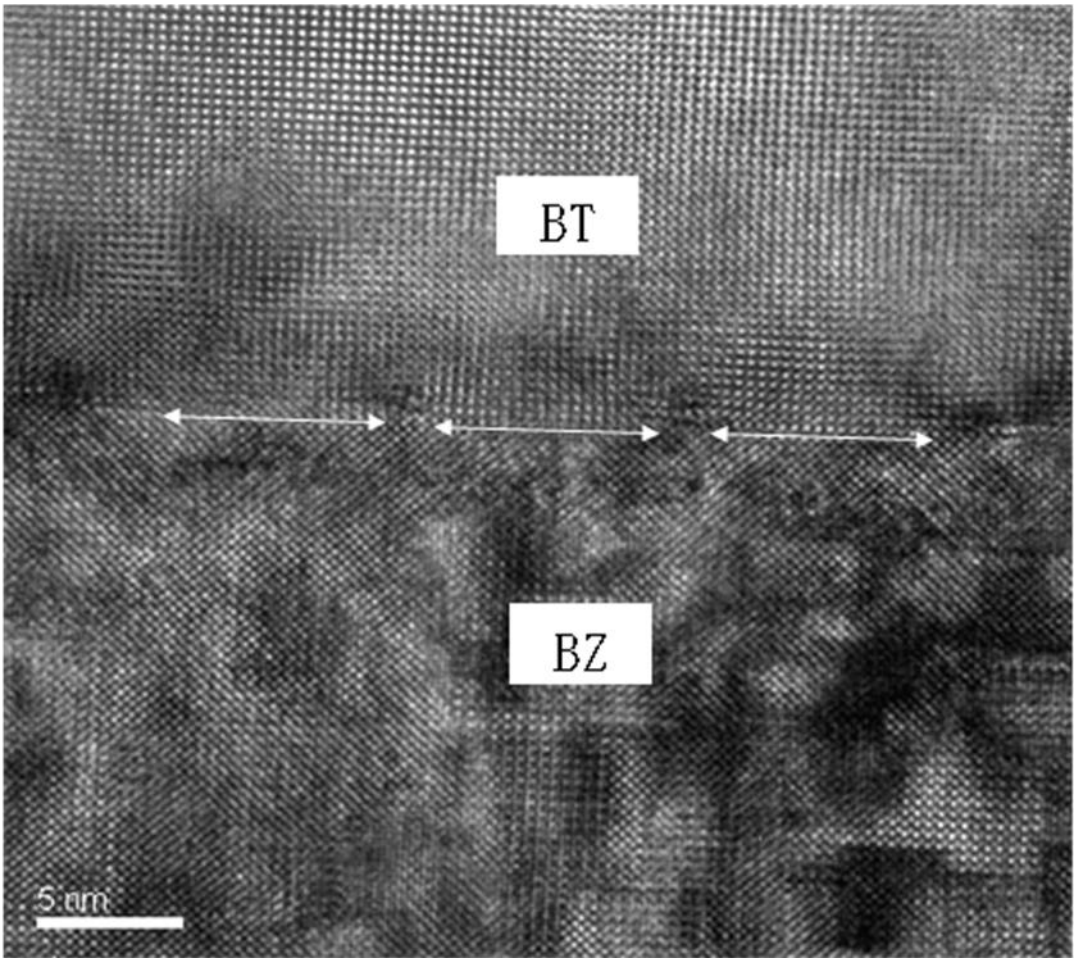

Figure 4.14 Cross-sectional bright-field TEM image of the boundary between the $BaZrO_3$ layer and the $BaTiO_3$ layer of the $BaTiO_3/BaZrO_3$ thin film deposited on the MgO(100) substrate annealed at 800 °C.

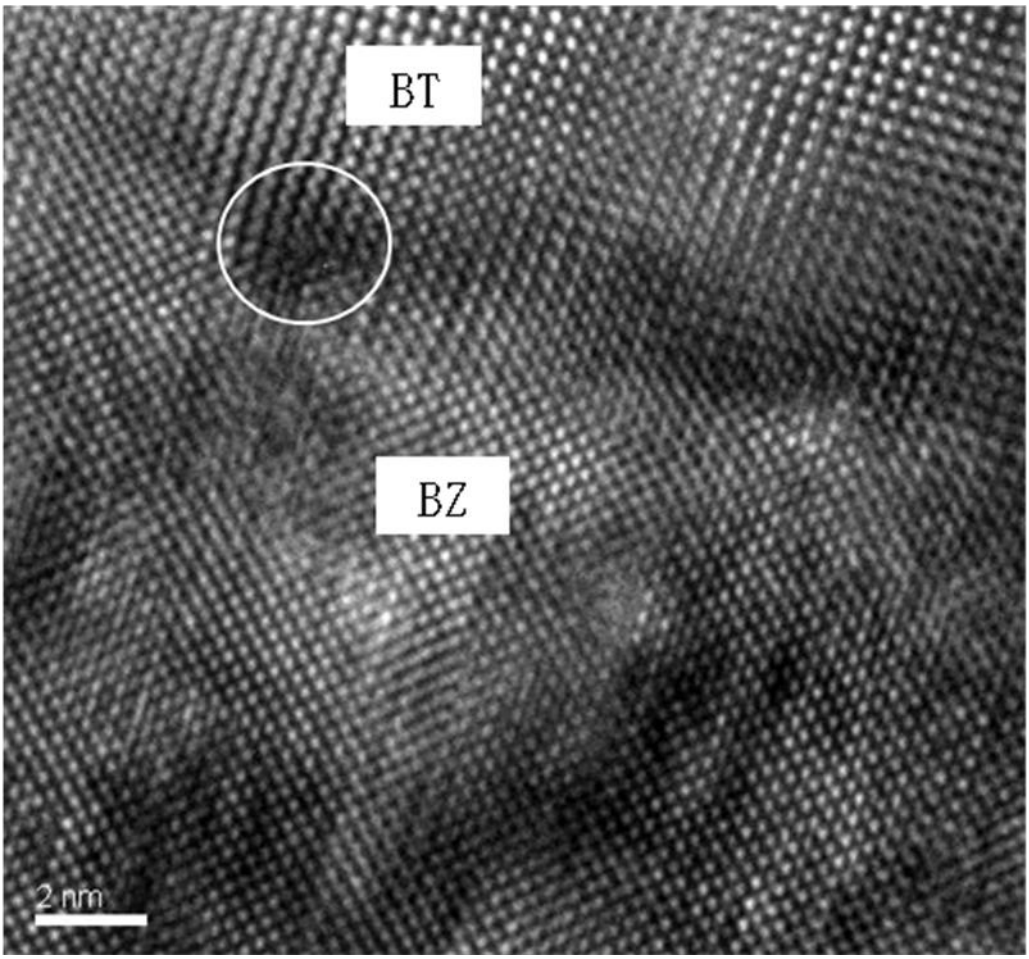

Figure 4.15 Cross-sectional bright-field TEM image of the boundary between the $BaZrO_3$ layer and the $BaTiO_3$ layer of the $BaTiO_3/BaZrO_3$ thin film deposited on the MgO(100) substrate annealed at 800 °C.

4.4 Conclusion

Epitaxially grown (100)-three-axis-oriented $(Ba_{0.7}Sr_{0.3})TiO_3$ thin film on (100) Pt coated (100) MgO substrate and (100) three-axis-oriented $BaTiO_3$ thin film with $BaZrO_3$ buffer layer were prepared on an MgO(100) substrate by the chemical solution deposition method. The growth of the film was found to depend on the annealing condition. TEM revealed cube-on-cube epitaxial growth. The thin films exhibited a (100) three-axis-orientation that followed the (100) orientation of the MgO substrate and the (100) orientation of the Pt or $BaZrO_3$ bottom layer, as observed from an X-ray pole figure measurement and the SAED patterns.

(111)-one-axis-oriented BST thin film have been obtained on Pt(111)/MgO(100) substrate and (100)-three-axis-oriented BST thin film have been obtained on Pt(100)/MgO(100) substrate by CSD method. The three-axis-orientation growth was enabled by epitaxialy growth of the (100) three-axis-oriented BST film on Pt(100) film. Obtained single-crystal-like perovskite (100) three-axis-oriented BST thin film was characterized by SEM, XRD, X-ray pole figure measurement, TEM and SAED. The electrical properties of the thin films show a significant dependence on their orientation and morphology.

The morphology and the crystallinity of the films can be controlled by changing the annealing condition; moreover, the preparation of thin films using the present method will be useful for the production of thin film devices using BST.

(100) three-axis-oriented $BaTiO_3/BaZrO_3$ thin film was deposited on an MgO(100) substrate by the CSD method. The obtained perovskite (100) three-axis-oriented $BaTiO_3/BaZrO_3$ thin films were characterized by XRD, X-ray pole figure measurement, TEM, and SAED.

Annealing at 800 °C gives the high ion mobilities. These enabled atoms rearrange into hetero-epitaxial growth on single crystal substrates. In comparison, Annealing at 650 °C gives the low ion mobilities. This led to the atoms being randomly nucleated. This technique enables to control the orientation and the morphology of the BT and BST thin film prepared by CSD method.

Moreover dielectric constant and tunability of the film can be controlled by the orientation and the morphology of the film, the fabrication of the thin films using the present method will be useful for the production of thin film devices using BT and BST.

4.5 References

[1] Kai-Huang Chen, Ying-Chung Chen, Zhi-sheng Chen, Cheng-Fu yang Ting-Chang Chang, Appl. Phys. A, **89** (2007) 533.

[2] T. Hosokura, Y. Sakabe and M. Kuwabara, J.Sol-Gel Soc. & Technol., **33** (2005) 221.

[3] Spartak Gevorgian, *Ferroelectrics in Microwave Devices, Circuits and Systems Physics, Modeling, Fabrication and Measurements*, Springer-Verlag London Limited (2009).

[4] Takakiyo Harigai, Song-Min Nam, Hirofumi Kakemoto, Satoshi Wada, Keisuke Saito, Takaaki Tsurumi, Thin Solid Films, **509** (2006) 13.

[5] Dharmadhikari, V. S., Grannemann, W. W: Journal of Applied Physics, **53** (1982) 8988.

[6] C. M. Chu and P. Lin, Appl. Phys. Lett., **70** (1997) 249.

[7] D. Y. Wang, J. Wang, H. L. W. Chan, and C. L. Cho**y**, J. Appl. Phys., **101** (2007) 043515.

[8] Osamu Nakagawara, Toru Shimuta, Takahiro Makino, Seiichi Arai, Hitoshi Tabata, and Tomoji Kawai, Appl. Phys. Lett., **77** (2000) 3257.

[9] Chiba T, Itoh K, and Matsumoto O., Thin Solid Films, **300** (1997) 6.

[10] H. Funakubo, Y. Takeshima, D. Nagano, K. Shinozaki, N. Mizutani, J. Mater. Res., **13** (1998) 3512.

[11] Theodor Schneller, Rainer Waser, Ferroelectrics, **267** (2002) 293.

[12] F. F. Lange, Science, **273** (1996) 903.

[13] Robert. W. Schwartz, Theodor Schneller, Rainer Wase, C. R. Chimie, **7** (2004) 433.

[14] Francis S. Galasso: Structure and Properties of Inorganic Solids, Pergamon Press Inc., (1970).

[15] Satoshi WADA, Takeyuki SUZUKI and Tatsuo NOMA, Jpn. J. Appl. Phys., **34** (1995) 5368.

[16] S. Hoffmann, R. Waser, Journal of the European Ceramic Society, **19** (1999) 1339.

[17] Tadasu Hosokura, Akira Ando and Yukio Sakabe, Key Engineering Materials, **320** (2006) 81.

[18] Shinichi Ito, Hiroshi Funakubo, Ivoyl P. Koutsaroff, Marina Zelner, and Cervin-Laery, Appl. Phys. Lett. **90** (2007) 14910.

[19] P X H Zhu, L P Yong, H F Tian, W Peng, J Q Li and D N Zheng, J.Phys. Condens. Matter, **18** (2006) 4709.

[20] Anquan Jaiang, Mattew Dawber, James F. Scott, Can Wang, Piero Migliorato and Marty Gregg ,Jpn. J Appl. Phys., **42** (2003) 6973.

[21] Yutaka Takeshima, Katsuhiko Tanaka and Yukio Sakabe, Jpn. J. Appl. Phys., **39** (2000) 5389.

[22] S. H. Wemple, Physical review B, **2** (1970) 2679.

[23] L. Hafid, G. Godefroy, A. EI Idrissi and F. Michel-Calendini, Solid State Communications, **66** (1988) 841.

[24] Wen-Ching Shin, Yuan-Sung Liang, and Mu-Shiang Wu, Jpn. J. Appl. Phys., **47** (2008) 7475.

Chapter 5

Artificial superlattices fabricated by chemical solution deposition

5.1 Introduction

Barium titanate and/or barium strontium titanate thin films have been in increasing demand as ferroelectric materials for the fabrication of ferroelectric memory devices,[1] multilayer capacitors,[2] optical modulators,[3] and other devices. Paraelectric thin films are attractive dielectrics for use in decoupling capacitors and high-frequency voltage-tunable microwave circuits, such as voltage-controlled oscillators (VCOs), tunable filters and phase shifters.[4] In recent years, there has been increasing interest in the synthesis of artificial superlattices of oxide materials because they have the potential to drastically improve ferroelectric properties.[5] Many studies concerning the $SrTiO_3/BaTiO_3$ system[6-9] have succeeded in fabricating artificial superlattices. Their superlattices have shown behaviors different from those of solid solution $Ba_xSr_{1-x}TiO_3$ (BST).

Artificial superlattices of oxide materials have been prepared by various vapor deposition techniques, such as RF sputtering,[10,11] pulsed laser deposition,[12,13] and molecular beam epitaxy.[14,15] To improve the dielectric properties of perovskite-type artificial superlattices, the thickness of the layer must be less than 10 nm, and each layer must grow highly epitaxially. Vapor deposition techniques are suitable for preparing thin films with thicknesses of less than 10 nm because these techniques can deposit at the atomic level. Nevertheless, to our knowledge, there has been no report on highly oriented $SrTiO_3/BaTiO_3$ artificial superlattices with a thickness of less than 10 nm prepared by the chemical solution deposition (CSD) method. CSD of $BaTiO_3$ or $SrTiO_3$ at temperatures of approximately 600–800 °C typically results in a poly-crystalline, granular film because of the trend toward homogeneous nucleation in the pyrolyzed precursor.[16-18] The CSD method utilized for the synthesis of various perovskite-type thin films can be applied to large wafers (typically from 4 to 8 inches) and possesses definite advantages for the formation of such films with typical thicknesses from 100 nm to 400 nm. These advantages include good compositional homogeneity, stoichiometry control, high purity, and intermediate processing temperatures. CSD processing requires inexpensive, standard laboratory equipment for the formation of such thin films.[19]

In this chapter, the preparation of (100)-oriented $SrTiO_3/BaTiO_3$ artificial superlattices with a thickness of 7 nm by CSD is concerned. The experimental procedure was modified by preparing a (100) three-axis-oriented BST thin film on a Pt(100)/MgO(100) substrate and a (100) three-axis-oriented $BaTiO_3/BaZrO_3$ thin film deposited on an MgO(100) substrate by the CSD method.[20]

5.2 The (100)-oriented $SrTiO_3/BaTiO_3$ artificial superlattices fabricated by chemical solution deposition

Pt(100)/MgO(100) substrates were used to fabricate $SrTiO_3/BaTiO_3$ artificial superlattices by the CSD method. The Pt(100) films were epitaxially grown on a MgO(100) wafer at 600 °C by dc sputtering. A 0.07 M chemical solution was prepared by dissolving $Ba(CH_3COO)_2$ or $Sr(CH_3COO)_2$ and $Ti(O\text{-}i\text{-}C_3H_7)_4$ at a 1:1 molar ratio in a mixed solvent of acetic acid and ethylene glycol monoethylether. The chemical solution was deposited by dispersing it on the substrate, following which spin coating was performed at 4,000 rpm for 30 s. Subsequently, the film was dried on a hot plate at 150 °C for 3 min. The dried and coated films were annealed by RTA at 800 °C for 30 min at a heating rate of 300 °C/min. To prepare $SrTiO_3/BaTiO_3$ artificial superlattices, the deposition procedure was repeated 20 times. Pt dots with a diameter of 0.5 mm were sputtered by placing a mask on the $SrTiO_3/BaTiO_3$ artificial superlattices to form metal-dielectric-metal (MDM) capacitors to investigate their dielectric nature. Crystal characterizations were performed by X-ray diffraction (XRD) (Model RINT-KI, Rigaku, Tokyo, Japan) and Micro X-ray diffraction (μ-XRD) (D8 DISCOVER with GADDS, Bruker, Wisconsin, USA). The High-angle annular dark-field scanning transmission electron microscopy (HAADF-STEM) images and annular bright field scanning transmission electron microscopy (ABF-STEM) images were taken by spherical aberration correctors scanning transmission electron microscopy (Cs-STEM) (ARM-200F, JEOL, Tokyo, Japan). STEM image and EDS mapping were taken by FE-TEM/EDX（JEOL JEM-2200FS/JED-2300T, Tokyo, Japan）Cross-sectional images of the obtained film were taken by a field emission-scanning electron microscope (FE-SEM) (Model S-5000, Hitachi, Tokyo, Japan). Small signal ac (100 mV, 1 kHz) capacitance and loss tangent were measured using an LCR meter (HP 4284A, Hewlett-Packard, California, USA).

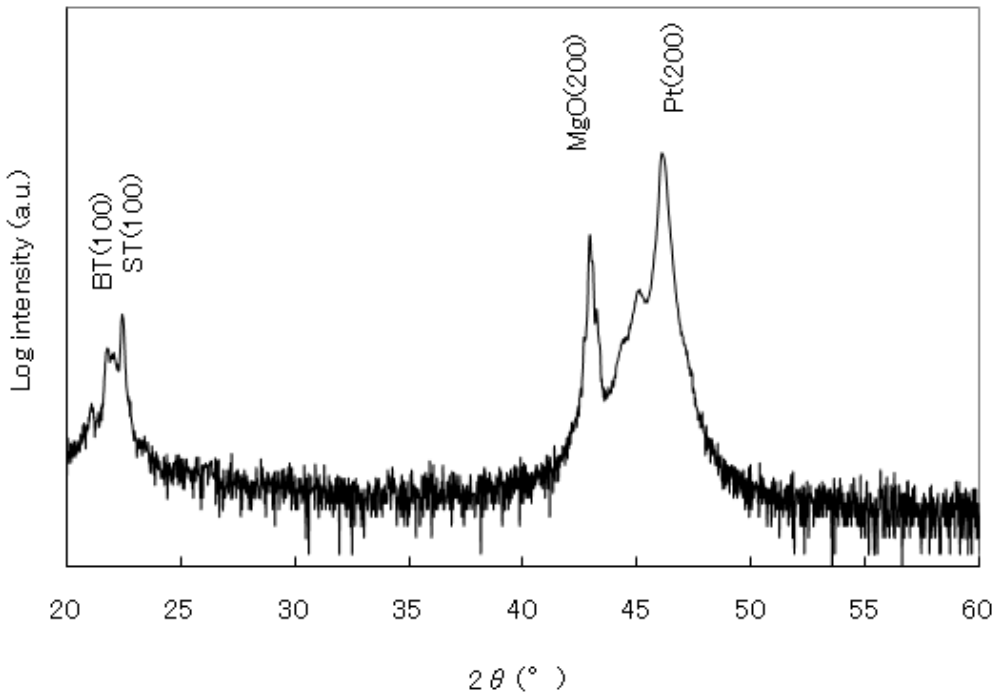

Figure 5.1. The XRD pattern of the $SrTiO_3/BaTiO_3$ deposited on Pt(100)/MgO(100) substrate.

Figure 5.1 shows the XRD pattern of the $SrTiO_3/BaTiO_3$ deposited on a Pt(100)/MgO(100) substrate. This XRD pattern can be indexed to $SrTiO_3$ (cubic; JCPDS: 35-0734), $BaTiO_3$ (cubic; JCPDS: 31-0174), MgO (JCPDS: 36-1377), and Pt (JCPDS: 04-0802). Strong (*h*00) reflections were observed for this $SrTiO_3/BaTiO_3$ deposited on a Pt(100)/MgO(100) substrate, which indicated that the perovskite $SrTiO_3(100)/BaTiO_3(100)$ were hetero epitaxially grown on the Pt(100)/MgO(100) substrate. Figure 5.2 shows the μ-XRD pattern of the $SrTiO_3/BaTiO_3$ deposited on a Pt(100)/MgO(100) substrate. In the μ-XRD pattern, diffraction peaks are observed at 21.25°, 21.892°, 22.482°, 23.040°, 23.713° and 24.321°. Diffraction peak at 21.892 ° and 22.482° are diffraction peak of $BaTiO_3$ and $SrTiO_3$ respectively. Diffraction peak at 21.25°, 23.040°, 23.713° and 24.321° are super diffractions by the artificial superlattice of $SrTiO_3/BaTiO_3$. This result indicates that $SrTiO_3/BaTiO_3$ artificial superlattice is obtained by our method. According to cross-sectional SEM and STEM imaging, the thickness of the $SrTiO_3(100)/BaTiO_3(100)$ artificial superlattices was 140 nm, and the thickness of each artificial superlattice was 7 nm. A clear boundary was observed between the $SrTiO_3$ and $BaTiO_3$ layers. In figures 5.3 and 5.4, EDS mapping indicated that the $SrTiO_3$ and $BaTiO_3$ layers were fabricated without intermixing. To determine the nature of the growth of the $SrTiO_3(100)/BaTiO_3(100)$ artificial superlattices, cross-sectional HAADF-STEM images and annular bright field scanning transmission electron microscopy (ABF-STEM) images were obtained by Cs-STEM. Cs-STEM was operated at 200 kV. The HAADF-STEM images were taken using an annular detector of which solid angle was conditioned in the range from 73 to 194 mrad. The ABF-STEM images were taken using an annular detector of which solid angle was conditioned in the range from 10 to 44 mrad. ABF-STEM images can determine the location of columns containing light elements, such as O columns, by comparison with HAADF-STEM images.[21, 22]

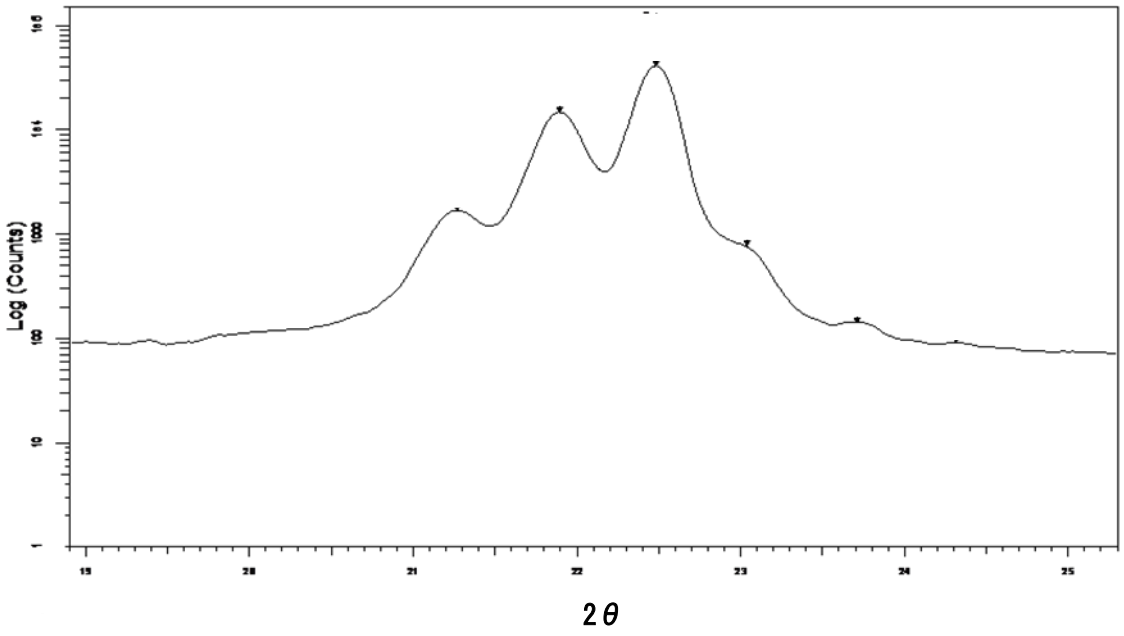

Figure 5.2. μ-XRD pattern of the $SrTiO_3/BaTiO_3$ deposited on a Pt(100)/MgO(100) substrate.

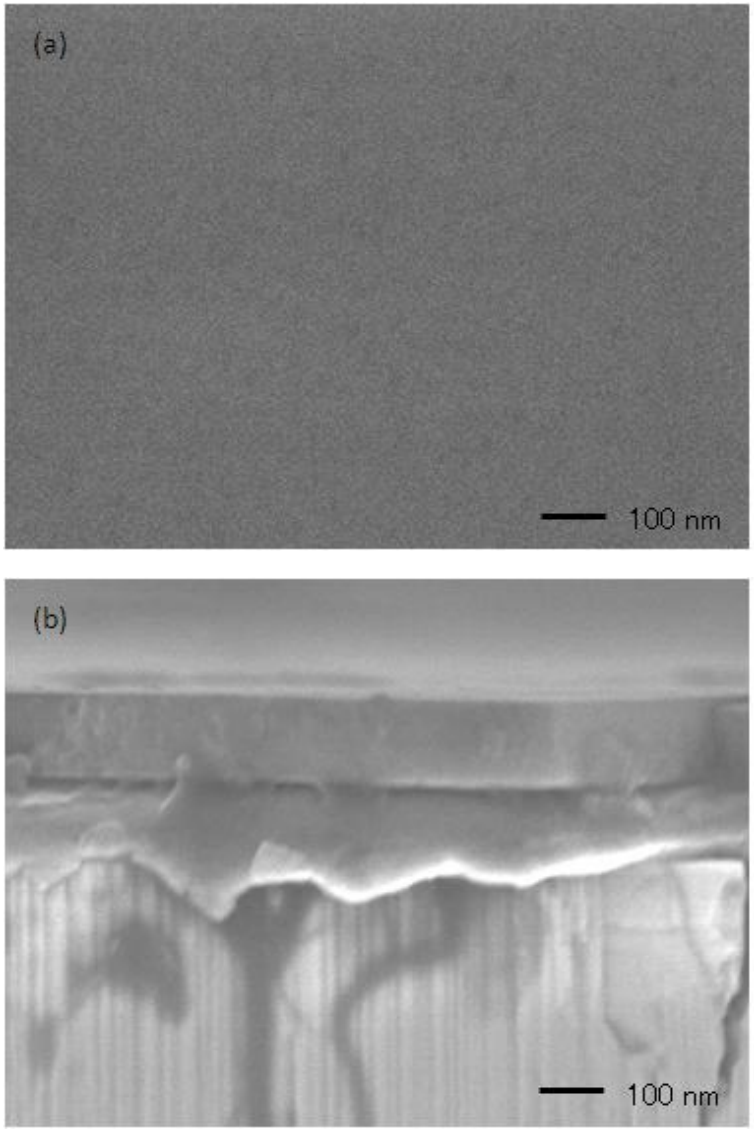

Figure 5.3. (a) Surface and (b) Cross-sectional FE-SEM image of the $SrTiO_3/BaTiO_3$ artificial superlattices.

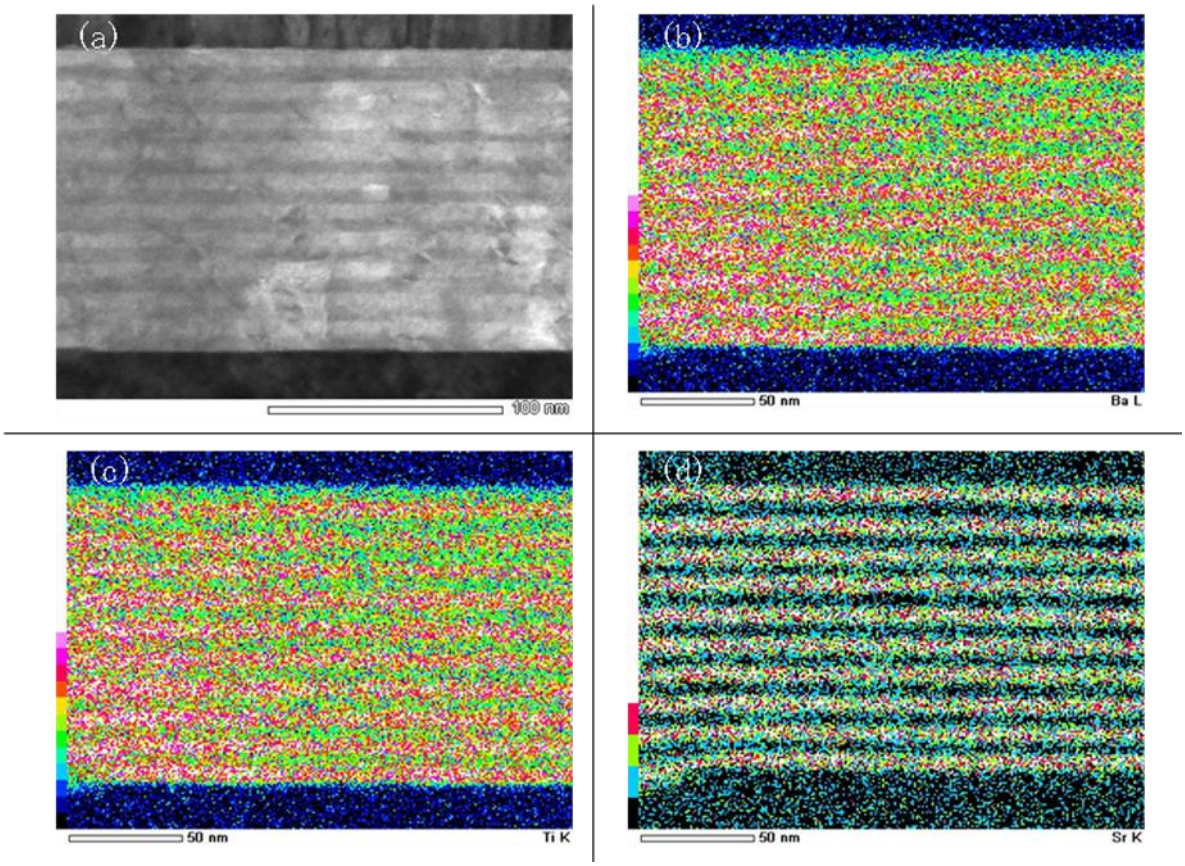

Figure 5.4. Cross-sectional (a) STEM image and (b) EDS mapping of the Ba atom, (c) EDS mapping of the Ti atom and (d) EDS mapping of the Sr atom of the $SrTiO_3/BaTiO_3$ artificial superlattices.

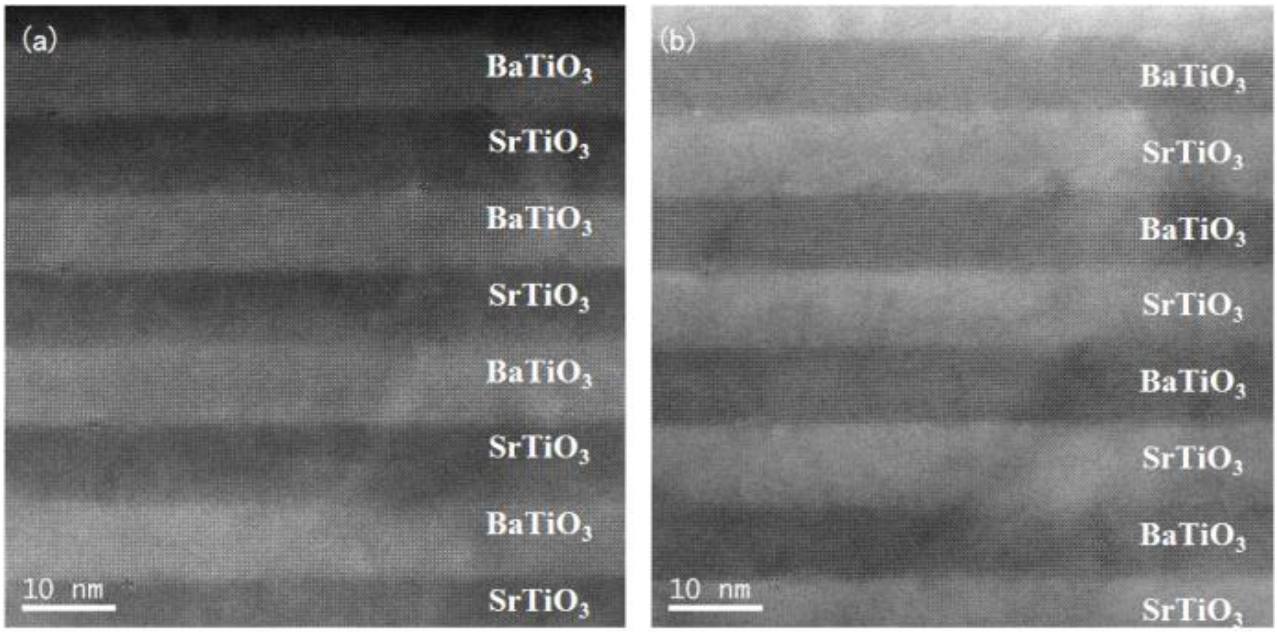

Figure 5.5. (a) HAADF-STEM image and (b) ABF-STEM image of the same view of the $SrTiO_3/BaTiO_3$ artificial superlattices.

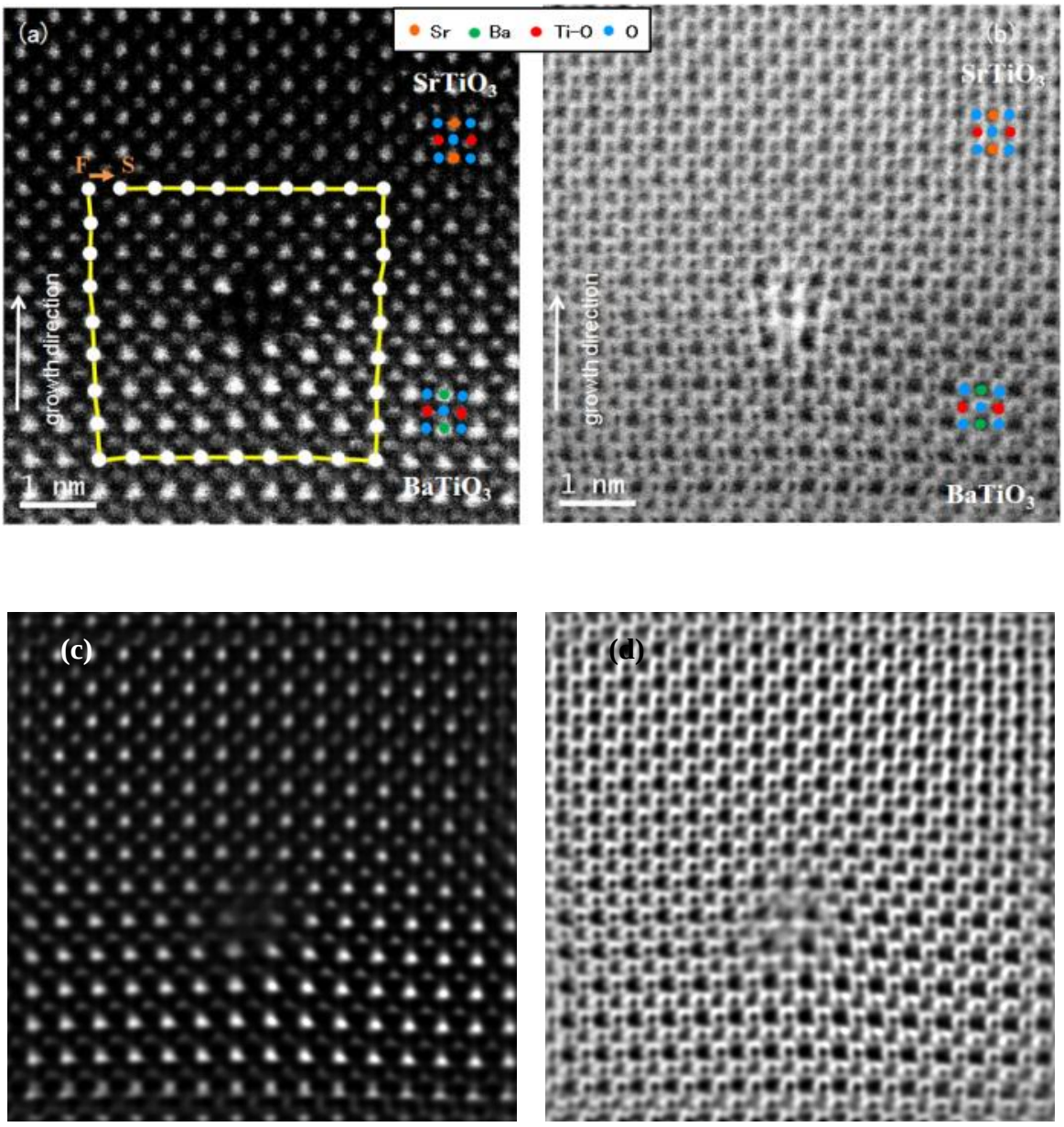

Figure 5.6. (a) HAADF-STEM image, (b) ABF-STEM image, (c) Noise reduced HAADF-STEM image and (d) Noise reduced ABF-STEM image of the boundary between the $SrTiO_3$ and $BaTiO_3$ layers; the view along the [001] orientation is shown.

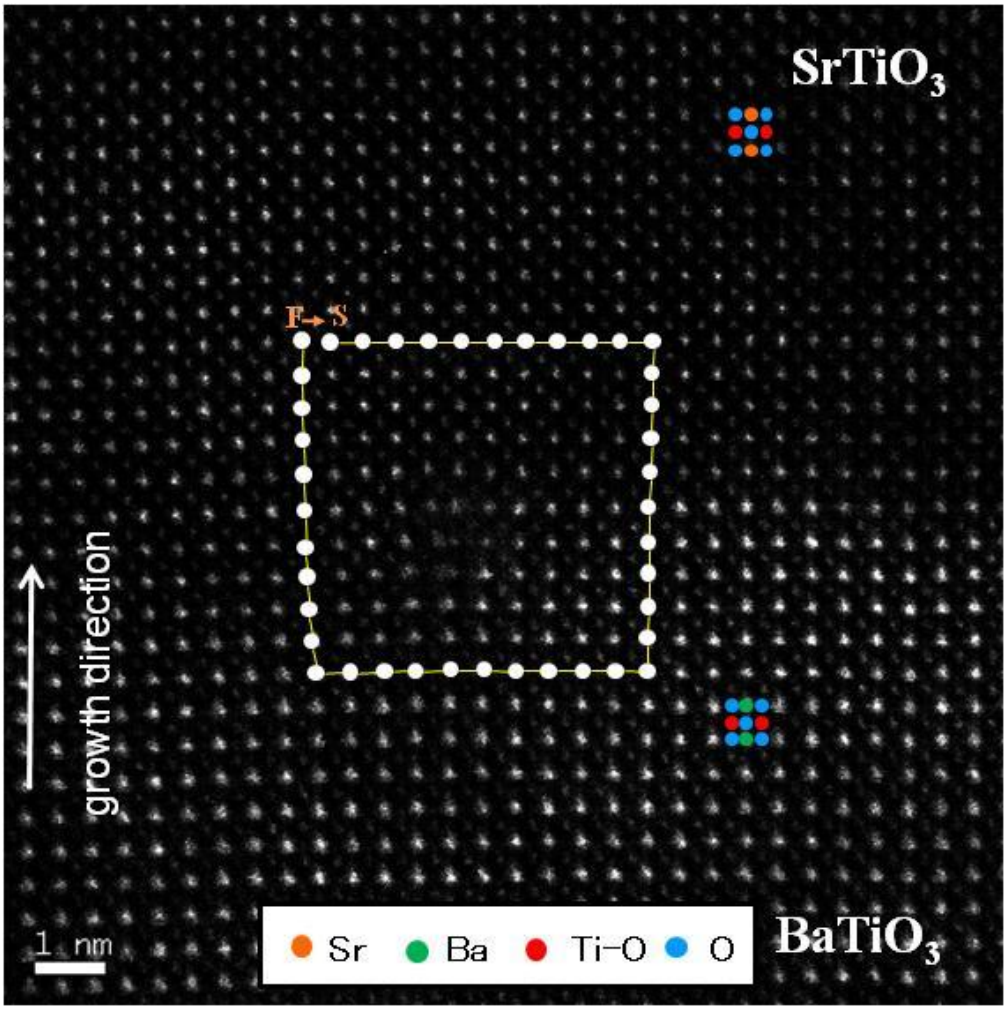

Figure 5.7. HAADF-STEM image of the boundary between the $SrTiO_3$ and $BaTiO_3$ layers; the view along the [001] orientation, in which both $BaTiO_3$ and $SrTiO_3$ lattices are distorted, is shown.

Figure 5.5(a) shows a HAADF-STEM image of the $SrTiO_3/BaTiO_3$ artificial superlattices, and 5.5(b) shows the ABF-STEM image of the $SrTiO_3/BaTiO_3$ artificial superlattices. The $SrTiO_3$ and $BaTiO_3$ layers were grown highly epitaxially and were effectively single-crystal-like with no visible grain boundaries. The HAADF-STEM observation results revealed that the $SrTiO_3/BaTiO_3$ artificial superlattices exhibited a strong cube-on-cube epitaxy. ABF-STEM imaging provides a contrast, the Z-contrast, which is monotonically proportional to the atomic number. The boundary between the $SrTiO_3$ and $BaTiO_3$ layers is clear. The $SrTiO_3$ layer is brighter than the $BaTiO_3$ layer because the atomic number of Sr (Z=38) is lower than the atomic number of Ba (Z=56).

Figure 5.6(a) shows the HAADF-STEM images of the boundary between the $SrTiO_3$ and $BaTiO_3$ layers as viewed along the [001] orientation. The heavy Ba and Sr columns are clearly visible, and the lighter Ti-O columns are also visible; however, the pure O columns are not. The Z-contrast of the HAADF-STEM image indicated that the $SrTiO_3$ layer and $BaTiO_3$ layer were fabricated without the intermixing of A-site atoms. Figure 5.6(b) shows the ABF-STEM image of the $SrTiO_3$ layer and the $BaTiO_3$ specimen, where the O columns are now visible, along with the Ba, Sr and Ti-O columns, which were previously evident in the HAADF-STEM image of the same layer. The Ba, Sr, Ti-O, and O columns can be clearly distinguished by comparing the HAADF-STEM and ABF-STEM images. The arrangement of these columns indicates that the (100) single-crystal-like perovskite layer was epitaxially grown, which is in good agreement with the results obtained by XRD.

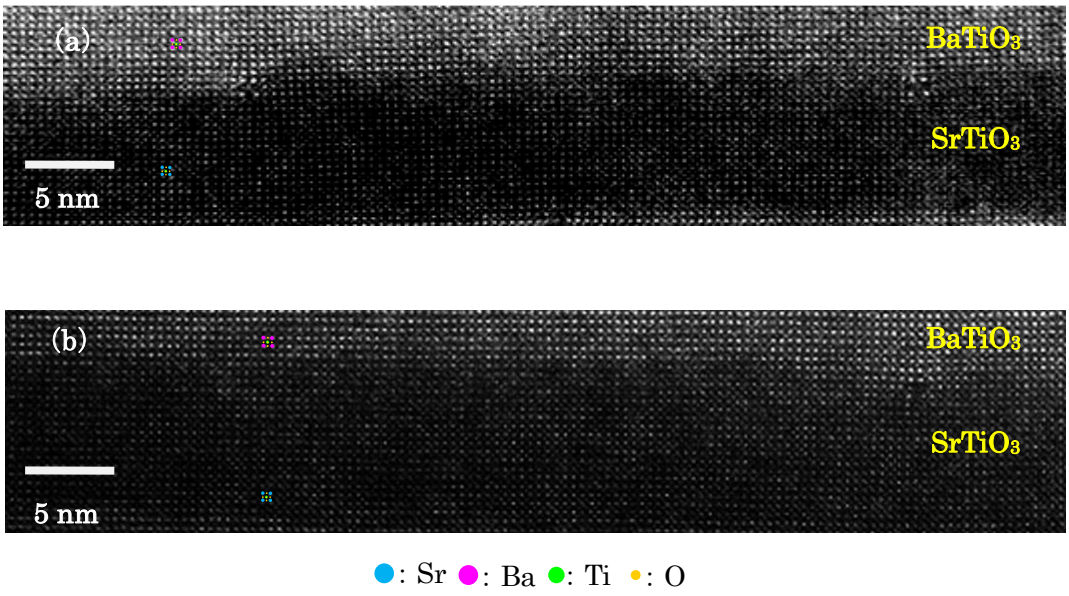

Figure 5.8 Low magnified HAADF-STEM image of the boundary between the $SrTiO_3$ and $BaTiO_3$ layers; the view along the [001] orientation is shown. (a) and (b) are taken from different point of view.

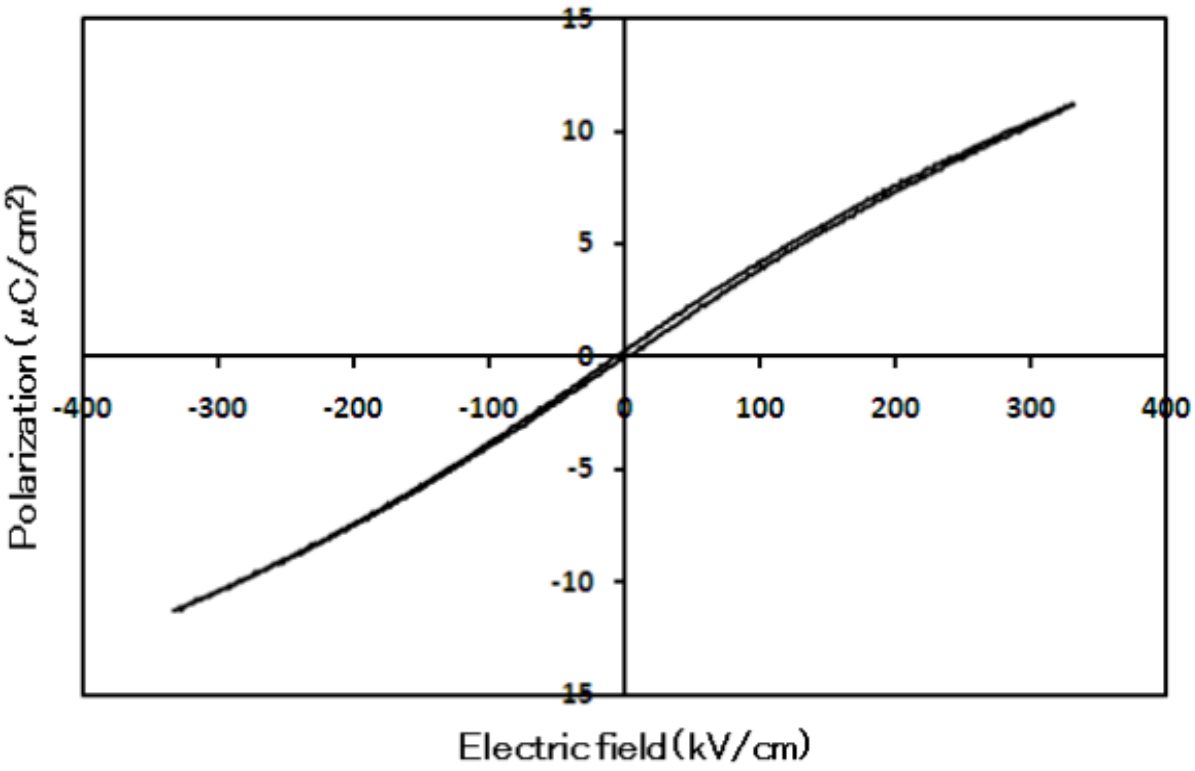

Figure 5.9. P-E hysteresis loop of the $SrTiO_3/BaTiO_3$ artificial superlattices in the MDM capacitor.

Figure 5.7 shows the HAADF-STEM images wherein both the $BaTiO_3$ and $SrTiO_3$ lattices are distorted. Edge dislocations are observed, and defects in the Sr, Ba, Ti-O, and O columns can be identified in the center of the image. In figure 4, the HAADF-STEM image shows that only the $BaTiO_3$ lattices are distorted. Edge dislocations are visible, and defects in the Ba column can be identified in the center of the image. The observation sample was not sufficiently thin to obtain the ABF-STEM image around this region. There are two types of defects in the boundary between the $SrTiO_3$ and $BaTiO_3$ layers: defects in the Ba, Sr, Ti-O, and O columns (figure 5.6) and defects in the Ba column (figure 5.7). The defects can only be observed in the boundary between the $SrTiO_3$ and $BaTiO_3$ layers. There was a mismatch of 3.0% between the in-plane lattice parameters of the $SrTiO_3$ and $BaTiO_3$ layers. This lattice mismatch induced the defects between the $SrTiO_3$ and $BaTiO_3$ layers. In figure 5.6 and figure 5.7, a misfit dislocation was introduced at the heteroepitaxial interface to relax misfit strain. Both in figure 5.6 and figure 5.7 a misfit dislocation was introduced at the heteroepitaxial interface to relax misfit strain. The dislocation was a pure edge dislocation with a Burgers vector of type [100], the same edge dislocation was observed in $BaTiO_3$ films epitaxially grown on (100) $SrTiO_3$ substrates.[23] As misfit between $SrTiO_3$ and $BaTiO_3$ is as large as 3.0 %, approximately 33 unit cells are required to relax the mismatch which can calculated to be around 13 nm. In figure 5.8, the misfit dislocations were not observed at periodic distance around 13 nm. Another study is underway to elucidate the formation mechanism of these defects. Controlling the intermixing at heterointerfaces is usually difficult for vapor deposition techniques because a high temperature and high energy are employed for the film deposition, and the stoichiometry of the deposition film changes with the deposition conditions in a complicated manner.[24] However, in this case, the $SrTiO_3/BaTiO_3$ artificial superlattices were fabricated without intermixing by the CSD method. Thus, the CSD method is proposed to be suitable to fabricate $SrTiO_3/BaTiO_3$ artificial superlattices without intermixing at heterointerfaces and with good stoichiometry of the deposited film. The capacitance (100 mV, 1 kHz) of the $SrTiO_3/BaTiO_3$ artificial superlattices in the MDM capacitor was 5.2 nF. The dielectric constant of the $SrTiO_3/BaTiO_3$ artificial superlattices was calculated to be approximately 400. In reference [20], the dielectric constant of the $Ba_{0.7}Sr_{0.3}TiO_3$ film on the same substrate with similar annealing conditions was 1200. The dielectric constant of the $SrTiO_3/BaTiO_3$ artificial superlattices is relatively low, compared to the results of the

$Ba_{0.7}Sr_{0.3}TiO_3$. This suppression is due to the size effect of a periodic thickness of the $SrTiO_3/BaTiO_3$ artificial superlattices and lower barium content of the $SrTiO_3/BaTiO_3$ artificial superlattices compare to the $Ba_{0.7}Sr_{0.3}TiO_3$ film.

Figure 5.9 shows the polarization-electric field (P-E) hysteresis loop of the $SrTiO_3/BaTiO_3$ artificial superlattices in the MDM capacitor. The hysteresis loop indicated paraelectric behavior. This result differs from the one obtained by Tabata et al.,[5] in which the $SrTiO_3/BaTiO_3$ artificial superlattices behaved as ferroelectrics, because inducing the defects between the layers relaxed the misfit strain. Enhancement of the ferroelectric behavior was weakened by relaxing the strain.

5.3 Conclusion

$SrTiO_3(100)/BaTiO_3(100)$ artificial superlattices with 7-nm-thick sublayers were synthesized by the CSD method. A systematic study is underway to elucidate the mechanism of the defects and synthesize a defect-free interface. These findings provides a new approach for fabricating artificial superlattices by CSD, which will drastically improve the material properties and open the door for the wider use of artificial superlattices of oxide materials.

5.4 References

[1] Chen, K.-H.; Chen, Y.-C.; Chen, Z.-S.; Yang, C.-F.; Chang, T.-C., Appl. Phys., A, **89** (2007) 533.

[2] Takeshima, Y.; Shiratsuyu, K.; Takagi, H; Sakabe, Y., Jpn. J. Appl. Phys., **36** (1997) 5870.

[3] Tang, P.; Towner, D. J.; Meier, A. L.; Wessels, B. W., Appl. Phys. Lett., **85** (2004) 4615.

[4] Gevorgian, S., Ferroelectrics in Microwave Devices, Circuits and Systems Physics, Modeling, Fabrication and Measurements; Springer-Verlag : London, (2009).

[5] Tabata, H.; Tanaka, H.; Kawai, T, Appl. Phys. Lett., **65** (1994) 1970.

[6] Iijima, K.; Terashima, T.; Bando, Y.; Kamigai, K.; Terauchi, H. , J. Appl. Phys., **72** (1992) 2840.

[7] Tsurumi, T.; Suzuki, T.; Yamane, M.; Daimon, M., Jpn. J. Appl. Phys. Part 1, **33** (1994) 5192.

[8] Tsurumi, T.; Miyasou, T.; Ishibashi, Y.; Ohashi, N., Jpn. J. Appl. Phys. Part 1, **37** (1998) 5104.

[9] Harigai, T.; Nam, S.-M.; Kakemoto, H.; Wada, S.; Saito, K.; Tsurumi, T., Thin Solid Films., **509** (2006) 13.

[10] Dawber, M.; Lichtensteiger, C.; Cantoni, M; Veithen, M.; Ghosez, P.; Johnston, K.; Rabe, K. M.; Triscone, J.-M., Phys. Rev. Lett., **95**1 (2005) 17760.

[11] Hung, C.-L.; Chueh, Y.-L.; Wua, T.-B.; Chou, L.-J., J. Appl. Phys., **97**(2005) 034105.

[12] Nakagawara, O.; Shimuta, T.; Makino, T.; Arai, S.; Tabata, H.; Kawai, T., Appl. Phys. Lett., **77** (2000) 3257.

[13] Qu, B. D.; Evstigneev, M.; Johnson, D. J.; Prince, R. H., Appl. Phys. Lett., **72**(1998) 1395.

[14] Marrec, F. L.; Farhi, R.; Marssi, M. E.; Dellis,J. L.; Karkut, M. G., Phys. Rev. B., **61** (2000) 6447.

[15] Zhao, T.; Chen, Z.-H.; Chen, F.; Shi, W.-S.; Lu, H.-B.; Yang, G.-Z., Phys. Rev. B., **60** (1999) 1697.

[16] Schneller, T.; Waser, R., Ferroelectrics., **267**3 (2002) 29.

[17] Lange, F. F., Science., **273** (1996) 903.

[18] Hosokura, T.; Ando, A.; Sakabe, Y., Key Engineering Materials., **320** (2006) 81.

[19] Schwartz, R. W.; Schneller, T.; Waser, R., C. R. Chimie., **7** (2004) 433.

[20] Hosokura, T.; Kageyama, K.; Takagi, H.; Sakabe, Y., J. Am. Ceram. Soc., **92** (2009) 253.

[21] Findlay, S. D.; Shibata, N.; Sawada, H.; Okunishi, E.; Kondo, Y. ; Yamamoto, T.; Ikuhara, Y., Appl. Phys. Lett., **95** (2009) 191913.

[22] Findlay, S.D.; Shibata, N.; Sawada, H.; Okunishi, E.; Kondo, Y.; Ikuhara, Y., Ultramicroscopy., **110** (2010) 903.

[23] Suzuki, T.; Nishi, Y.; Fujimoto, M., Philos. Mag. A, **79** (1999) 2461.

[24] Ohnishi, T.; Koinuma, H.; Lippmaa, M., Appl. Surf. Sci., **252** (2006) 2466.

Summary

In this study, preparation and structure control of dielectric thin films have been carried out under different processing conditions and with different substrates by CSD. The results can be summarized as follows.

In chapter 2, a novel electrophoretic method that uses a partially hydrolyzed highly concentrated solution of barium and titanium alkoxides was developed in order to prepare $BaTiO_3$ with patterned microstructure. By using electron beam lithography, a micro-patterned mold, that is a mold with an array of air holes of 250 nm arranged in a triangular lattice with a lattice constant of 500 nm was prepared on a $Pt/Ti/SiO_2/Si$ substrate. By combining high-concentration metal alkoxides sol-gel processing, an electrophoretic deposition technique, and electron-beam lithography, barium titanate patterned microstructures were produced. The reflection spectra obtained for the patterned BT films can be interpreted as indicating that PBGs formed in the crystals.
This deposition technique for formation of BT patterned microstructures is revealed to be very promising for fabricating photonic crystals.

In chapter 3, epitaxially grown $(Ba,Sr)TiO_3$ thin films were prepared on platinum-coated silicon substrate by sol-gel method using a $(Ba,Sr)TiO_3$ sol derived from $Ba(CH_3COO)_2$, $Sr(CH_3COO)_2$ and $Ti(O\text{-}i\text{-}C_3H_7)_4$. The morphology of the films was found to depend on the annealing condition. A columnar structure was obtained for $(Ba,Sr)TiO_3$ thin film by annealing at 800 °C and a columnar grain was found to be single crystal by TEM. The columnar grown film exhibits a preferred (111) orientation that follows the (111) orientation of Pt substrate. Measurement of the C-V in MFM was configured in order to demonstrate the ferroelectric properties. Obtained butterfly loops indicate ferroelectricity in the film. Morphology of BST films was controlled by controlling annealing condition by using CSD method. The BST films showed the ferroelectric polarization reversal that indicates ferroelectricity in the film. Columnar grain growth occurs when annealing condition is above decomposition-temperature and

crystallise-temperature. The columnar grown film exhibits a preferred (111) orientation that follows the (111) orientation of Pt substrate. A single columnar grain in BST film is consisted of a single crystal. Dielectric constant of the film differs by the morphology of the film. Columnar grains induce a higher dielectric constant.

TG-DTA measurement under changing heating rate enables us to express the decomposition and the crystallization reaction of CSD solution by using thermal dynamic method. The effective Arrhenius activation energy (Ea) for decomposition and crystallization of the CSD solution for BST film are 124.76 kJ/mol and 361.33 kJ/mol respectively. For heating rate at 300 °C/min (normal annealing speed by RTA), decomposition temperature and crystallization temperature are calculated to be 454 °C and 719 °C respectively. The calculated result implies to decide the drying temperature and annealing temperature for CSD solution. Appling thermal dynamic method is effective to CSD thin film deposition method. Though the annealing temperature is same, the dielectric constant of the BST film changes by the heating rate. The heating rate affects the dielectric constant by changing the grain size of the BST films. Crystallizing temperature grain growth was accelerated. Using thermo-dynamic method enables to reveal the crystallization temperature and to obtain high quality BST film.

In this chapter, the orientation and the morphology of the BT and BST thin films can control and this controlling method is useful for the production of thin film devices using BT and BST.

In chapter 4, epitaxially grown (100)-three-axis-oriented $(Ba_{0.7}Sr_{0.3})TiO_3$ thin film on (100) Pt coated (100) MgO substrate and (100) three-axis-oriented $BaTiO_3$ thin film with $BaZrO_3$ buffer layer were prepared on an MgO(100) substrate by the chemical solution deposition method. The growth of the film was found to depend on the annealing condition. TEM revealed cube-on-cube epitaxial growth. The thin films exhibited a (100) three-axis-orientation that followed the (100) orientation of the MgO substrate and the (100) orientation of the Pt or $BaZrO_3$ bottom layer, as observed from an X-ray pole figure measurement and the SAED patterns.

(100) three-axis-oriented $BaTiO_3/BaZrO_3$ thin film was deposited on an MgO(100) substrate by the CSD method. The obtained perovskite (100) three-axis-oriented $BaTiO_3/BaZrO_3$ thin films were characterized by XRD, X-ray pole figure measurement,

TEM, and SAED.

Annealing at 800 °C gives the high ion mobilities. These enabled atoms rearrange into hetero-epitaxial growth on single crystal substrates. In comparison, Annealing at 650 °C gives the low ion mobilities. This led to the atoms being randomly nucleated. This technique enables us to control the orientation and the morphology of the BT and BST thin film prepared by CSD method. Moreover dielectric constant and tunability of the film can be controlled by the orientation and the morphology of the film, the fabrication of the thin films using the present method will be useful for the production of thin film devices using BT and BST.

In chapter 5 epitaxially grown $SrTiO_3$(100)/$BaTiO_3$(100) artificial superlattices with 7-nm thick layers were synthesized on (100) platinum-coated (100) magnesium oxide substrates by a chemical solution deposition method. HAADF-STEM observation revealed cube-on-cube epitaxial growth. The Z-contrast HAADF-STEM image indicated that the $SrTiO_3$ and $BaTiO_3$ layers were fabricated without the intermixing of A-site atoms. The defects can only be observed in the boundary between the $SrTiO_3$ and $BaTiO_3$ layers. There was a mismatch of 3.0% between the in-plane lattice parameters of the $SrTiO_3$ and $BaTiO_3$ layers. This lattice mismatch induced the defects between the $SrTiO_3$ and $BaTiO_3$ layers. Inducing the defects between the layers relaxed the misfit strain.

This studies' finding provides a new approach for fabricating structure control of dielectric thin films by CSD, which will enable us to improve the material properties drastically and open the door for the wider use of structure control of dielectric thin films of oxide materials.

List of Publications

Chapter 1

Tadasu Hosokura, Koh-ichi Maruyama, Izumi Ohno and Osamu Nittono

"Structure and Magnetic Properties of Co-based Metal Electroless-deposited into Porous Silicon"

Journal of the Surface Finishing Society of Japan, **49** (1998) pp 401-406.

Chapter 2

Tadasu Hosokura, Satoshi Shindo and Makoto Kuwabara

"Preparation of Barium Titanate Patterned Microstructures by a Novel Sol-Electrodeposition Method Using a Highly Concentrated Alkoxide Solution"

Key Engineering Materials, **248** (2003) pp. 69-72.

Tadasu Hosokura, Yukio Sakabe and Makoto Kuwabara

"Preparation of Barium Titanate with Patterned Microstructure by a Novel Electrophoretic Deposition Method"

Journal of Sol-Gel Science and Technology, **33** (2005) pp. 221-228.

Chapter 3

Tadasu Hosokura, Akira Ando and Yukio Sakabe

"Fabrication and Electrical Characterization of Epitaxially Grown (Ba,Sr)TiO_3 Thin Films Prepared by Sol-Gel Method"

Key Engineering Materials, **320** (2006) pp.81-84.

Keisuke Kageyama, Tadasu Hosokura. Toshiyuki Nakaiso and Hiroshi Takagi

"Dielectric properties of (Ba,Sr)TiO_3 thin films with varied microstructures prepared by the chemical solution deposition method for thin-film capacitors and ferroelectric varactors"

IEEE Transaction on Ultrasonic, Ferroelectric and Frequency Control, **57** (2010) pp. 2198-2204.

Chapter 4

Tadasu Hosokura, Keisuke Kageyama, Hiroshi Takagi and Yukio Sakabe

"Fabrication and Characterization of a (100) Three-Axis-Oriented Single-Crystal $(Ba_{0.7}Sr_{0.3})TiO_3$ Thin Film Prepared by the Chemical Solution Deposition Method"

Journal of the American Ceramic Society, **92** (2009) pp.253-255.

Tadasu Hosokura, Keisuke Kageyama, Hiroshi Takagi and Yukio Sakabe

"(100) Three-Axis-Oriented $BaTiO_3$ Thin Film with $BaZrO_3$ Buffer Layer on MgO(100) Prepared by Chemical Solution Deposition Method"

Journal of the American Ceramic Society, **93** (2010) pp. 630-633.

Tadasu Hosokura, Keisuke Kageyama, Hiroshi Takagi and Yukio Sakabe

"Development of (100) Three-Axis-Oriented Single Crystal $(Ba_{0.7}Sr_{0.3})TiO_3$ Thin Film Fabrication on Pt/MgO(100) Substrate by Chemical Solution Deposition Method"

Ceramic Transactions, **216** (2010) pp.73-82.

Tadasu Hosokura, Keisuke Kageyama, Hiroshi Takagi and Yukio Sakabe

"(100) three-axis-oriented $BaTiO_3$, $(Ba_{0.7}Sr_{0.3})TiO_3$ Thin Film Prepared by Chemical Solution Deposition Method"

International Journal of Ceramic Technology, **9** (2012) pp.74-82.

Naoki Matsumoto, Tadasu Hosokura, Keisuke Kageyama, Hiroshi Takagi, Yukio Sakabe and Masanori Hangyo

"Analysis of Dielectric Response of TiO_2 in Terahertz Frequency Region by General Harmonic Oscillator Model"

Japanese Journal of Applied Physics, **47** (2008) pp7725-7728.

Naoki Matsumoto, Tadasu Hosokura, Takeshi Nagashima and Masanori Hangyo

"Measurement of the dielectric constant of thin films by terahertz time-domain spectroscopic ellipsometry"

Optics Letters, **36** (2011) pp265-267.

Chapter 5

Tadasu Hosokura, Naoki Iwaji,Takuji Nakagawa, Akira Ando, Hiroshi Takagi, Yukio Sakabe and Kazuyuki Hirao

“(100)-Oriented $SrTiO_3$/$BaTiO_3$ Artificial Superlattices Fabricated by Chemical Solution Deposition”

Crystal Growth & Design, **11** (2011) pp.4253-4256.

Proceedings

Chapter 1

Tadasu Hosokura, Satoshi Shindo, Syuichi Shimada and Makoto Kuwabara

Proceedings of the 19th International Korea-Japan Seminar on Ceramics, November 2002

"Preparation and Characterization of Barium Titanate Thin Films by Electrophoretic Sol-Gel Deposition Using a High Concentration Alkoxide Solution "

Makoto Kuwabara and Tadasu Hosokura

Proceedings of the American Ceramics Society 17th cocoa beach annual

"Synthesis and Dielectric Properties of Dense Nanocrystalline Barium Titanate Thin Films by a Novel Electrodeposition Method Using a Highly-Concentrated Alkoxide Solution"

Chapter 3

Keisuke Kageyama, Tadasu Hosokura. Toshiyuki Nakaiso and Hiroshi Takagi

Proceedings of the 17th IEEE International Symposium on the Applications of Ferroelectrics 2008

"Dielectric properties of (Ba,Sr)TiO_3 thin films with varied microstructures prepared by the chemical solution deposition method for thin-film capacitors and ferroelectric varactors"

Chapter 4

Tadasu Hosokura, Keisuke Kageyama, Hiroshi Takagi and Yukio Sakabe

Proceedings of the 8th Pacific Rim Conference on Ceramic and Glass Technology 2009

"Development of (100) Three-axis-oriented ($Ba_{0.7}Sr_{0.3}$)TiO_3 Thin Film fabricated on Pt/MgO(100) Substrate by Chemical Solution Deposition Method"

Tadasu Hosokura, Keisuke Kageyama, Hiroshi Takagi and Yukio Sakabe

Proceedings of the Ceramic Interconnect and Ceramic Microsystems Technologies 2010

"(100) three-axis-oriented BT, BST Thin Film Prepared by Chemical Solution Deposition Method"

Acknowledgment

I would like to acknowledge my deep sense of gratitude to Professor Kazuyuki Hirao, Department of Material Chemistry, Graduate School of Engineering in Kyoto University, for his guidance and supervision throughout this study.

I would like to express my gratitude to Dr. Yukio Sakabe, Corporate Adviser of Murata Manufacturing Co., Ltd., I thank him for guiding me all the way in pursuit of this work. I deeply appreciate to Dr. Hiroshi Takagi, Vice President, Director Yasu Plant, Materials Development Group, Technology & Business Development Unit of Murata Manufacturing Co., Ltd., for encouragement and full understanding of my work.

I am deeply grateful to Dr. Akira Ando, General Manager of Materials Development Dept.2, Materials Development Group, Murata Manufacturing Co., Ltd. I acknowledge him for devoting time to participate in many fruitful discussions and guidance. Grateful acknowledgements are made to Dr. Keisuke Kageyama, General Manager of Research Dept. Research Center for Next Generation Technology of Murata Manufacturing Co., Ltd., for his guidance and kind discussions.

I am thankful to Dr. Takuji Nakagawa Research Dept. Research Center for Next Generation Technology of Murata manufacturing Co., Ltd., for general advice and technological help. I would like to extend my thanks to Ivoyl P. Koutsaroff, Associate Chief Researcher of Materials Development Dept.2, Materials Development Group, Murata Manufacturing Co., Ltd., for his fruitful advices. I thank to Dr. Keigo Suzuki, Associate Chief Researcher of Materials Development Dept.2, Materials Development Group, Murata Manufacturing Co., Ltd., for his help and encouragement.

Special thanks to Naoki Iwaji, Analysis Dept. Technology & Business Development Unit of Murata Manufacturing Co., Ltd., for Cs-STEM analysis and discussions. I am so appreciated to Nobuhiro Tanaka, Koichi Banno, Shoichiro Suzuki, Masashi Inoguchi, Takafumi Okamoto, Hiroyuki Kondo, Huabing Zhou, Ayumi Shinagawa

and Sena Isoda the members of Materials Development Dept.2 of Murata Manufacturing Co., Ltd., for their words of encouragement and support.

Finally, I express my appreciation to my wife, Astuko Hosokura, for hearty encouragement and unconditional support.